Supplementary Information

Strain–Induced Spin Regulation of Stepped Co(111) for Boosting Peracetic Acid Magnetocatalysis

Yinqiao Zhang [a #], Xiaona Zhang [a #], Shuhan Qin [a], Hao Liang [a], Yiming Ma [a], Yan Di [a], Wei Meng [a], Sijin Zuo [a *] and Minghua Zhou [b]

[a] State Key Laboratory of Natural Medicines, School of Engineering, China Pharmaceutical University, Nanjing 210009, PR China

[b] College of Environmental Science and Engineering, Nankai University, Tianjin 300350, PR China

[#] These authors contributed equally: Yinqiao Zhang and Xiaona Zhang

[*]Corresponding author. E–mail: sjzuo@cpu.edu.cn

Text S1. Chemicals and Reagents

All reagents were at least analytical grade and used as received without further purification. Sulfamethoxazole (SMX), naproxen, and 2,2,6,6–tetramethylpiperidin–1–oxy radical (TEMPO) were purchased from Sigma–Aldrich Co., Ltd. (St. Louis, MO, USA). Cobalt nitrate hexahydrate ($Co(NO_3)_2$•$6H_2O$), dicyandiamide ($C_2H_4N_4$), methyl alcohol (MeOH), furfuryl alcohol (FFA), L–histidine, β–carotene, 2,4–hexadiene (2,4–HD), sodium thiosulfate ($Na_2S_2O_3$), terephthalic acid, 9,10–diphenylanthracene (DPA), methyl phenyl sulfoxide (PMSO), methyl phenyl sulfone ($PMSO_2$), sodium bicarbonate ($NaHCO_3$), sodium chloride (NaCl), sodium sulphate (Na_2SO_4), sodium hydroxide (NaOH), sulfuric acid (H_2SO_4), potassium iodide (KI), humic acid (HA), methylene blue, ethylenediamine tetraacetic acid disodium salt (EDTA–2Na), sodium hypochlorite, sodium perborate ($NaBO_3$), potassium peroxodisulfate, potassium peroxymonosulfonic acid ($H_3K_5O_{18}S_4$), hydrogen peroxide (H_2O_2), N,N–dimethylformamide were obtained from Aladdin Biological Technology Co., Ltd. (Shanghai, China). Acetonitrile (ACN) of high–performance liquid chromatography (HPLC) grade was purchased from Anhui Tiandi Life Science and Technology Co., Ltd. Except for DPA stock solution, which was prepared using ACN as the solvent, all the stock solutions were prepared in Milli–Q water (>18.2 MΩ·cm).

Text S2. Characterizations

The physical morphologies of catalysts were characterized by Transmission Electron Microscopy (TEM), high–resolution TEM (HRTEM, JEM–2100 HR, JEOL) and aberration–corrected high–angle annular dark–field scanning transmission electron microscopy (AC–HAADF–STEM, JEM–ARM300F2, JEOL) quipped with a Gatan image filter spectrometer. Geometric phase analysis (GPA) to characterize the strain distribution of catalysts was obtained by an open–source program $Strain^{++}$ plug in the software of Digital Micrography. Raman spectra were recorded on the Raman spectrometer (LABRAM HR800) under the excitation of a 532 nm laser. The surface element valence states of catalysts were examined with K–Alpha X–ray Photoelectron Spectrometer (XPS). X–ray diffraction (XRD, Bruker–D8 Instrument) using Cu Kα radiation (λ 0.15418 nm) was used to analyze the crystalline structure of catalysts. Concentrations of organics were determined by the high–performance liquid chromatography (HPLC, LC–20AT, Shimadzu, Japan) equipped with a Waters C18 analytical column (4.6 mm×150 mm, particle size 5 μm) and a diode array detector (DAD). Intermediates of SMX degradation were detected by liquid chromatography–mass spectrometry (LC/MS, Agilent 1260/6420). Electron paramagnetic resonance

spectroscopy (EPR, EMX–10/12, Bruker) was adopted to analyze the physicochemical structure of catalysts and the reactive species generated in reaction systems. Zero field cooled measurements were executed by magnetic property measurement system (SQUID–VSM, Quantum Design) under 1 kOe. The X–ray absorption experiments were carried out at the XAS station (BL14W1) at the Shanghai Synchrotron Radiation Facility (SSRF), China. Co foil, CoO, Co_2O_3 and cobalt phthalocyanine (CoPc) were used as reference samples. The magnetism measurements were conducted in a commercial magnetic property measurement system (MPMS–squid VSM–094).

Text S3. Catalysts' synthesis

2.9 g DCD and 1.0 g $Co(NO_3)_2$•$6H_2O$ were put into a 2 mL ethanol solution. The foregoing mixtures were placed in an agate mortar and continuously grinded until forming uniform pink pastes. Then, the pastes were annealed at 700 °C for 3.5 hours with a ramping rate of 5 °C min^{-1} under a nitrogen atmosphere to obtain the powder catalyst termed as CNT/Co_n. Acid wash of the obtained catalysts to remove some impurities such as weakly–bonded cobalt debris was conducted in 0.5 M H_2SO_4 for 4 hours. The catalysts of N/C, N/C–Co_{n-2}, CNT/Co_{n-1} and CNT/Co_{n+1} were respectively prepared by adjusting the dosage of $Co(NO_3)_2$•$6H_2O$ to 0, 0.1, 0.5, and 2.0 g. XPS survey spectrum of catalysts indicated that these catalysts only contain cobalt, carbon, oxygen and nitrogen elements (Fig. S17 below). Cobalt concentrations doped in CNT/Co_{n-1}, CNT/Co_n and CNT/Co_{n+1} catalysts were measured to be 12.6 wt.%, 14.3 wt.% and 17.8 wt.% respectively, via thermogravimetric analysis technology, shown in Fig. S6 below.

Text S4. PAA measurement

The stock solution of PAA was prepared by the reaction of H_2O_2 and CH_3COOH under the catalysis of sulfuric acid [1], where the PAA/H_2O_2 molar ratio in the stock solution was 0.83. As the PAA stock solution contains high concentrations of PAA and H_2O_2, the total concentration of PAA and H_2O_2 was tested by iodimetry titration method [2]. Briefly, potassium iodide was added as an iodine source, and ammonium molybdate as a catalyst for free iodine production (equations (1–2)). The concentration of total oxidant in the system was determined by titration of free iodine with sodium thiosulfate (equation (3)). The concentration of H_2O_2 in the system was then tested by titration with potassium permanganate (equation (4)). Hence, the concentration of PAA in the stock solution can be obtained by the concentration of total oxidant minus the concentration of H_2O_2.

$$2KI+2H_2SO_4+CH_3COOOH = 2KHSO_4+CH_3COOH+H_2O+I_2 \quad (1)$$

$$2KI+2H_2SO_4+H_2O_2 = 2KHSO_4+2H_2O+I_2 \quad (2)$$

$$I_2+2Na_2S_2O_3 = 2NaI+Na_2S_4O_6 \quad (3)$$

$$2KMnO_4+3H_2SO_4+5H_2O_2=2MnSO_4+K_2SO_4+8H_2O+5O_2 \quad (4)$$

The residual concentration of PAA was determined by the potassium iodide colorimetric method [3]. The sample was taken at a predetermined time and immediately reacted with potassium iodide, the resulting iodine monomer reacting with excess iodide ions to form I_3^- showing a yellow color (Fig. S21g). The sample was analyzed by the UV–vis spectrophotometer at 350 nm. The standard curve between PAA and the corresponding absorbance value at 350 nm is displayed in Fig. S1 below.

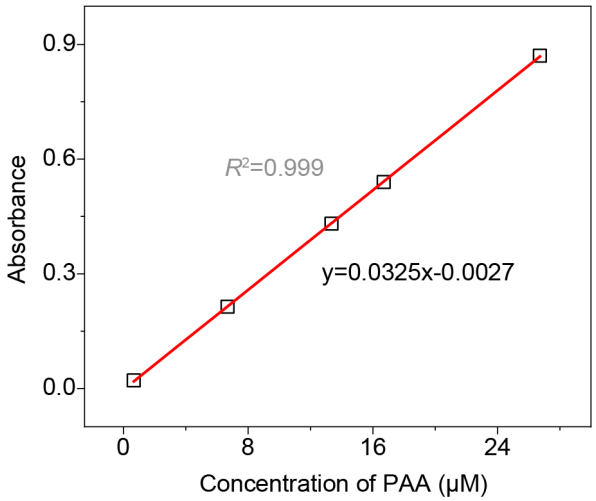

Figure S1. The standard curve between PAA concentration and its corresponding absorbance measured by the UV–vis spectroscopy.

Text S5. PAA utilization

During PAA activation process, 0.2 mM PAA was added into 200 mL reaction solution without target contaminant addition, and subsequently 10 mg L^{-1} catalyst was added for utilizing PAA to produce reactive species. To detect PAA activation under the magnetic field (MF), a magnet (60×40×10 mm) was introduced as an applied magnetic field and placed on the side wall of a beaker containing 200 mL of PAA solution. MF strength was adjusted by setting different numbers of magnets measured by Gaussmeter magnetic tester (TD8620, Changsha Tianheng Measurement and Control Technology Co., Ltd.). In PAA magnetocatalysis process, the dosage of catalysts were improved to 100 g L^{-1} to strengthen magnetism response of the reaction systems, and accordingly, the usage of PAA was decreased to 0.12 mM. The

utilization efficiency of PAA was quantified by the *k* value obtained from the pseudo–first–order kinetic model as equation (5) shown below.

$$-\ln\frac{C}{C_0}=kt \quad (5)$$

Text S6. Contaminant abatement

During contaminant degradation by PAA activation process, taken SMX as example, 2.5 mg L^{-1} SMX and PAA were simultaneously added into 200 mL reaction solution containing pre−dosed catalyst. At predetermined intervals, 1.0 mL reaction solution and 1.0 mL $Na_2S_2O_3$ solution (1.6 g L^{-1}) were mixed immediately to stop catalytic reaction. The above filtered solution was used to analyze the concentration of SMX by an HPLC system. The mobile phase was acetonitrile versus water (55:45, v/v%) with a flow rate of 1.0 mL min^{-1}, and the detection wavelength was selected at 265 nm.

Text S7. Kinetic model

According to the reaction kinetics of probe molecule removal in this work, its abatement can be expressed as equation (6).

$$-\ln\frac{[P]}{[P]_0}=k_{P,\cdot OH}\times\int[\cdot OH]dt+k_{P,R\text{-}O\cdot}\times\int[R\text{-}O\cdot]dt \quad (6)$$

where, [P] and $[P]_0$ represent the concentrations of a probe molecule at reaction and initial time, respectively; t represents the reaction time; $k_{P,\cdot OH}$ and $k_{P,R\text{-}O\cdot}$ represent the second–order rate constants for the reaction of target pollutants with •OH and R–O•, respectively; $\int[\cdot OH]dt$ and $\int[R\text{-}O\cdot]dt$ represent the exposures of •OH and R–O•, respectively.

To obtain the exposures of •OH and R–O•, SMX and naproxen (NAP) were selected as target pollutants. NAP has a naphthyl constructure and is easier attacked by R–O• [4]. Hereby, based on the reaction kinetics of SMX and NAP as shown in equations (7) and (8), $\int[\cdot OH]dt$ and $\int[R\text{-}O\cdot]dt$ can be obtained.

$$-\ln\frac{[SMX]}{[SMX]_0}=k_{SMX,\cdot OH}\times\int[\cdot OH]dt+k_{SMX,R\text{-}O\cdot}\times\int[R\text{-}O\cdot]dt \quad (7)$$

$$-\ln\frac{[NAP]}{[NAP]_0}=k_{NAP,\cdot OH}\times\int[\cdot OH]dt+k_{NAP,R\text{-}O\cdot}\times\int[R\text{-}O^{\cdot}]dt \quad (8)$$

$k_{SMX,\cdot OH}$, $k_{SMX,R\text{-}O\cdot}$, $k_{NAP,\cdot OH}$, and $k_{NAP,R\text{-}O\cdot}$ are 7.9×10^9 M^{-1} s^{-1}, 3.78×10^9 M^{-1} s^{-1}, 8.99×10^9 M^{-1} s^{-1} and 9×10^9 M^{-1} s^{-1}, respectively. $\int[\cdot OH]dt$ and $\int[R\text{-}O^{\cdot}]dt$ at 20 min reaction are 5.31×10^{-10} M s (87.5%) and 7.63×10^{-11} M s (12.5%), respectively. The $\int[R\text{-}O^{\cdot}]dt$ can be calculated according to equation (9).

$$-\ln\frac{[SMX]}{[SMX]_0}=k_{SMX,R\text{-}O\cdot}\times\int[R\text{-}O^{\cdot}]dt \quad (9)$$

Text S8. Electrochemical experiments

Electrochemical experiments were performed using a CHI 760E electrochemical workstation equipped with standard three–electrode electrochemical cells in 50 mM Na_2SO_4 solution, where counter electrode of platinum wire, reference electrode of saturated calomel electrode (SCE) and work electrode of carbon paper (1×2 cm) covered with the testing catalysts were applied. The catalyst ink was prepared by mixing 1 mg catalyst, 950 μL ethanol solution and 50 μL Nafion by sonication for 1 hour. The prepared catalyst ink was uniformly sprayed onto the carbon paper as a working electrode.

Text S9. DFT calculation

The density of states (DOS), work function, Fermi level, and adsorption energy etc., were calculated by the density functional theory (DFT) calculations using the Vienna Ab initio Simulation Package (VASP) within the generalized gradient approximation (GGA) using the Perdew–Burke–Ernzerhof (PBE) functional. The projected augmented wave (PAW) potentials were chosen to describe the ionic cores. The cutoff energy for the planewave basis set was set to 450 eV. A 20 Å vacuum space was applied along the Z–direction to reduce the mirror image interaction. The Brillouin zone was sampled with 3×3×1 Monkhorst–Pack k–mesh. Geometry optimizations were performed with the force convergency smaller than 0.02 eV/Å. Grimme's DFT–D3 method was applied to the dispersion correction. The vacuum thickness was set 20 Å. The model of cobalt single atom (Co SA) contained 39 atoms. The model of Co (111) contained 3 layers of Co atoms (60 atoms).

To investigate the most likely to be exposed crystal plane for fcc–Co surfaces, we built a Wulff construction by calculating the surface energy of each crystal plane [5]. The slabs of each crystal plane

have 8 layers of cobalt atoms and a 20 Å vacuum space was applied along the z–direction. The Brillouin zone was sampled with 12×12×1 Monkhorst–Pack k–mesh. The surface energy ($E_{surface}$) can be calculated according to equation (10).

$$E_{surface} = (E_{total}–N×E_{bulk})/2A \quad (10)$$

where, N is the number of atoms in the slab; E_{total} is the calculated total energy of the slab; E_{bulk} is the total energy per atom of fcc–Co, and A is the surface area of the slab.

Text S10. Theoretical analysis of organics

The theoretical analysis of organics was performed using the Gaussian 16 program package. The geometry structures, vibrational frequencies and Gibbs free energy of all the molecules involved in this work were optimized and analyzed at the M06–2X/6–311G+(d,p)/SMD (water) level [6]. The transient states were searched by the same method. The DFT–D3 empirical correction method was employed to describe the van der Waals interactions. Multiwfn and VMD software were used for the analyzation and visualization of Fukui function, dual describer, HOMO and LUMO.

Text S11. Calculation for the effective magnetic moment of catalysts

The effective magnetic moment (μ_{eff}) can be calculated according to equations (11–12) [7].

$$\mu_{eff} = \sqrt{8C}\mu_B \quad (11)$$

$$\mu_{eff} = \sqrt{n(n+2)}\mu_B \quad (12)$$

where, μ_B is Bohr magneton, C is Curie constant, n is the number of single electrons.

C is derived from a linear fitting of χ^{-1}–T curve based on the Curie−Weiss law as shown in equation (13).

$$\chi = \frac{C}{T - \theta} + \chi_0 \quad (13)$$

where, χ is susceptibility, χ_0 is a constant susceptibility independent of temperature. θ and T are Curie−Weiss temperature and experimental temperature, respectively.

After the μ_{eff} is obtained, the fractions of low– and high–spin states (V_{LS} and V_{HS}) can be calculated according to equations (14–15) [8].

$$\mu_{eff} = g\mu_B\sqrt{S_{LS}(S_{LS}+1)V_{LS} + S_{HS}(S_{HS}+1)V_{HS}} \quad (14)$$

$$V_{LS} + V_{HS} = 1 \quad (15)$$

where, g is the Lande g−factor (g=2 for electron), S_{LS} and S_{HS} are total spin angular momentum of low and high spin states, respectively.

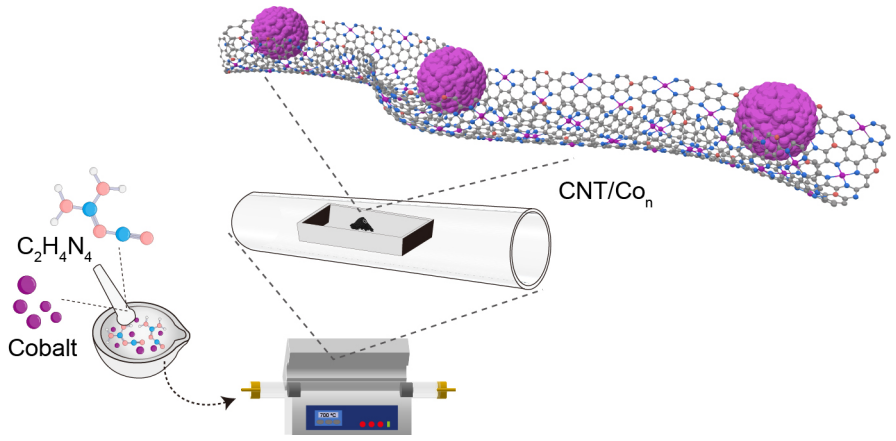

Figure S2. Schematical illustration for the catalyst preparation in one–pot pyrolysis strategy.

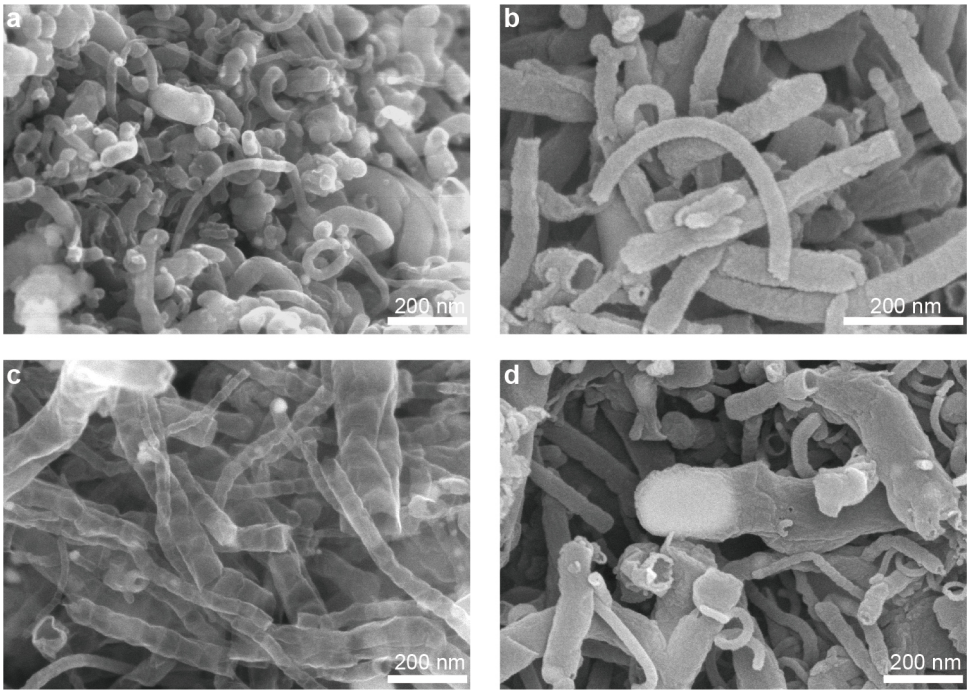

Figure S3. SEM images of a) N/C–Co_{n-2}, b) CNT/Co_{n-1}, c) CNT/Co_n and d) CNT/Co_{n+1} catalysts.

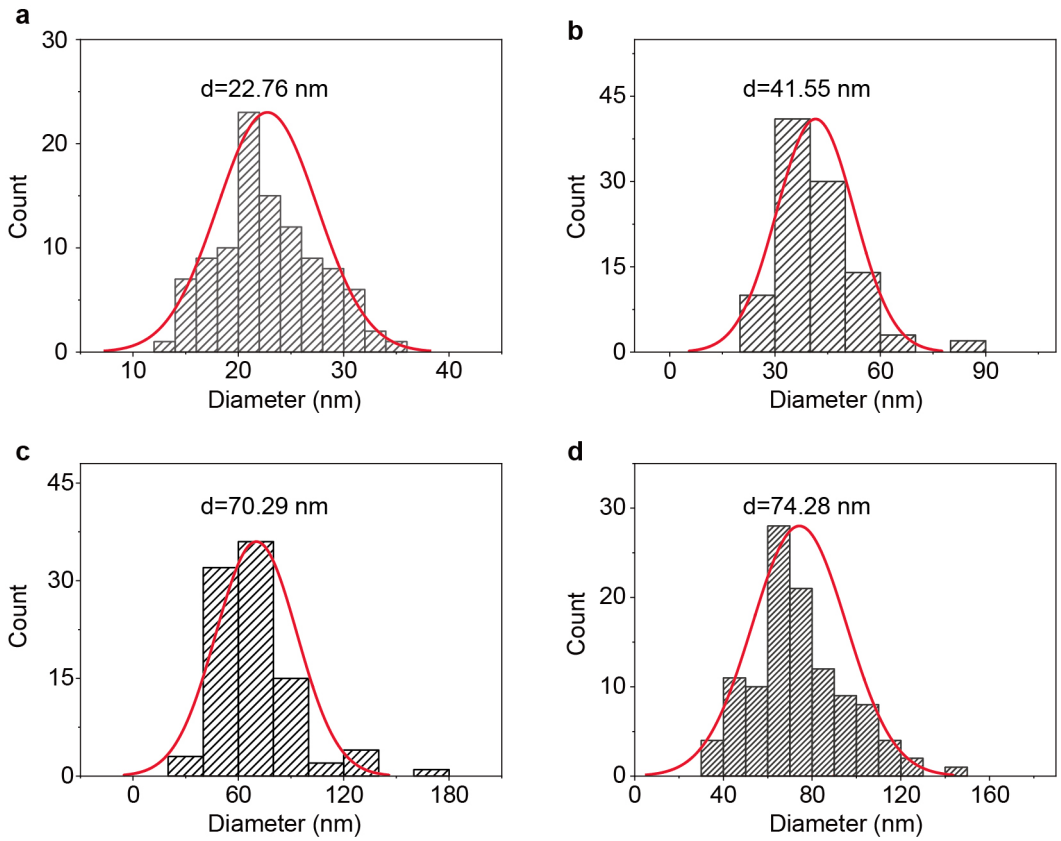

Figure S4. Histogram statistical diameter of a) N/C–Co_{n-2}, b) CNT/Co_{n-1}, c) CNT/Co_n and d) CNT/Co_{n+1} obtained from the results of SEM characterization above.

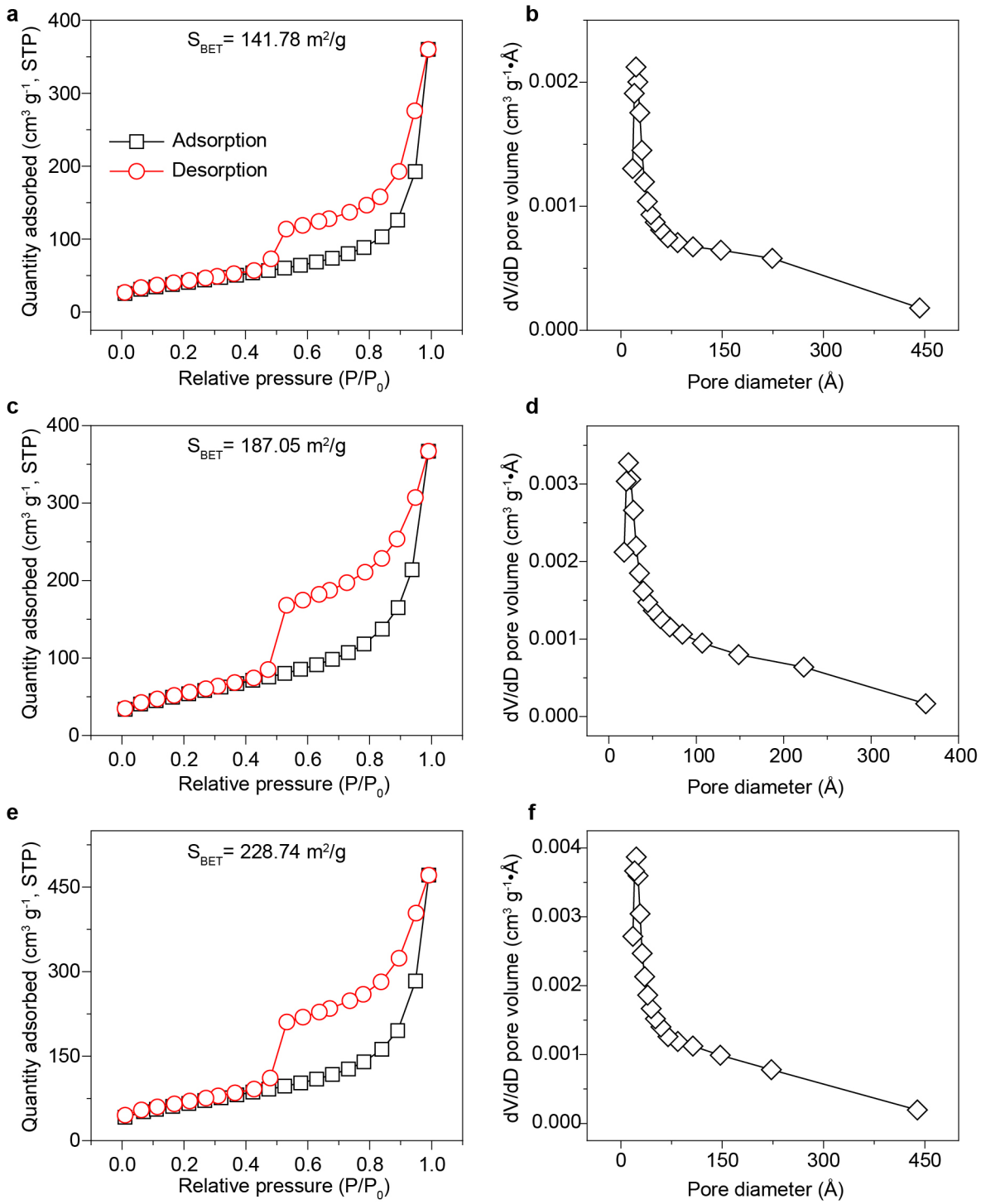

Figure S5. Nitrogen adsorption desorption isothermal curves of the a) CNT/Co_{n-1}, c) CNT/Co_n and e) CNT/Co_{n+1} catalysts. Their special surface area is displayed in the inset of each figure and was calculated based on the method of Brunauer–Emmett–Teller. Pore size distribution of the b) CNT/Co_{n-1}, d) CNT/Co_n and f) CNT/Co_{n+1} catalysts.

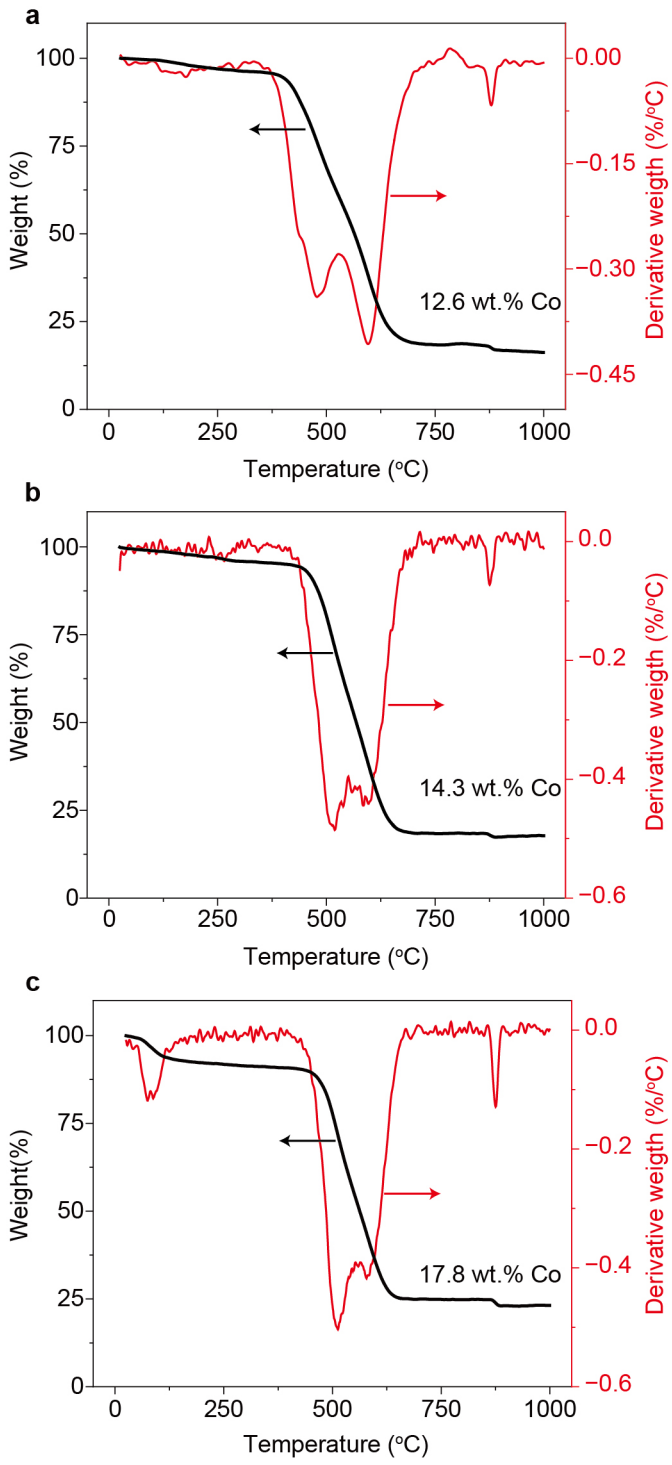

Figure S6. Thermogravimetric analysis (TGA) curves and corresponding differential scanning calorimetry (DSC) curve of the a) CNT/Co_{n-1}, b) CNT/Co_n and c) CNT/Co_{n+1} catalysts.

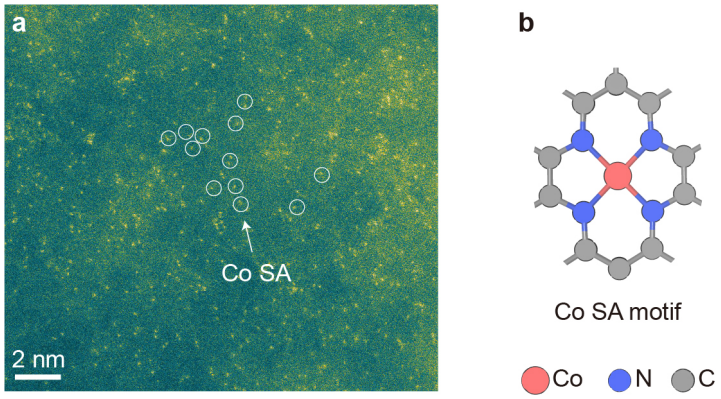

Figure S7. a) AC–HADDF–STEM image of atomically dispersed Co site in CNT/Co_n extracted from area I in Fig. 1b of the main text. b) Schematical illustration of Co–N_4 motif presented by atomically dispersed Co site in CNT/Co_n.

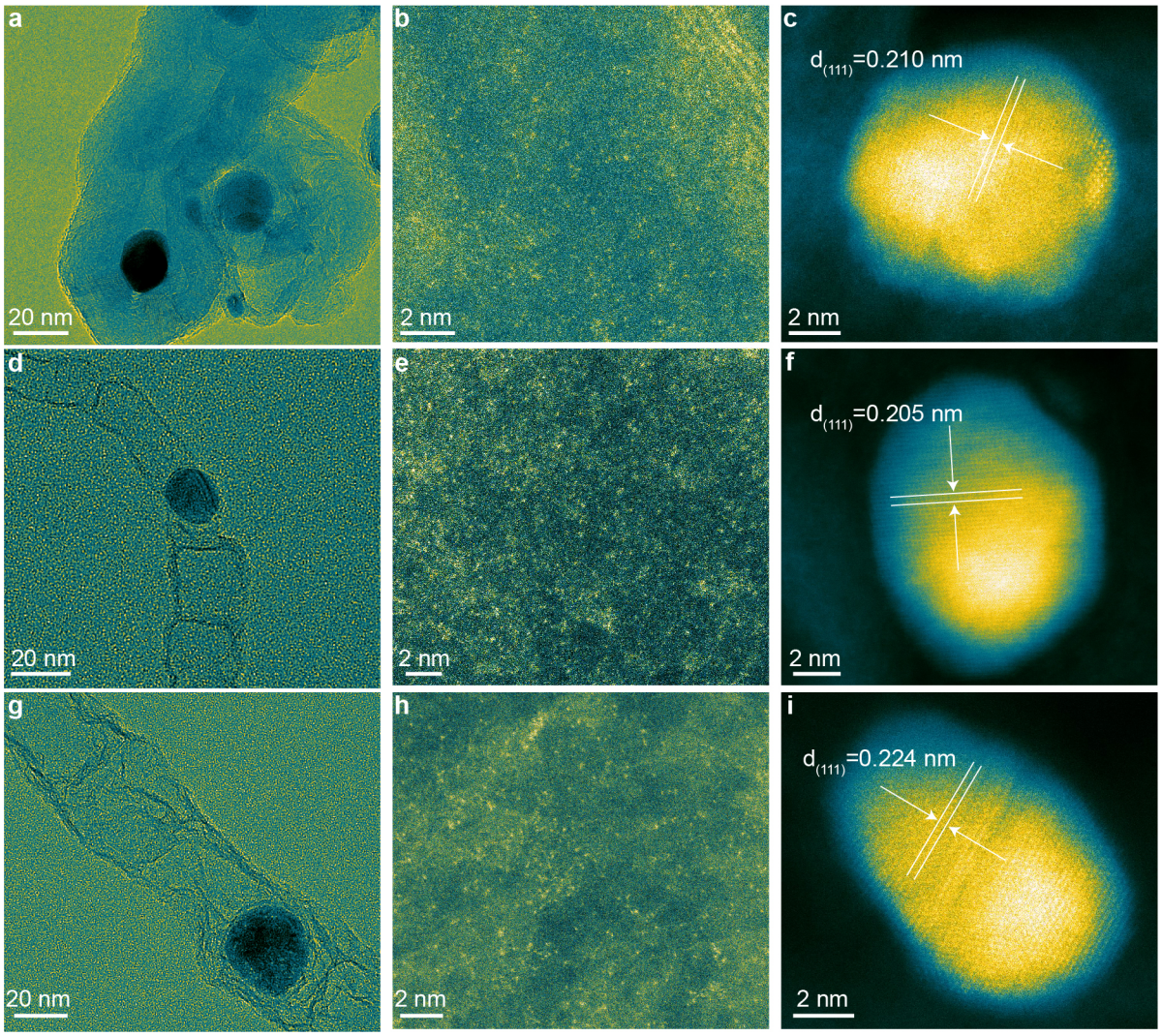

Figure S8. HR–TEM images of the a) N/C–Co_{n-2}, d) CNT/Co_{n-1} and g) CNT/Co_{n+1}. AC–HADDF–STEM images of atomically dispersed Co site in the b) N/C–Co_{n-2}, e) CNT/Co_{n-1} and h) CNT/Co_{n+1}. AC–HADDF–STEM image of nanoparticulate Co site in the c) N/C–Co_{n-2}, f) CNT/Co_{n-1} and i) CNT/Co_{n+1}.

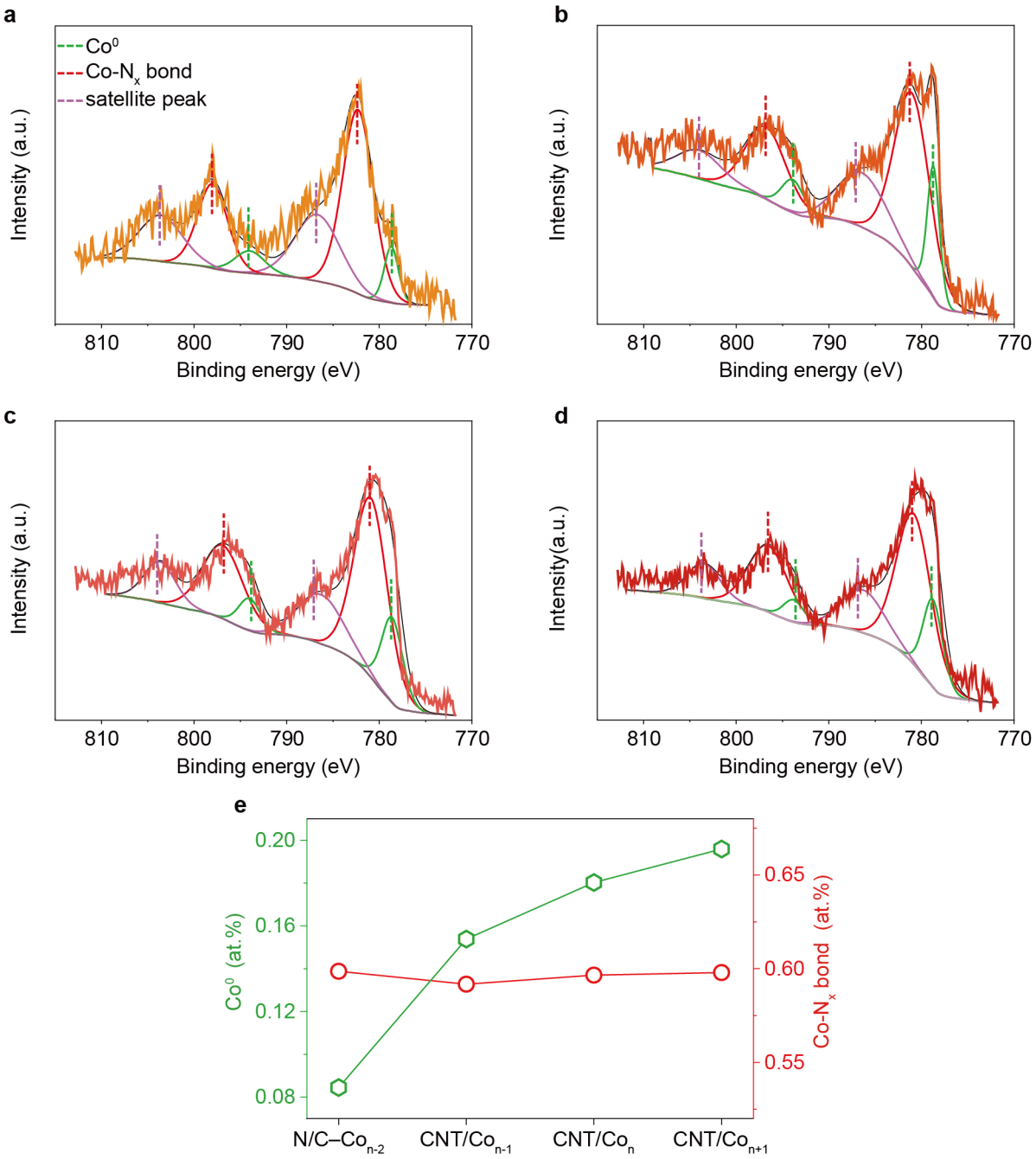

Figure S9. High–resolution Co 2p XPS survey spectrums of a) N/C–Co_{n-2}, b) CNT/Co_{n-1}, c) CNT/Co_n and d) CNT/Co_{n+1}. e) The atomic ratio of Co–N_x bond and Co^0 in the catalysts obtained from the deconvoluted peaks.

Interestingly, we found that increased feeding of cobalt source to brick carbon nanotube in–situ will obtain the catalysts with stable Co–N_x bonds content while increasing Co^0 amounts (Fig. S9e). It may hint the stable amount of atomically dispersed cobalt and reduced average valence state of cobalt for the catalysts with increasing cobalt resource feeding.

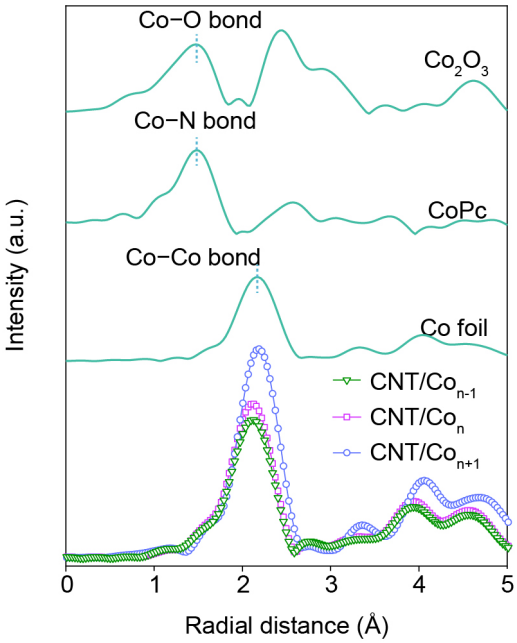

Figure S10. FT–EXAFS spectra of CNT/Co_n series and corresponding standard samples of Co foil, Co_2O_3 and CoPc to analyze the bonding environment of Co in our catalysts.

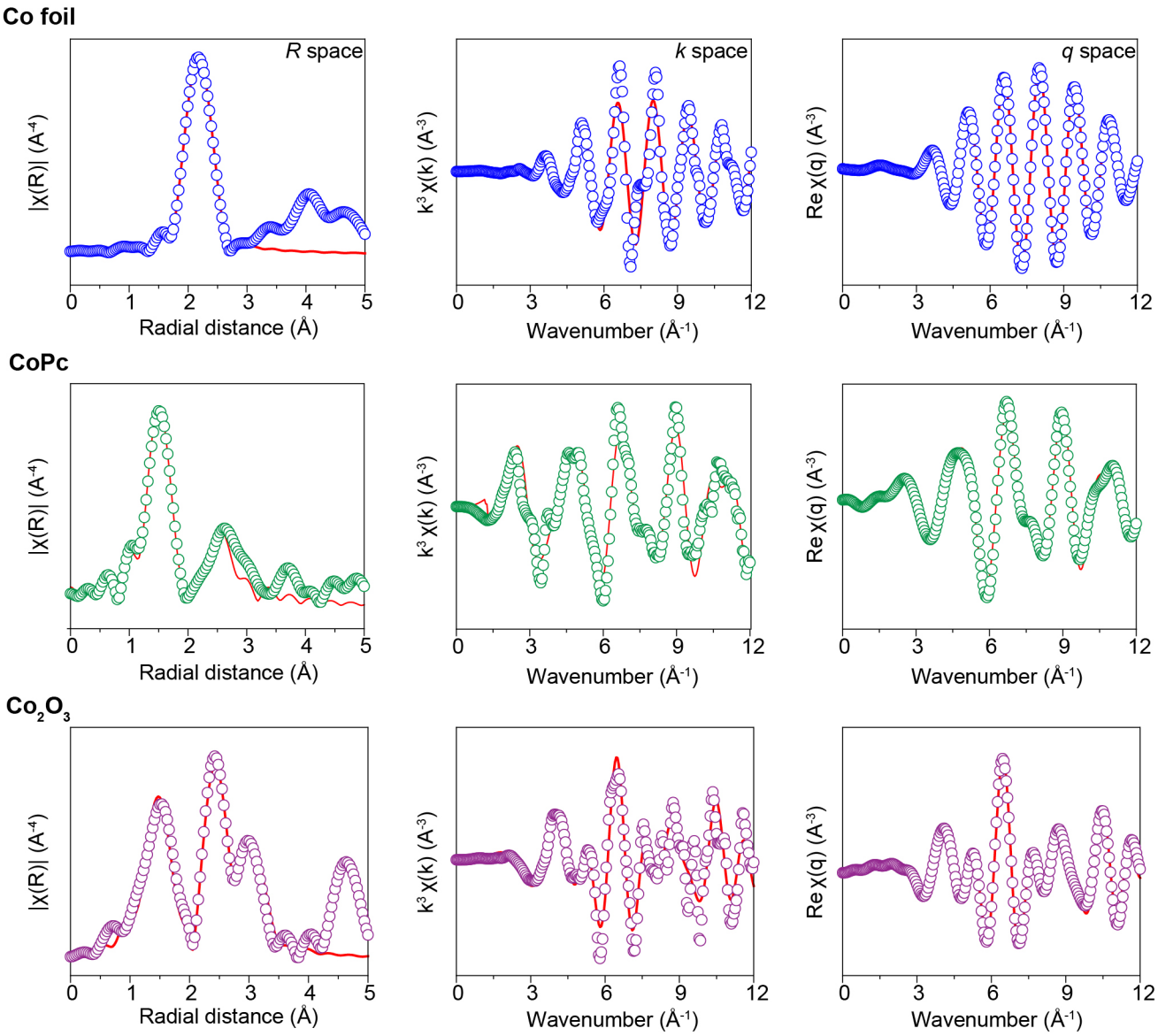

Figure S11. Experimental value and fitting value for FT–EXAFS spectra of the standard samples, Co foil, CoPc and Co_2O_3 at *R* space, *k* space and *q* space. The circle represents the experimental value, and the black line means the fitting value.

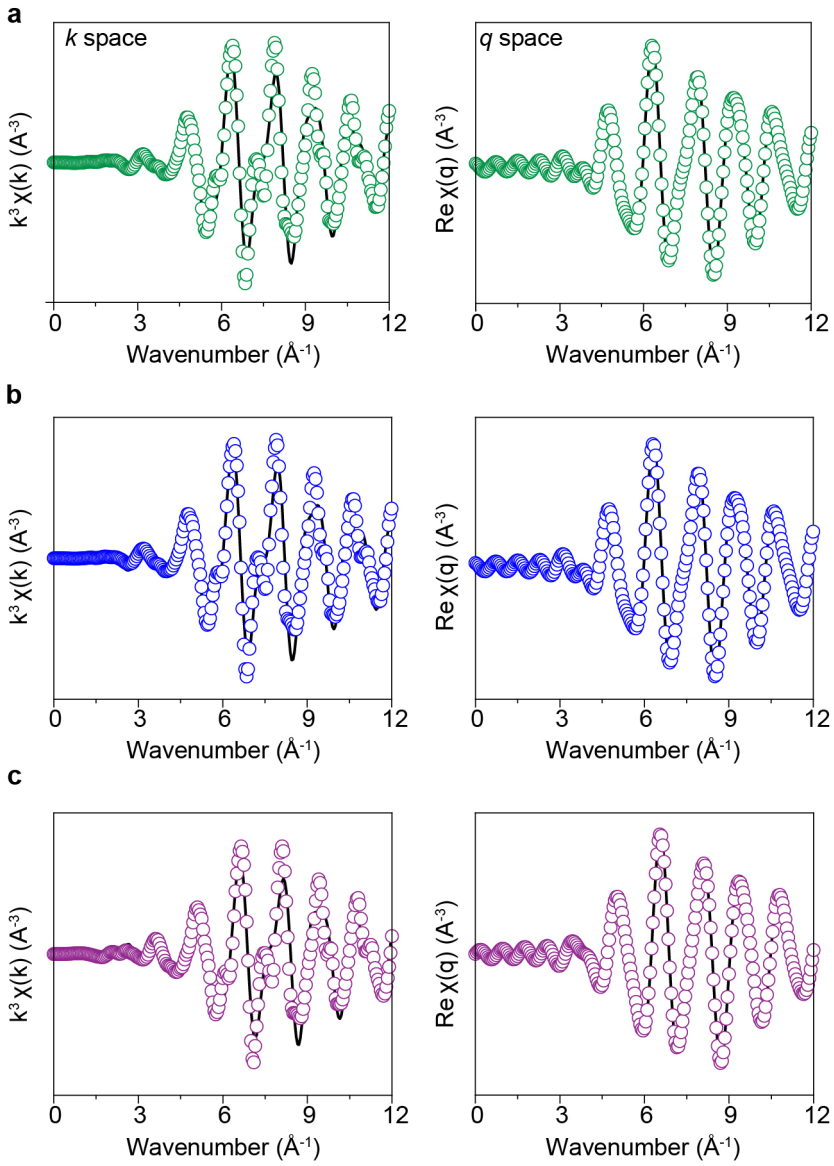

Figure S12. Experimental value and fitting value for FT–EXAFS spectra of a) CNT/Co_{n-1}, b) CNT/Co_n and c) CNT/Co_{n+1} catalysts at *R* space, *k* space and *q* space. The circle represents the experimental value, and the black line means the fitting value.

Table S1. Structural parameters of the catalysts obtained from their EXAFS fitting results

Catalysts	Path	CN	R (Å)	σ^2 ($\times10^{-3}$Å^2)	ΔE_0 (eV)	R–factor× 10^{-3}
Co foil	Co–Co	12	2.492±0.001	6.68±0.31	7.47±0.0001	0.299
Co_2O_3	Co–O	6.16±0.28	1.911±0.006	3.25±0.0029	-6.65±0.57	6.021
	Co–O–Co	5.25±0.44	2.857±0.005	4.68±0.619	-6.57±0.34	
	Co–O–Co	7.17±0.48	3.357±0.013	4.68±0.619	-6.57±0.34	
CoPc	Co–N	4.02±0.29	1.917±0.086	2.76±0.483	7.78±1.09	8.938
	Co–C	6.01±0.85	2.932±0.091	2.00±1.367	5.33±1.38	
CNT/Co_{n-1}	Co–Co	5.38±0.054	2.492±0.016	6.701±0.168	-5.49±0.13	0.623
	Co–N	3.61±0.54	2.063±0.061	27.264±6.078	-3.11±1.30	
CNT/Co_n	Co–Co	6.07±0.175	2.496±0.013	6.852±0.672	-4.73±0.32	5.576
	Co–N	3.99±0.853	2.044±0.041	24.201±11.104	-5.12±2.20	
CNT/Co_{n+1}	Co–Co	6.19±0.184	2.499±0.0096	6.677±0.255	8.25±0.13	0.801
	Co–N	3.79±0.491	2.027±0.024	54.602±7.204	6.51±1.411	
Co SA	Co–N	3.82±0.440	1.954±0.048	12.904±2.495	-3.82±0.401	9.381

Note: CN, coordination number. R, distance between adsorber and backscatter atoms. σ^2, Debye–Waller factor to account for both thermal and structural disorders. ΔE_0, inner potential correction. R factor indicates the goodness of fitting. S_0^2 was fixed to 0.89 as determined from Co foil fitting.

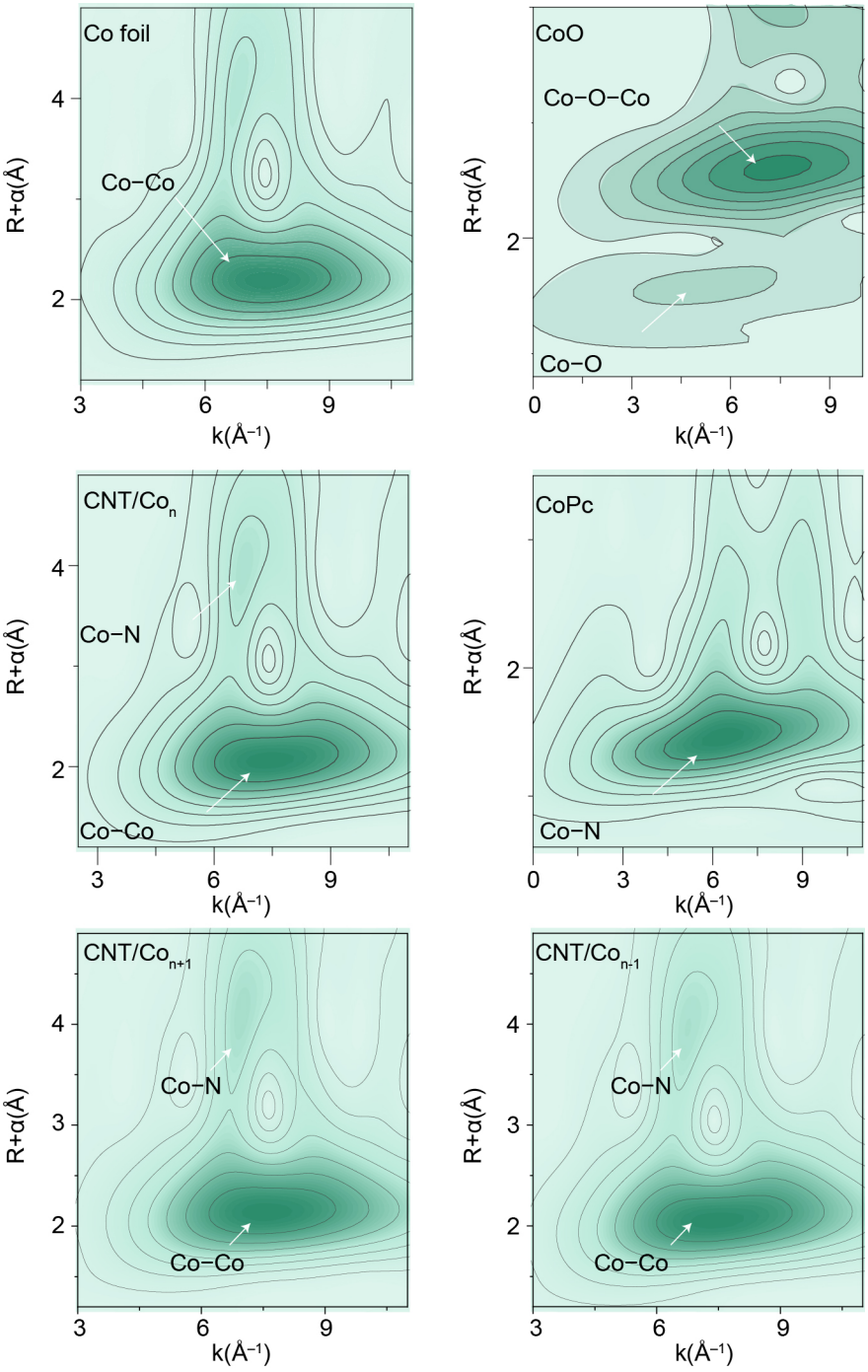

Figure S13. Wavelet transform plots of the k^3–weighted EXAFS of Co K–edge from our catalysts CNT/Co$_n$ series and the standard samples of Co foil, CoO and CoPc.

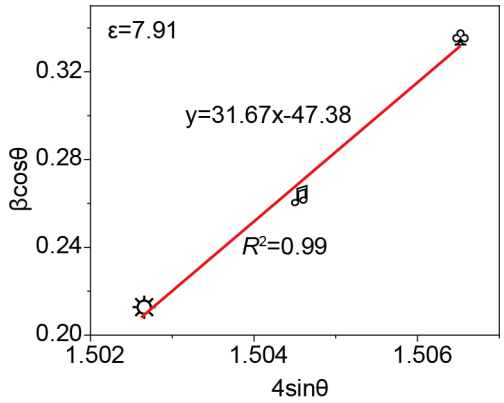

Figure S14. Analysis for XRD data of CNT/$Co_{n-1,}$ CNT/Co_n and CNT/Co_{n+1} in Williamson–Hall equation.

According to Williamson–Hall equation below [9], we can calculate the strain component ε to quantify the strain value. A positive value of ε indicate the tension strain.

$$\frac{\beta_{(111)}\cos\theta}{\lambda}=\frac{k\lambda}{D}+4\varepsilon\sin\theta \quad (15)$$

Where, $\beta_{(111)}$ is the measured full width at half maximum of (001) peak, λ is the wavelength of radiation (1.54056 Å for Cu Kα radiation). k is the Scherrer constant, 0.94. D represents the grain size in nanometer, θ is the diffraction angle. ε can be thus obtained from the slope by plotting $\beta_{(111)}\cos\theta$ versus 4sinθ.

Table S2. The parameters of Rietveld refinements from the catalysts' XRD data

Samples	Space group	Lattice parameters							R_p (%)	R_w (%)
		a (Å)	b (Å)	c (Å)	α (°)	β (°)	λ (°)	V (Å^3)		
CNT/Co_{n-1}	Fm–3m	3.54061	3.54061	3.54061	90.0	90.0	90.0	44.38	8.19%	7.72%
CNT/Co_n	Fm–3m	3.54839	3.54839	3.54839	90.0	90.0	90.0	44.68	9.22%	9.26%
CNT/Co_{n+1}	Fm–3m	3.55662	3.55662	3.55662	90.0	90.0	90.0	44.99	6.65%	7.57%

V means the unit cell volume.

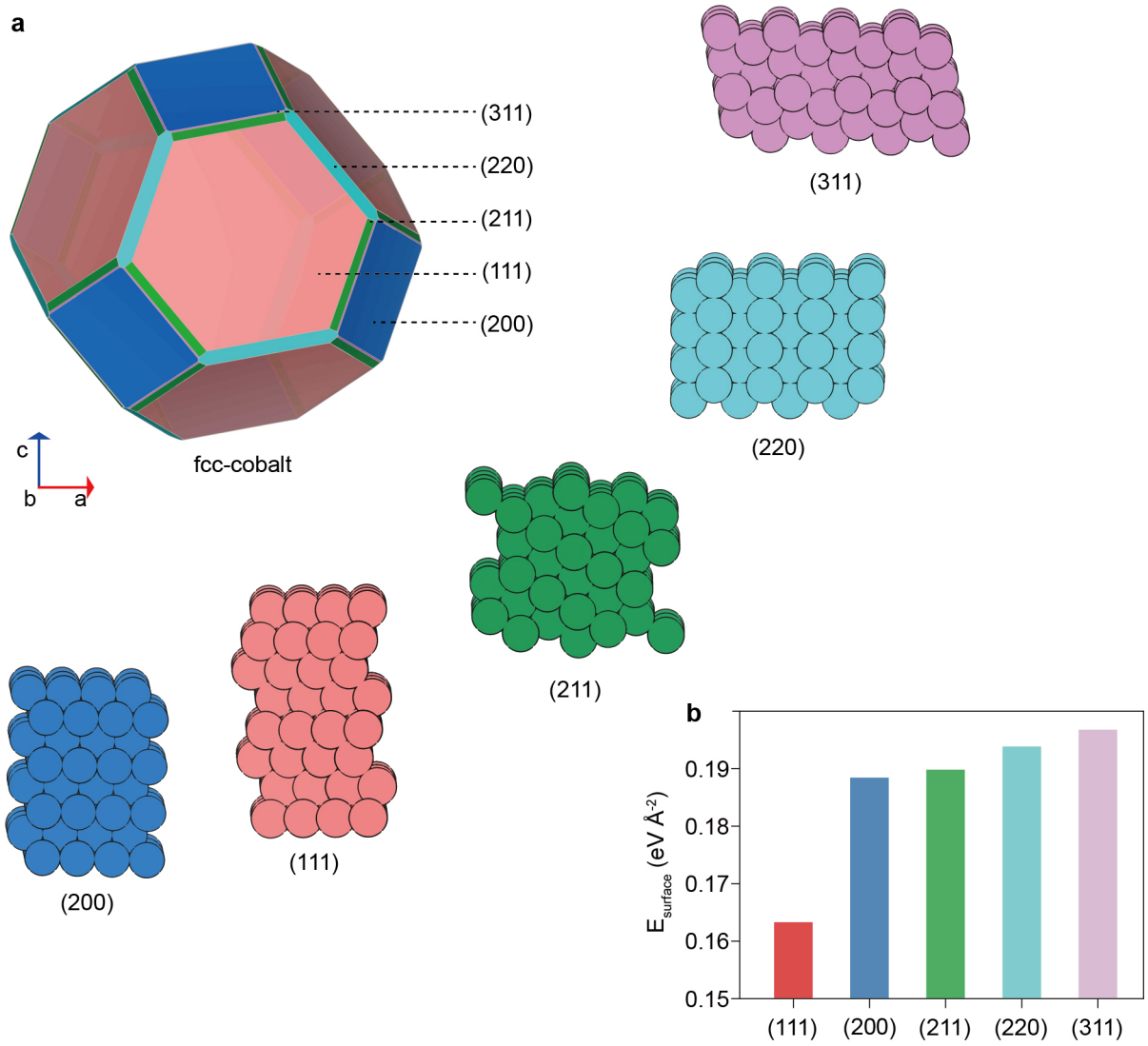

Figure S15. a) Built Wulff construction for fcc–cobalt based on the calculated surface energies. b) The corresponding surface energies of lattice planes.

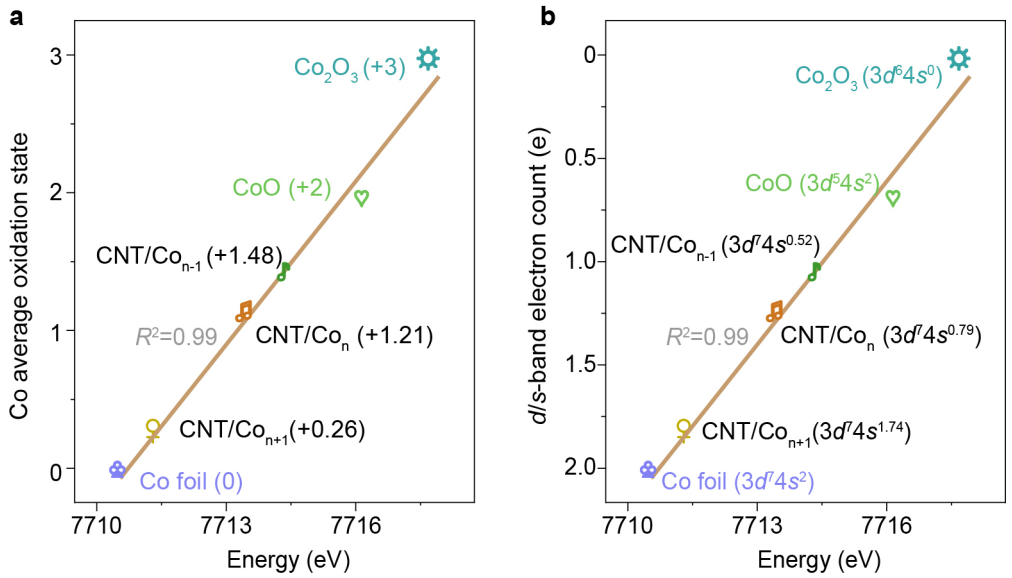

Figure S16. Linear fitting between a) cobalt average oxidation state and b) the outer electrons of cobalt sites and their corresponding positions at adsorption edges in Co *K*–edge XANES.

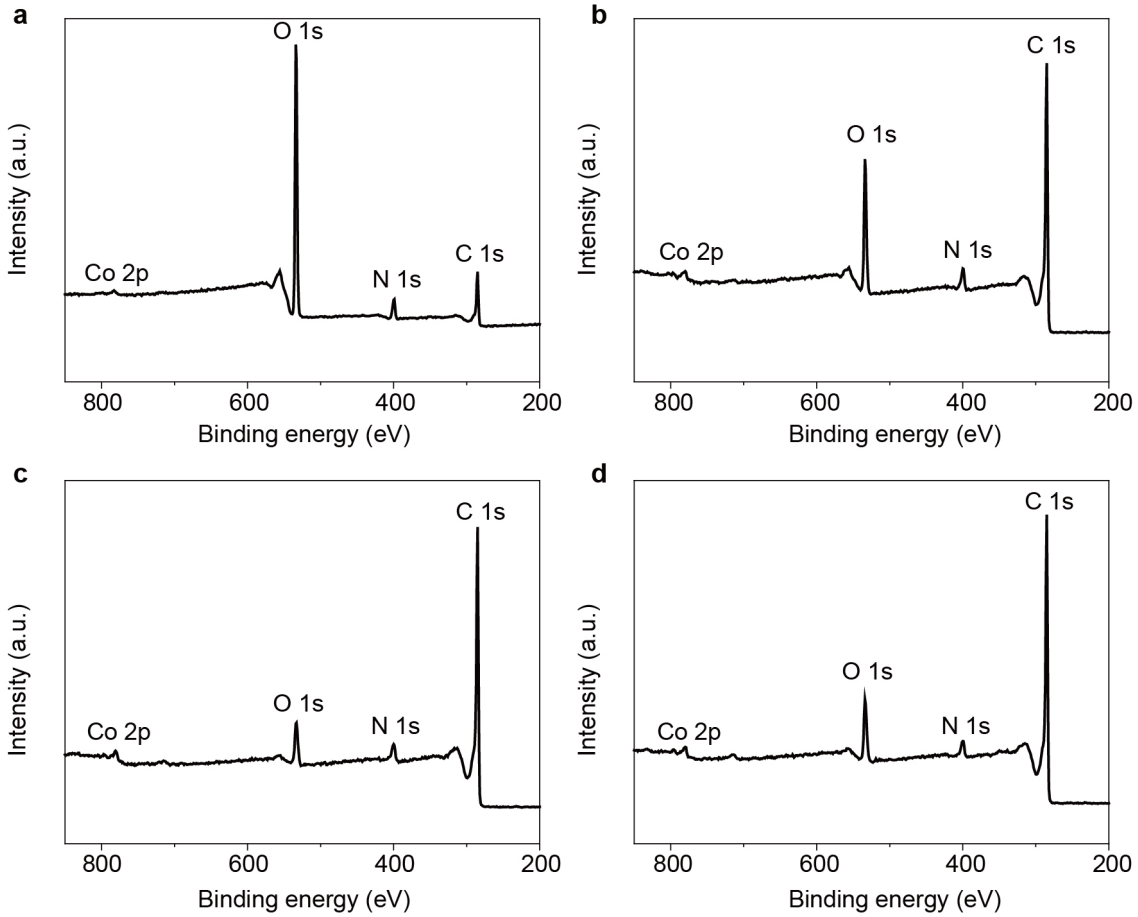

Figure S17. XPS survey spectrums of N/C–Co_{n-2}, CNT/Co_{n-1}, CNT/Co_n and CNT/Co_{n+1} catalysts. The spectrums indicated that these catalysts only contain cobalt, carbon, oxygen and nitrogen elements.

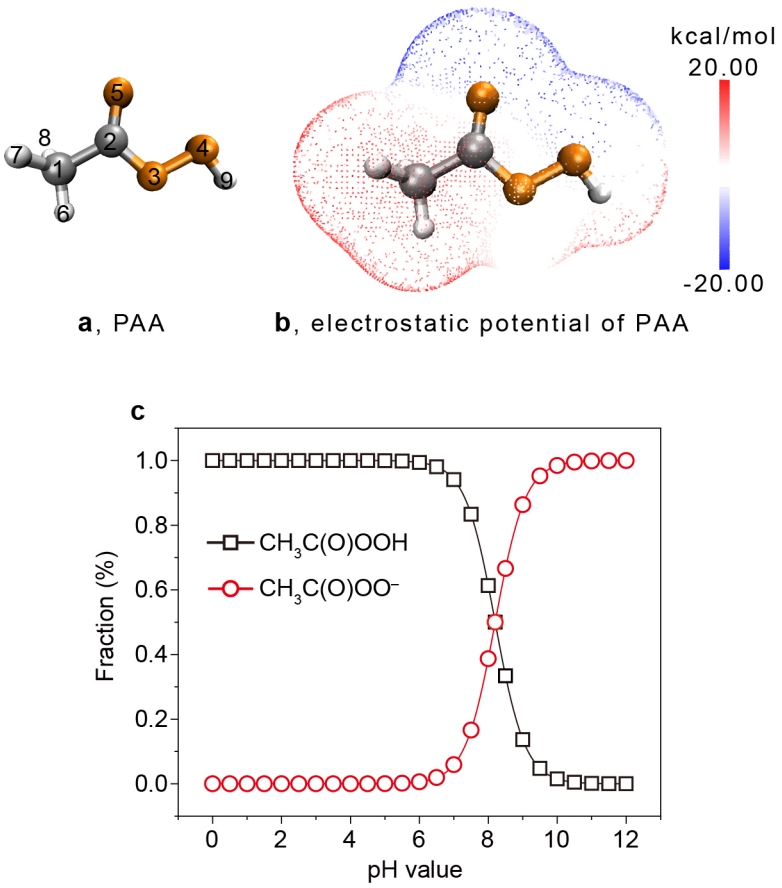

Figure S18. a) Optimized molecular structure of PAA. b) Electrostatic potential (ESP) of PAA. ESP of PAA displays O3 site have positive electrostatic potential differing with O1 and O2 sites of PAA. c) pH–dependent distribution of PAA species including $CH_3C(O)OOH$ and $CH_3C(O)OO^-$.

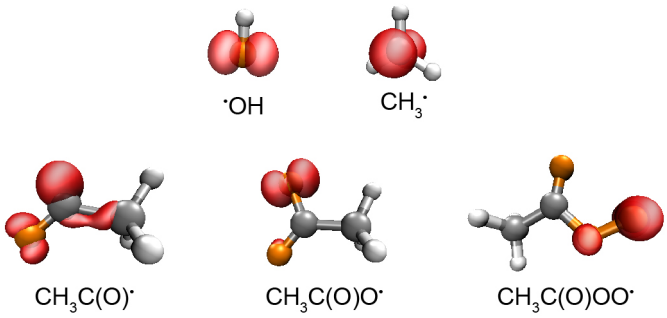

Figure S19. The spin–density distribution of free radicals including ·OH, CH_3·, $CH_3C(O)$·, $CH_3C(O)O$· and $CH_3C(O)OO$·.

Table S3. Chemical properties of free radicals involved in this work

Free radicals	Electronic affinity[a], eV	Van der waals radius[b], Å	Lifetime[c]	Oxidation potential[d], V vs NHE
·OH	5.54	2.00	<1 μs [10]	2.70 [11]
CH_3·	2.94	2.24	9~12 ns [10]	-0.98 [11]
$CH_3C(O)$·	2.60	3.49	8.7 μs[e] [12]	-1.10 [13]
$CH_3C(O)O$·	6.10	4.09	> 10 μs [10]	2.24 [11]
$CH_3C(O)OO$·	4.78	5.14	--	1.60 [11]

-- means not found in related literature. [a,b] These data are obtained from our DFT calculation, and [c,d] the data is collected from references. [e] The lifetime of $CH_3C(O)$· is measured in 2,3–butanedione.

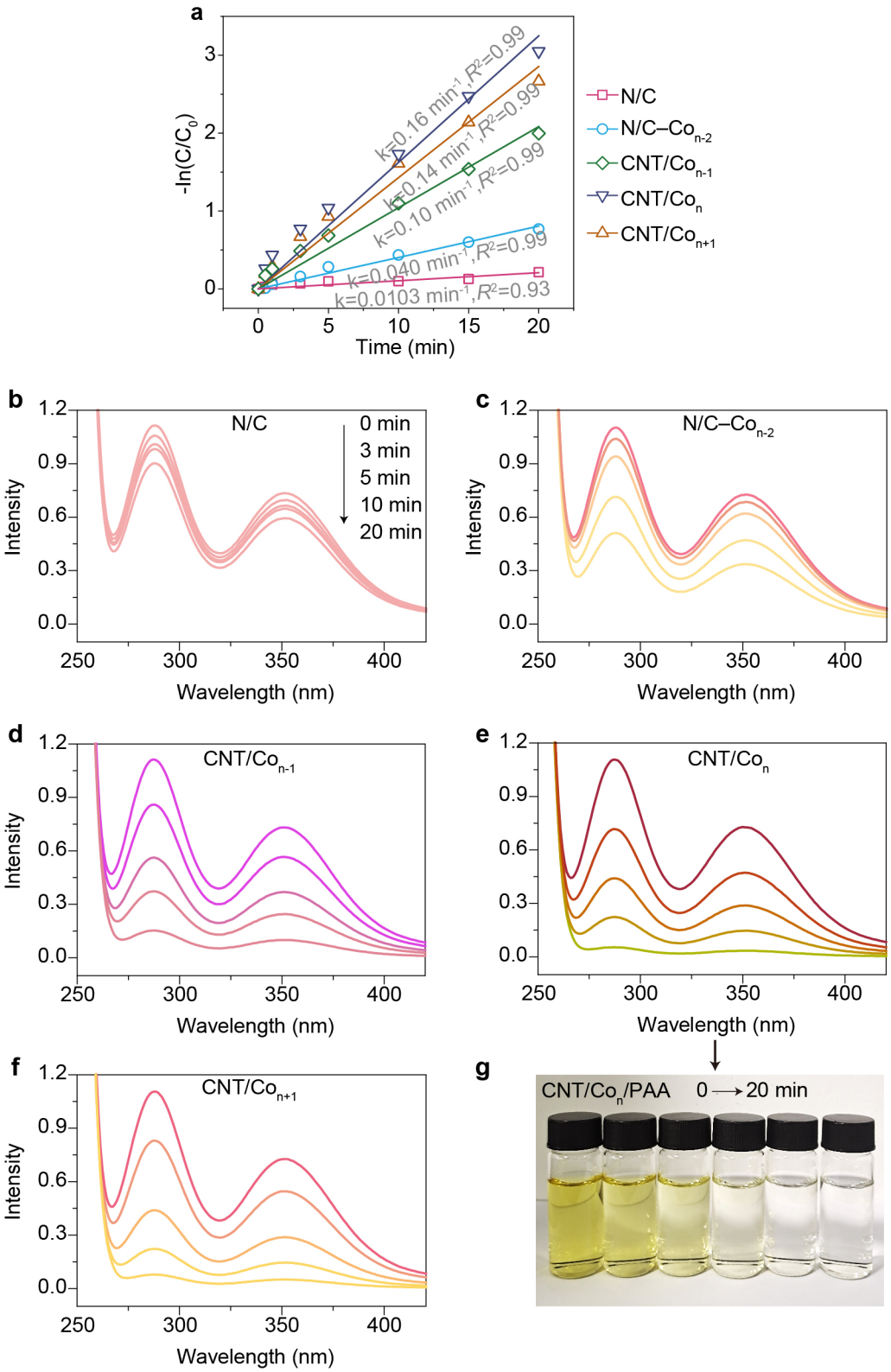

Figure S20. a) Linear fitting of -ln(C/C_0) against time course to calculate the *k* values for PAA utilization by different catalysts. b to f) UV–vis absorption spectra of I_3^- to quantify the concentration change of PAA in the systems of N/C, N/C–Co_{n-2}, CNT/Co_{n-1}, CNT/Co_n and CNT/Co_{n+1}, respectively. g) Digital photo of post–reaction solution from CNT–Co_n/PAA system. The yellow color of I_3^- can be used to quantify the concentration of PAA.

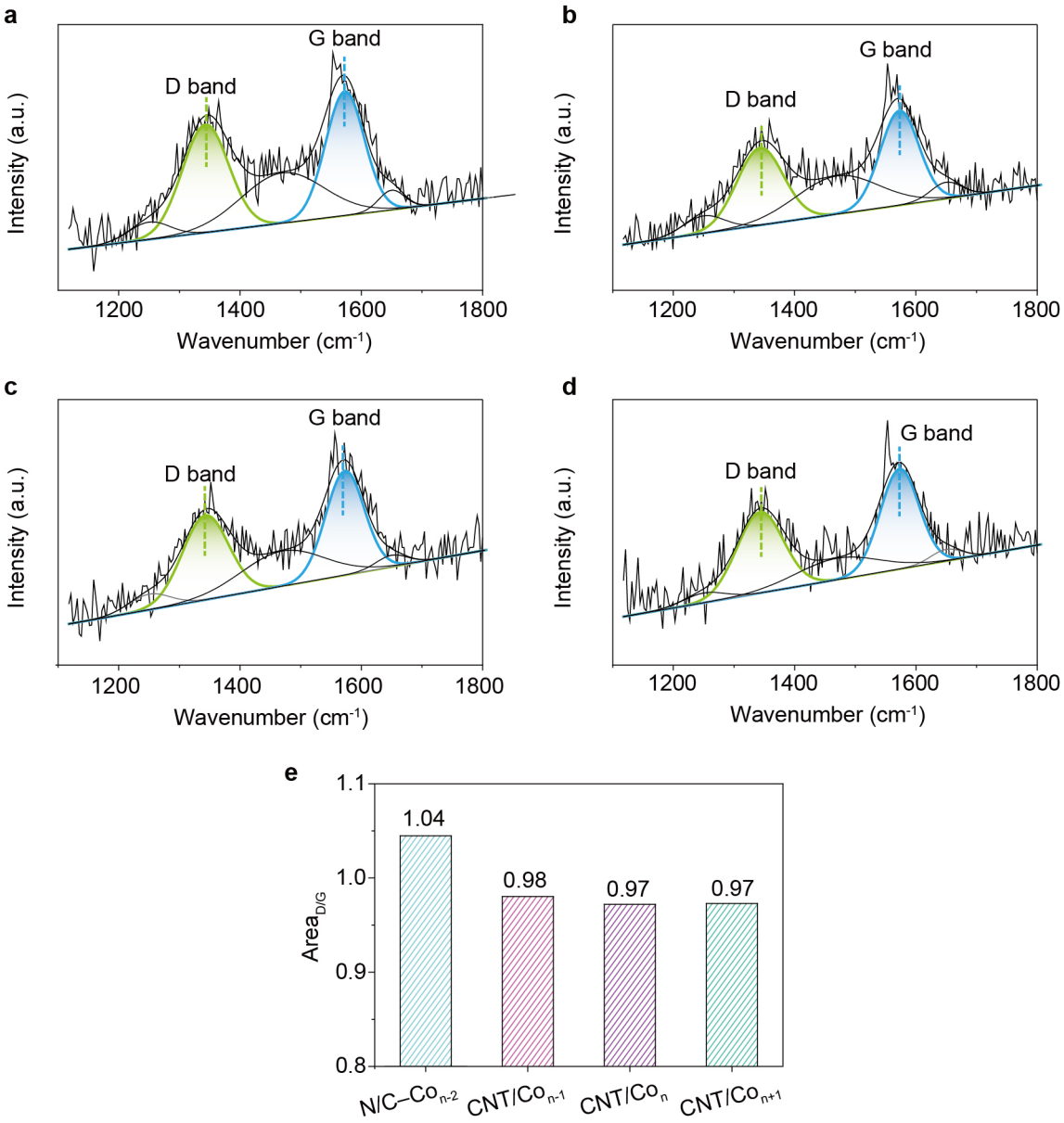

Figure S21. Raman spectrums for analysis of D band and G band from the catalysts of a) N/C–Co_{n-2}, b) CNT/Co_{n-1}, c) CNT/Co_n and d) CNT/Co_{n+1}. e) Area ratio of D band and G band for our catalysts. The similar value of $Area_{D/G}$ for CNT/Co_{n-1}, CNT/Co_n and CNT/Co_{n+1} can be observed, indicating nearly same degree of defects or graphitization toward carbon skeleton.

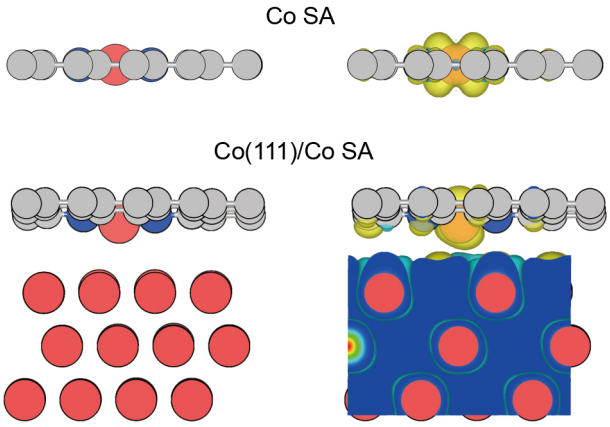

Figure S22. Spin density plots of Co SA and Co(111)/Co SA. Spin up and spin down are illustrated by the yellow and green cloud, respectively. Isosurface levels of the cloud are both set at 0.001. This results potentially unraveled that the spin charge around at Co SA is substantially remodeled by Co(111).

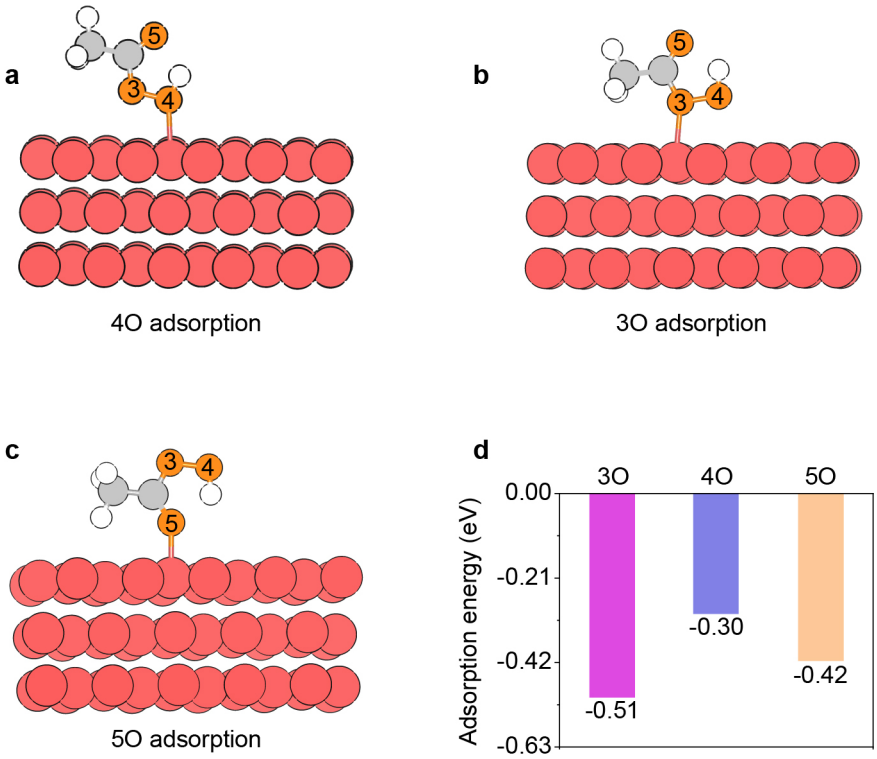

Figure S23. PAA adsorbed onto Co(111) plane in a) O4 site, b) O3 site and c) O5 site. d) Adsorption energy of O3, O4 and O5 of PAA adsorbed onto Co(111).

The results showed the most negative adsorption energy for 3O site in PAA. It indicated the beneficial adsorption of PAA's 3O by Co(111). It may be related to the fact that O3 site in PAA has a positive charge (Fig. S18), easier to obtain electron from the catalysts. This is consistent with the analysis of Bader charge transfer between Co–3O in Fig. 3e of main text. We thus discuss the adsorption of PAA's 3O subsequently.

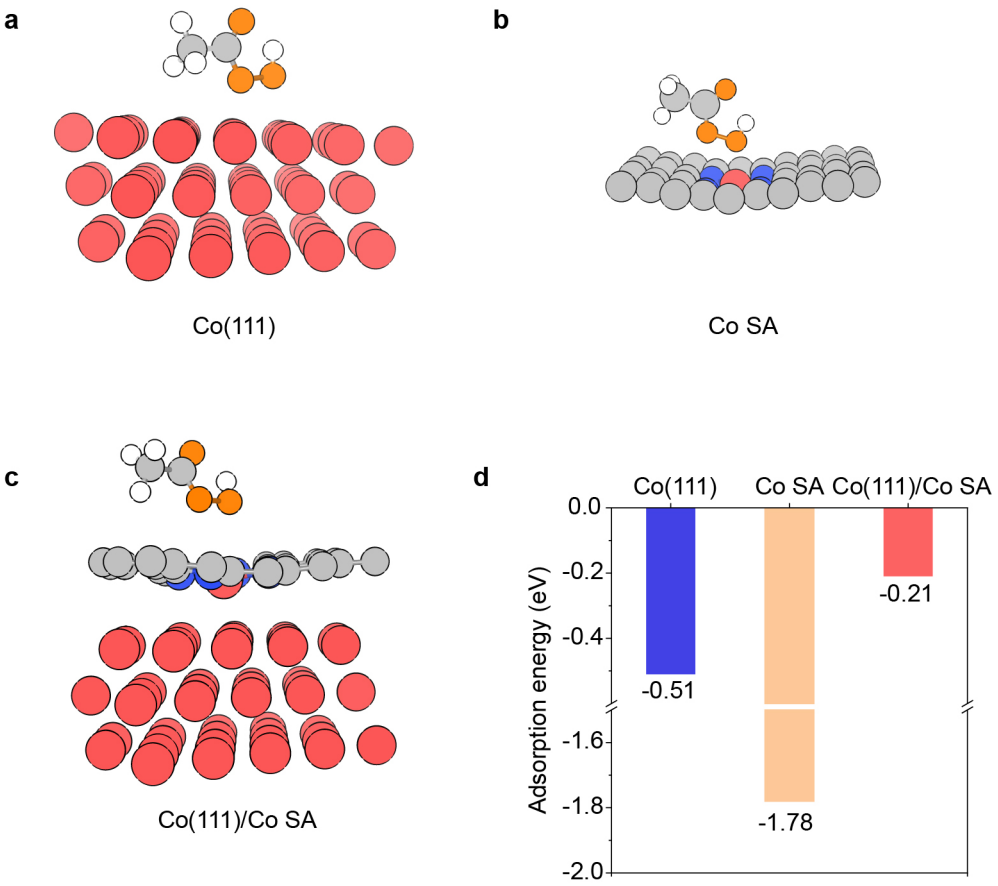

Figure S24. PAA adsorbed onto a) Co(111) plane, b) Co SA and c) Co(111)/Co SA site. d) Adsorption energy of PAA adsorbed onto Co(111) plane, Co SA and Co(111)/CoSA sites, respectively.

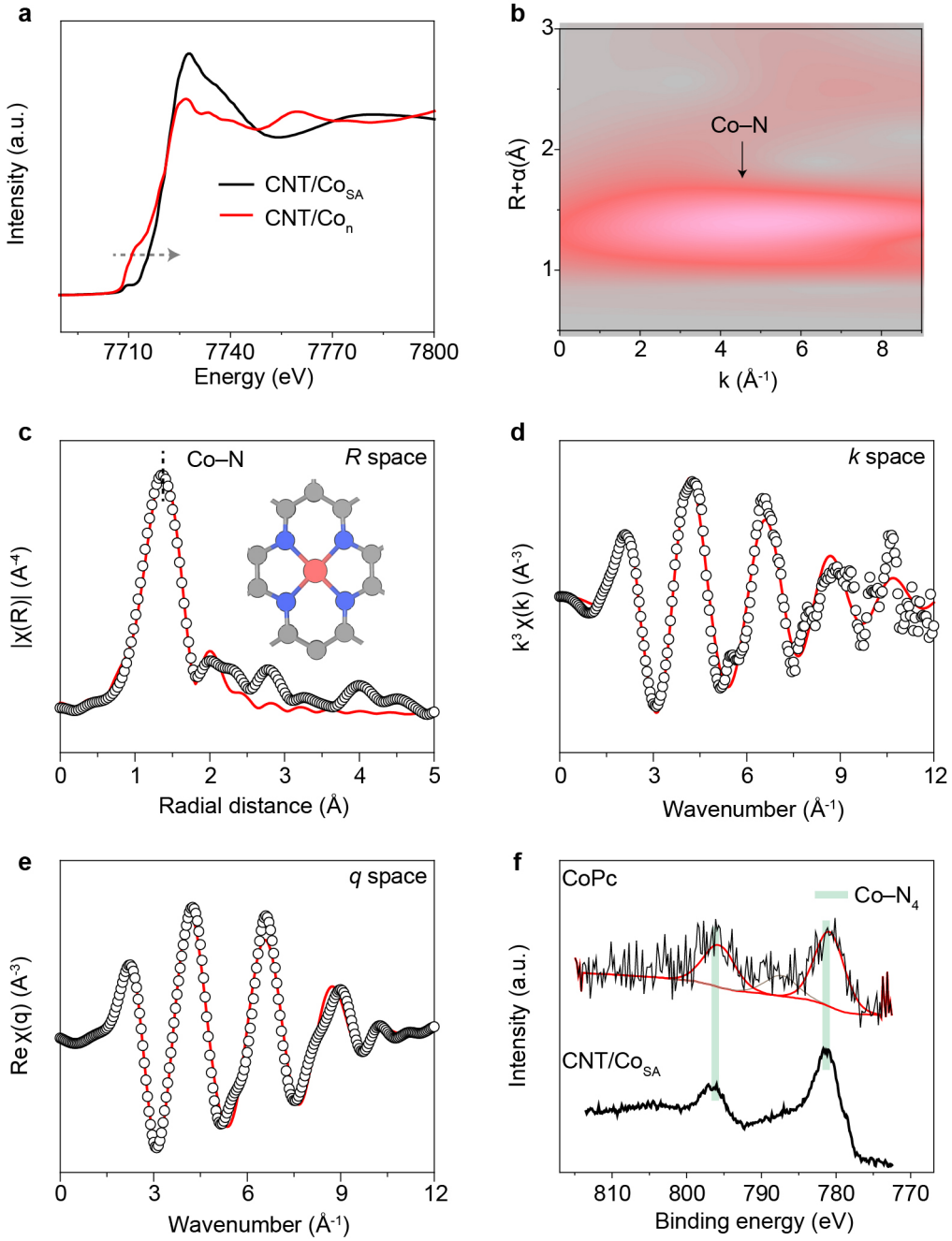

Figure S25. a) Co *K*–edge XANES of CNT/Co$_n$ and CNT/Co$_{SA}$. b) Wavelet–transform plots of the k^3–weighted EXAFS of Co K–edge for CNT/Co$_{SA}$. c to e) Experimental value and fitting value for FT–EXAFS spectra of CNT/Co$_{SA}$ at *R* space, *k* space and *q* space. The circle represents the experimental value, and the red line means the fitting value. f) High–resolution Co XPS spectrums of CNT/Co$_{SA}$ and the standard sample of cobalt phthalocyanine (CoPc).

A slightly positive toward CNT/Co$_n$ than that of CNT/Co$_{SA}$ for their near–edge absorption energy from Co *K*–edge XANES demonstrated the increasing average oxidation state for the former. It makes sense due to the removal of Co^0 species from the catalyst. A clear Co–N_4 coordination environment for Co motif in CNT/Co$_{SA}$ can be confirmed by analyzing the experimental and fitting FT–EXAFS curves of

the catalyst. Additionally, binding energy at ~781.3 eV and ~796.2 eV in high–resolution Co XPS spectra both pointed to Co–N bond by comparing the standard sample of cobalt phthalocyanine, also confirming the existence of Co–N motif.

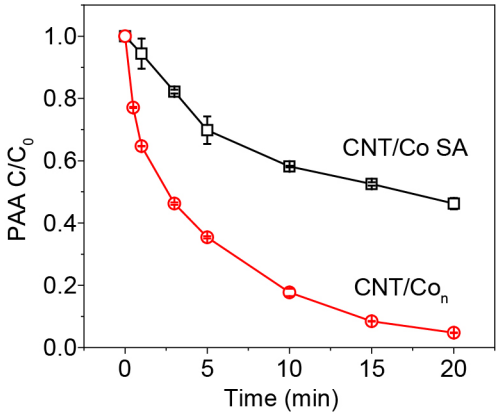

Figure S26. Time profile of PAA utilization via the catalysts of CNT/Co SA and CNT/Co_n. C means the concentration of PAA at intermediate reaction time and C_0 is the initial concentration of PAA. Reaction conditions: 10 mg L^{-1} catalysts, 200 μM PAA, 7.0±0.2 pH and room temperature.

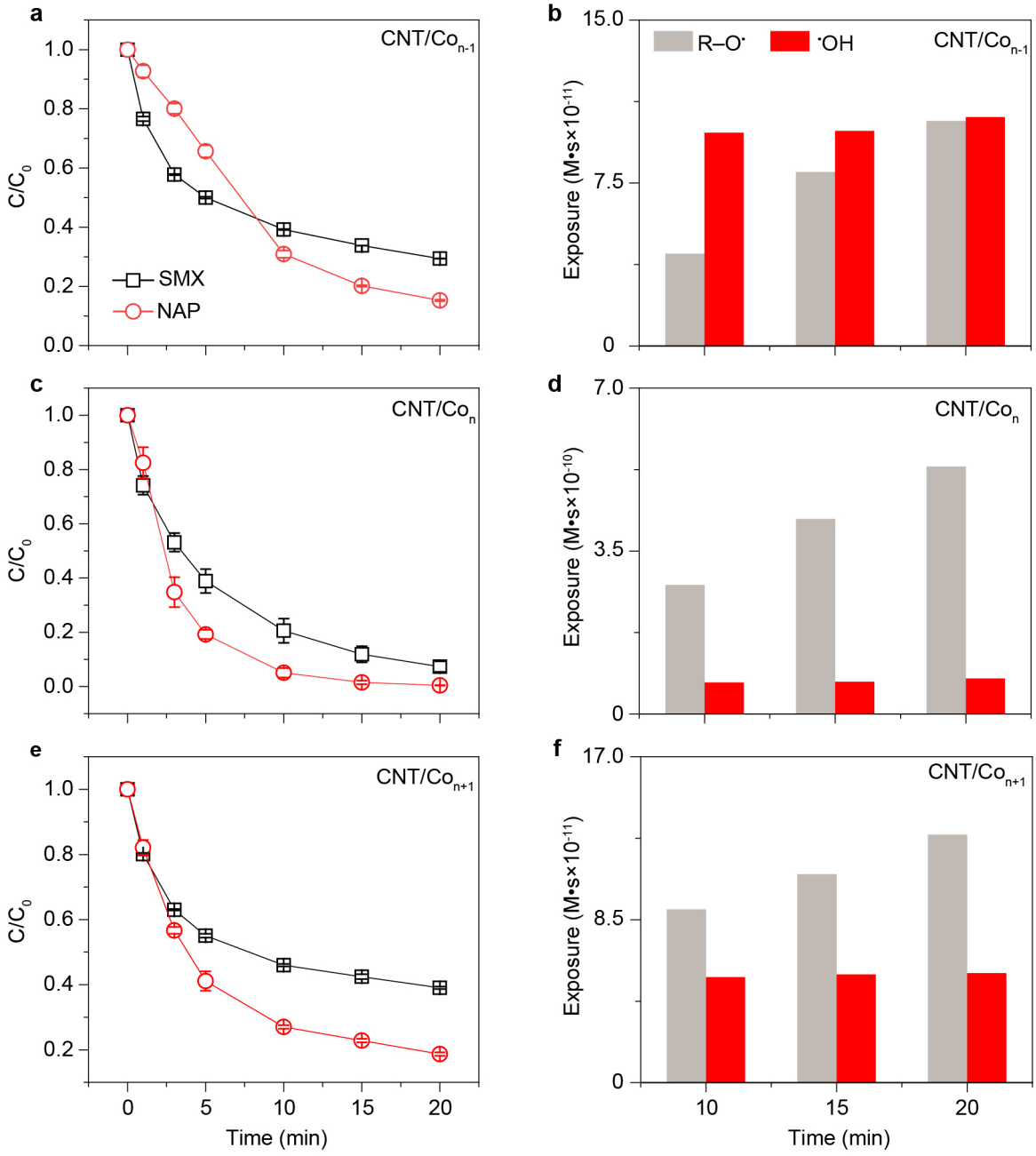

Figure S27. Time profile of SMX and naproxen (NAP) degradation in a) CNT/Co$_{n-1}$, c) CNT/Co$_n$ and e) CNT/Co$_{n+1}$ activating PAA systems. Reaction conditions: 10 mg L^{-1} catalysts, 200 μM PAA, 2.5 mg L^{-1} organic, 7.0±0.2 pH and room temperature. Exposure of R–O• and •OH in b) CNT/Co$_{n-1}$, d) CNT/Co$_n$ and f) CNT/Co$_{n+1}$ activating PAA systems based on the kinetic model analysis (see text S7. Kinetic model).

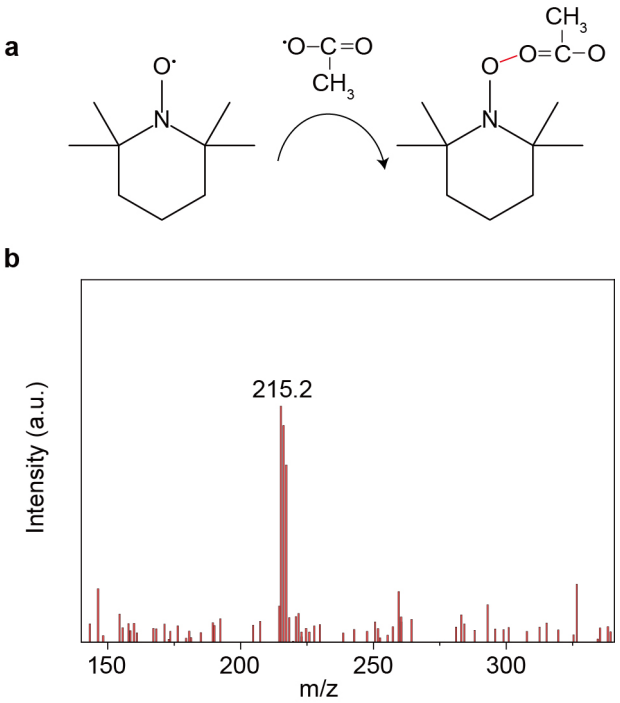

Figure S28. a) Schematical illustration for the reaction between TEMPO and $CH_3C(O)O^{\bullet}$. b) Mass spectroscopy detecting the product of TEMPO–$CH_3C(O)O$. Occurrence of 215.2 assigned to TEMPO–$CH_3C(O)O$ indicated the existence of $CH_3C(O)O^{\bullet}$ in CNT/Co_n/PAA system.

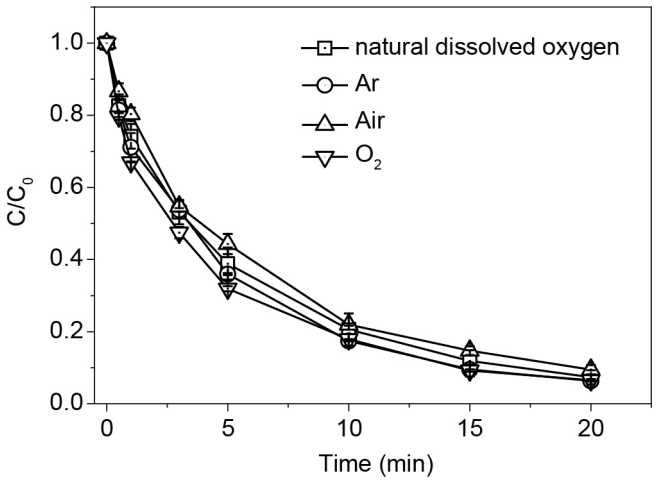

Figure S29. Time courses of SMX degradation in CNT/Co_n/PAA system under various concentrations of oxygen in reaction solution. Reaction conditions: 10 mg L^{-1} catalysts, 200 μM oxidants, 2.5 mg L^{-1} SMX, unadjusted pH value and room temperature.

The experimental results demonstrated that dissolved oxygen has no contribution to SMX removal in CNT/Co_n/PAA system, and indicated that $^{\bullet}CH_3$ may not be involved in this system, because $^{\bullet}CH_3$ can quickly react oxygen with a rate constant 4.7×10^9 $M^{-1}s^{-1}$ to consume the reactive species itself [14]. It is also consistent with the results of mass spectroscopy detecting the product in figure S28 above.

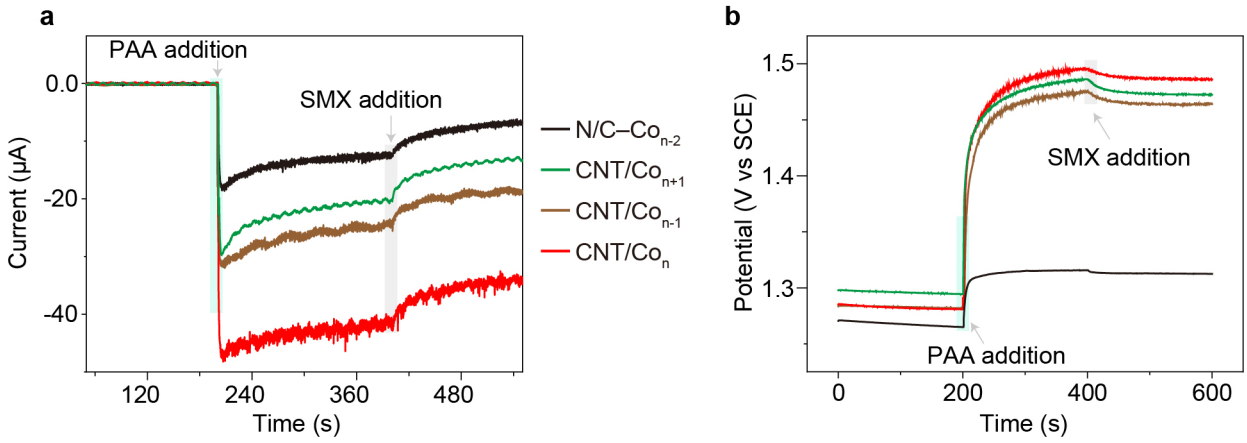

Figure S30. a) Amperometric current–time curves of CNT/Co$_n$ series in a three–electrode electrochemical system. PAA and SMX were added into the electrolyte at running times of approximately 200 s and 400 s, respectively. b) Open circuit potential–time curves of CNT/Co$_n$ series in a three–electrode electrochemical system. PAA and SMX were added into the electrolyte at running times of approximately 100 s and 200 s, respectively.

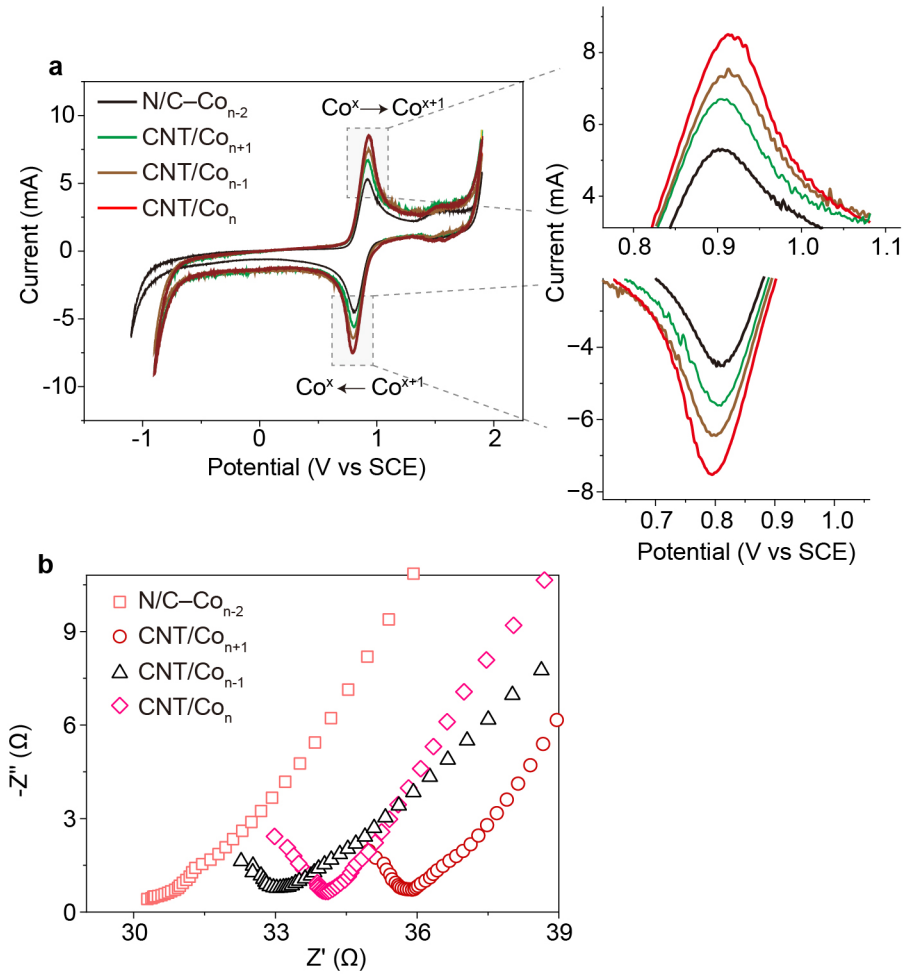

Figure S31. a) Cyclic voltammetry curves of CNT/Co$_n$ series in a three–electrode electrochemical system, electrolyte consisted of 1 M KCl and 10 mM $K_3[Fe(CN)_6]$ solution. b) Electrochemical impedance spectroscopy measurements of CNT/Co$_n$ series in a three–electrode electrochemical system.

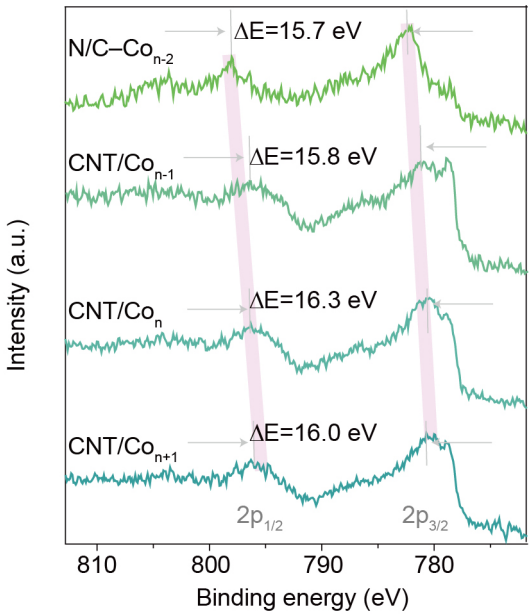

Figure S32. High–resolution Co XPS spectra of CNT/Co$_n$ series.

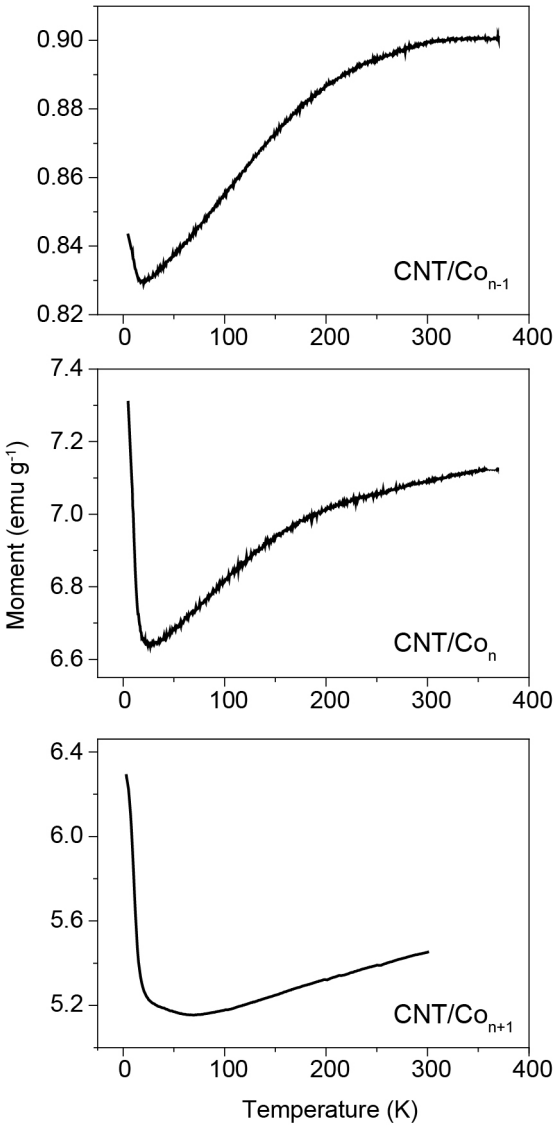

Figure S33. Zero–field cooling curves of the catalysts under 1 kOe.

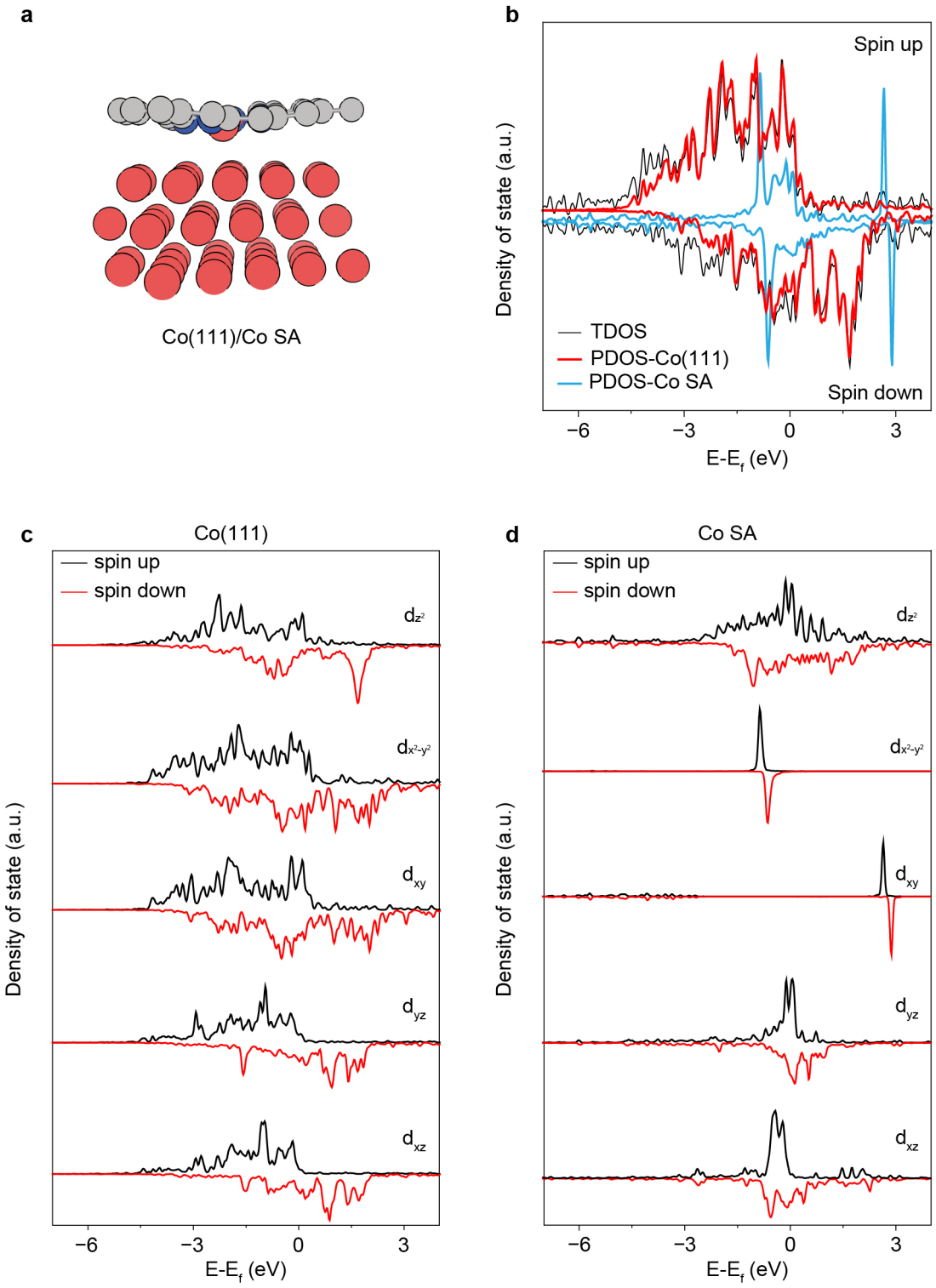

Figure S34. a) Schematical illustration of the model of unstrained Co(111)/Co SA . b) Total density of states (TDOS) of the Co(111)/Co SA and projected DOS of Co(111) and Co SA. c and d) DOS of d_{z2}, d_{x2-y2} d_{xy}, d_{yz} and d_{xz} for Co(111) and Co SA. According to Fig. S34b, we can find that the TDOS of Co(111)/Co SA is nearly totally contributed by Co(111).

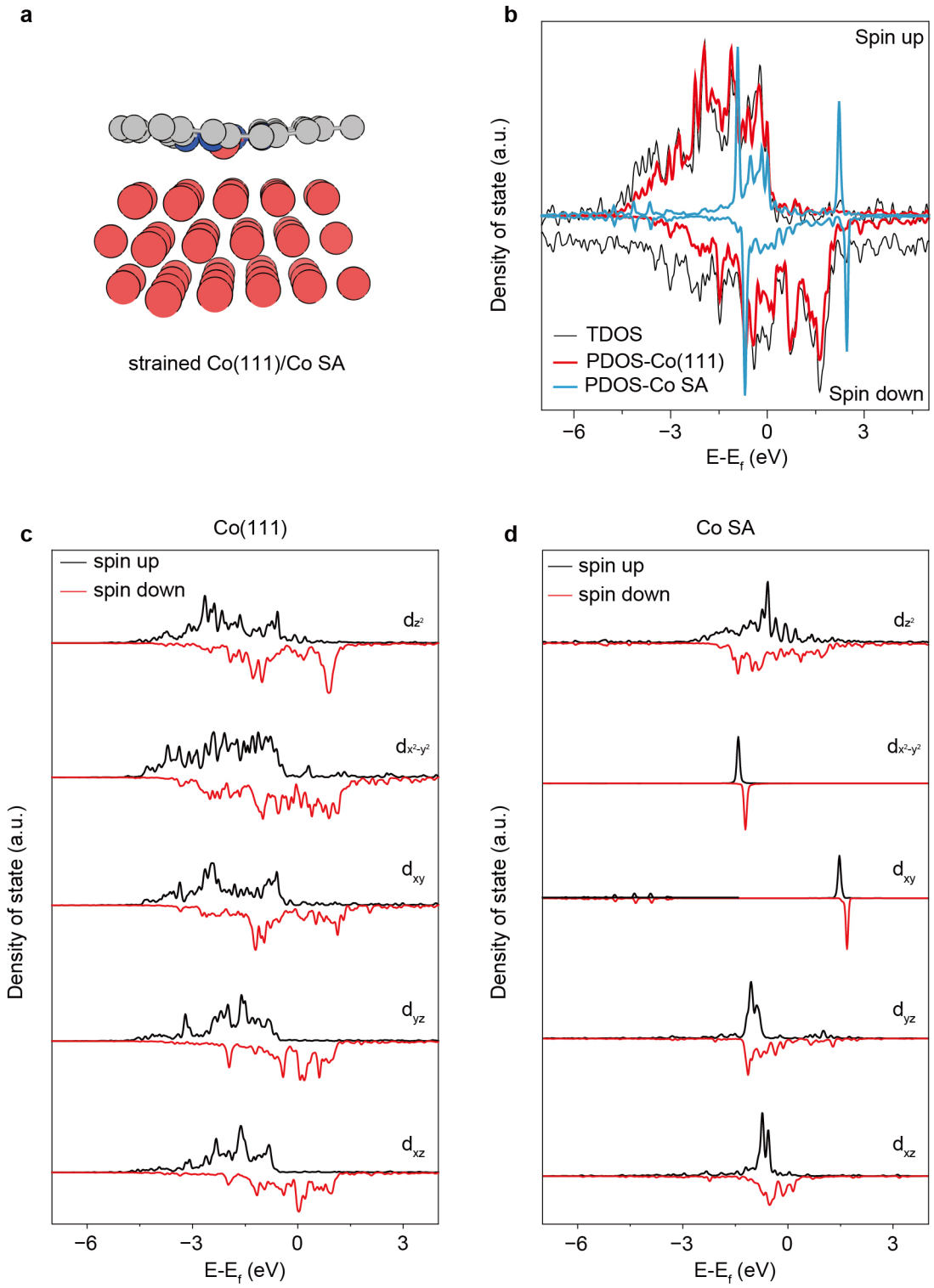

Figure S35. a) Schematical illustration of the model of 7%–strained Co(111)/Co SA . b) Total density of states (TDOS) of the Co(111)/Co SA and projected DOS of Co(111) and Co SA. c and d) DOS of d_{z2}, d_{x2-y2} d_{xy}, d_{yz} and d_{xz} for Co(111) and Co SA.

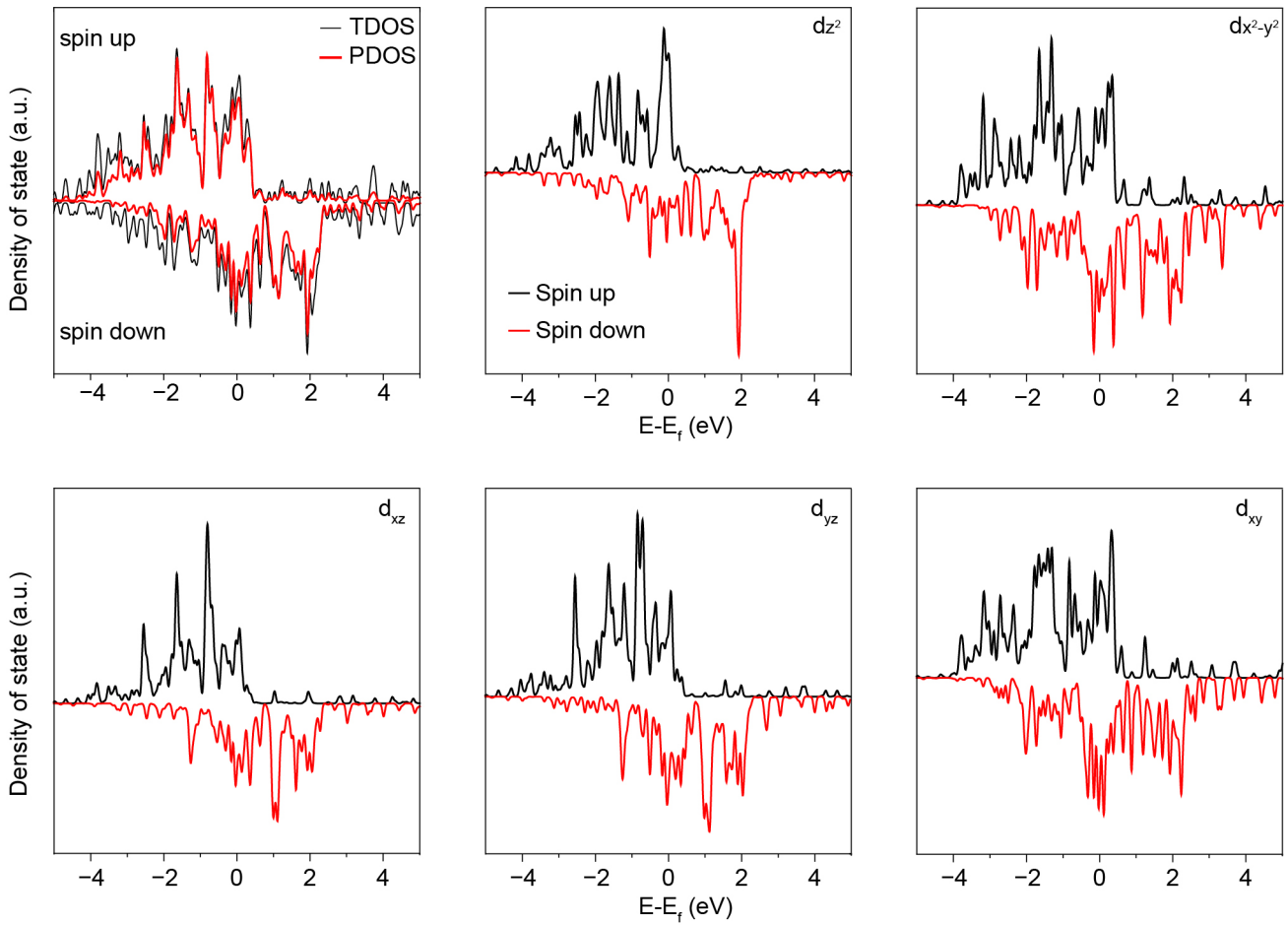

Figure S36. Total DOS and projected DOS of 1%–strained Co(111).

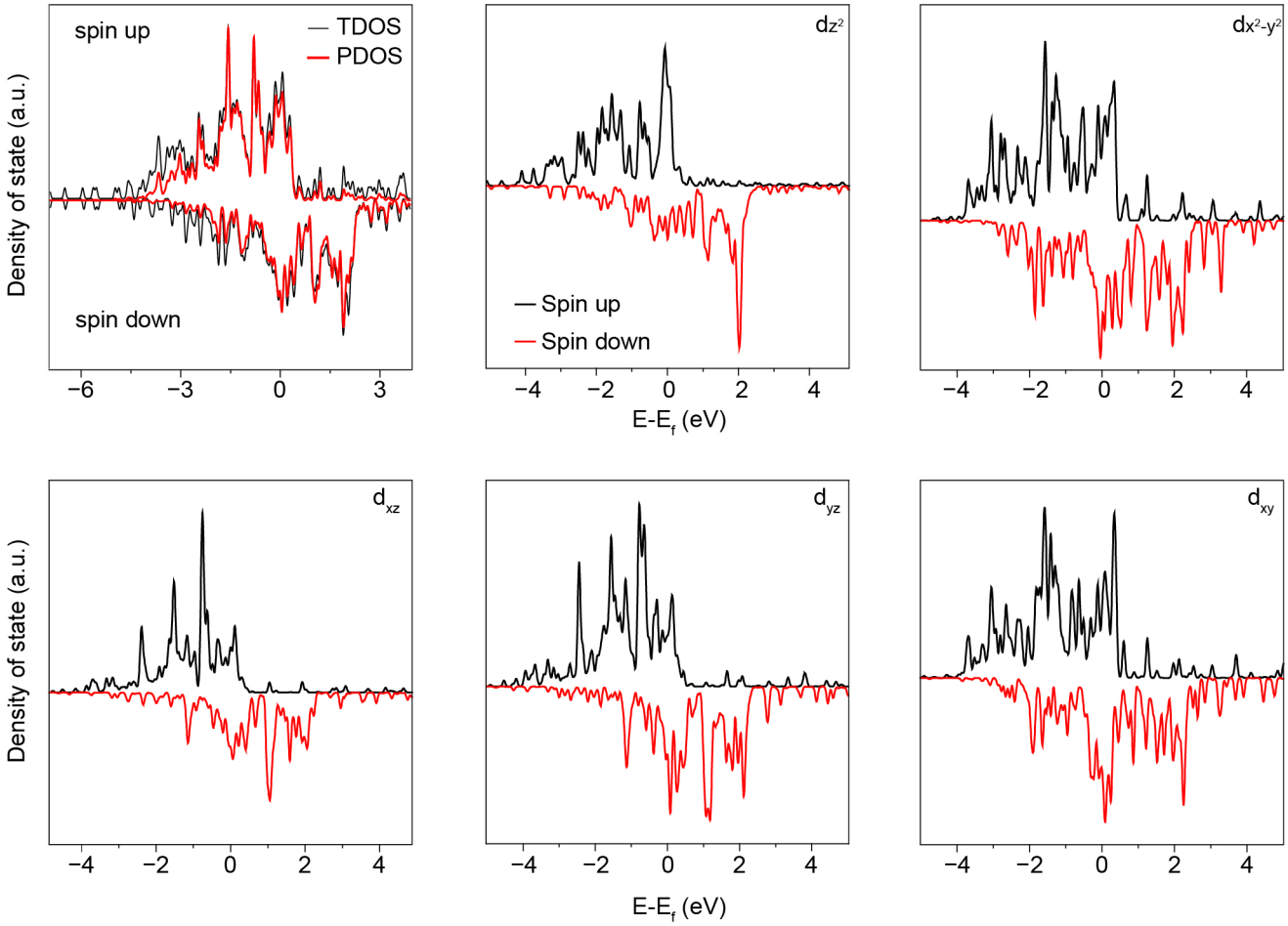

Figure S37. Total DOS and projected DOS of 3%–strained Co(111).

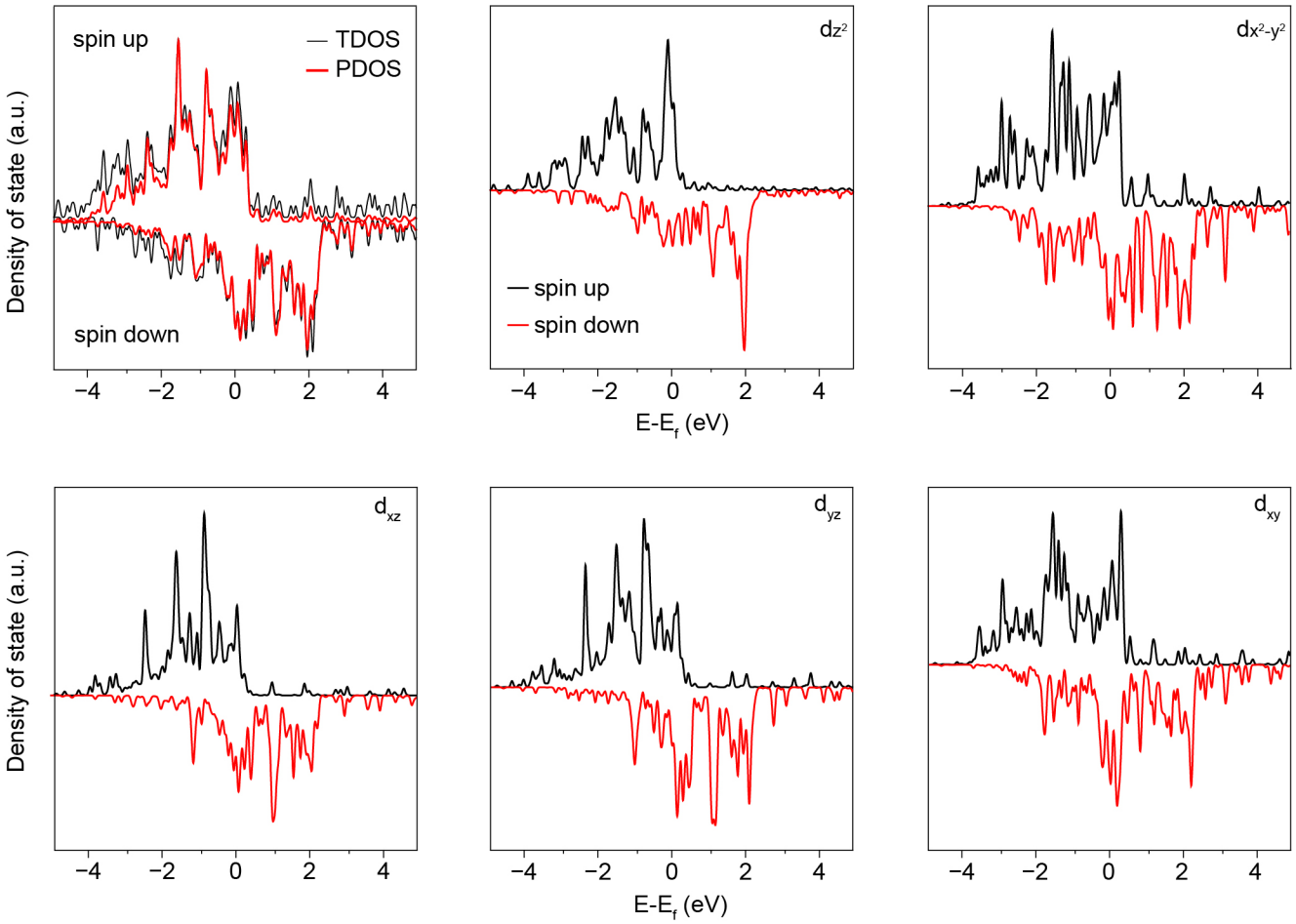

Figure S38. Total DOS and projected DOS of 5%–strained Co(111).

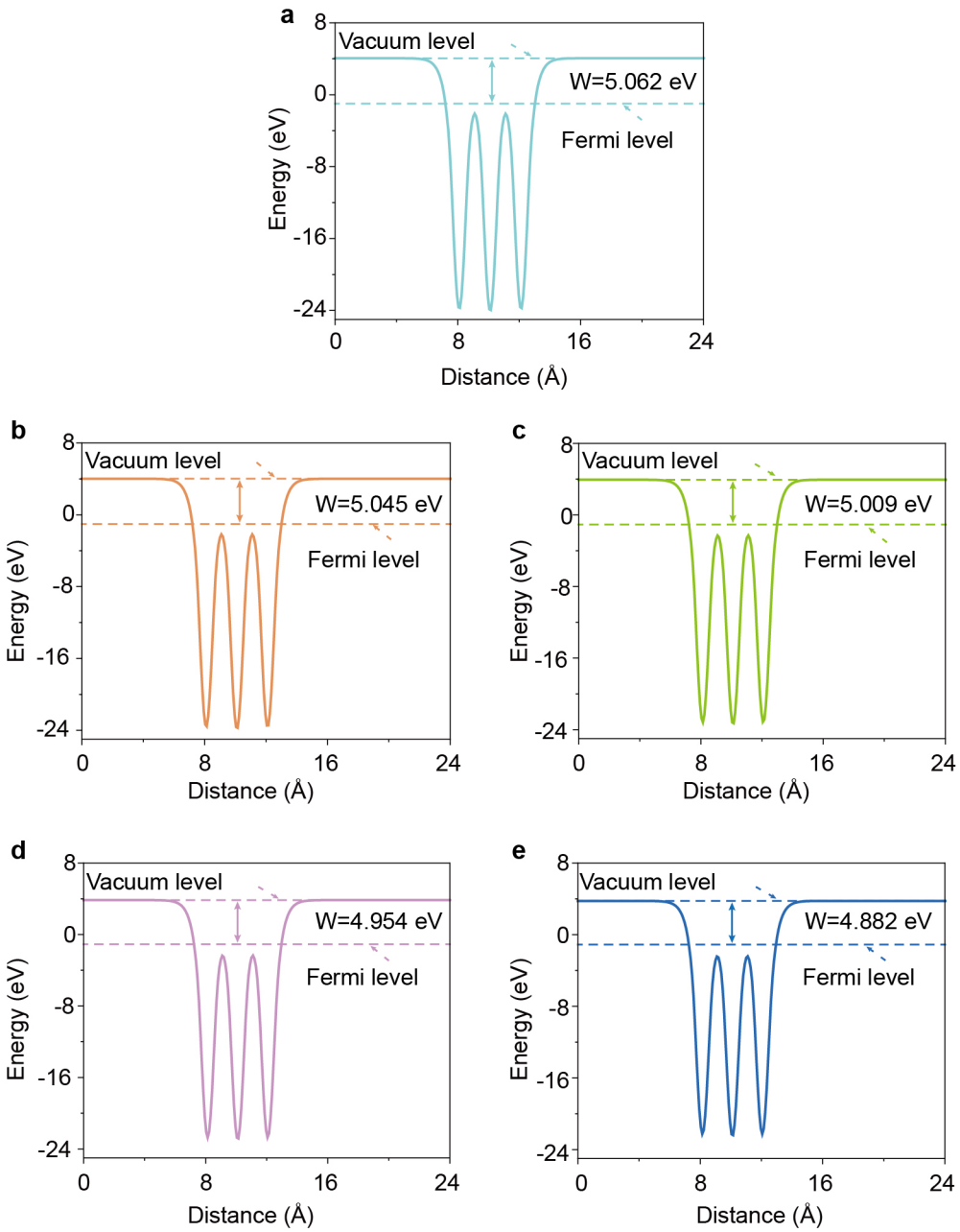

Figure S39. Work function of a) unstrained Co(111), b) 1%–strained Co(111), c) 3%–strained Co(111), d) 5%–strained Co(111) and e) 7%–strained Co(111).

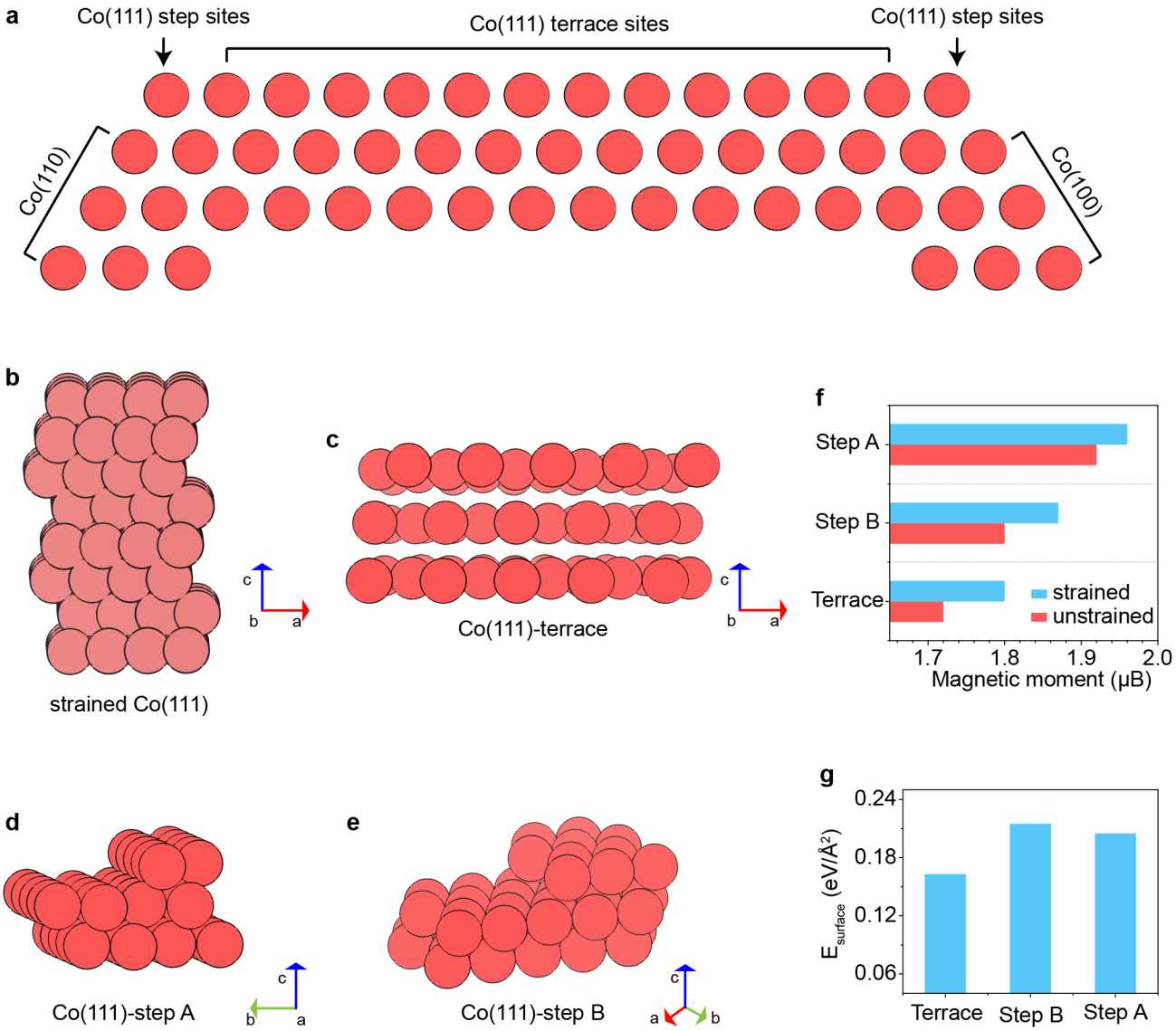

Figure S40. a) Configuration of Co(111) lattice plane and its terrace sites and Co(111) step A and B sites, obtained by the build Wulff construction of fcc–cobalt. b) Configuration of strained Co(111) lattice plane. Configuration of strained Co(111) of c) terrace site, d) step A site and e) step B site. f) Magnetic moments of terrace site, step A site and site B step in Co(111) with and without 7% strain. g) Surface energy of terrace site, step A site and step B site in Co(111) lattice plane.

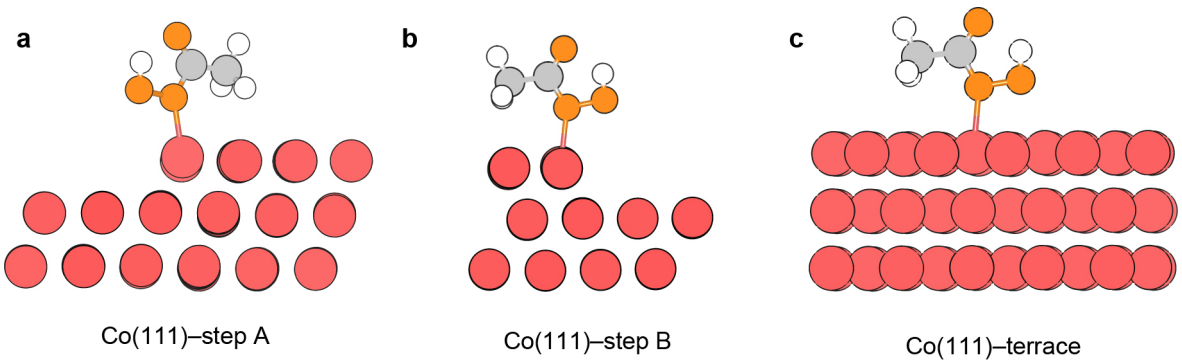

Figure S41. PAA adsorbed onto a) step A, b) step B and c) terrace site in Co(111).

a

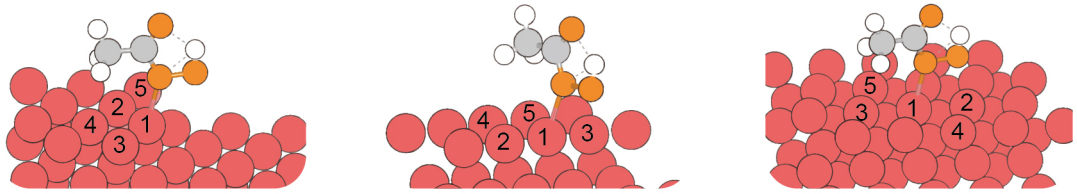

b

Bader charge									
	terrace			step A			step B		
Co	before	after	Δ	before	after	Δ	before	after	Δ
1	8.9	9.02	-0.12	8.81	8.99	-0.18	8.85	9	-0.15
2	8.96	9.02	-0.06	9.01	9.04	-0.03	8.99	9	-0.01
3	9.03	9.02	0.01	9.05	9.01	0.04	8.98	9	-0.02
4	8.99	9.02	-0.03	9.03	9	0.03	9	8.99	0.01
5	9.03	9.02	0.01	9	9.01	-0.01	9	8.99	0.01
net spin charge									
1	1.8	1.79	0.01	1.93	1.89	0.04	1.87	1.84	0.03
2	1.8	1.81	-0.01	1.78	1.78	0	1.87	1.88	-0.01
3	1.8	1.77	0.03	1.77	1.77	0	1.87	1.88	-0.01
4	1.8	1.81	-0.01	1.73	1.73	0	1.9	1.89	0.01
5	1.8	1.79	0.01	1.93	1.92	0.01	1.9	1.89	0.01

Figure S42. a) Schematical illustration of the cobalt sites adsorbed by PAA molecule from step A, step B and terrace site in Co(111). b) The detailed values of Bader charge and net spin charge for the cobalt sites after and before PAA molecule adsorption, the figure unit, |e|.

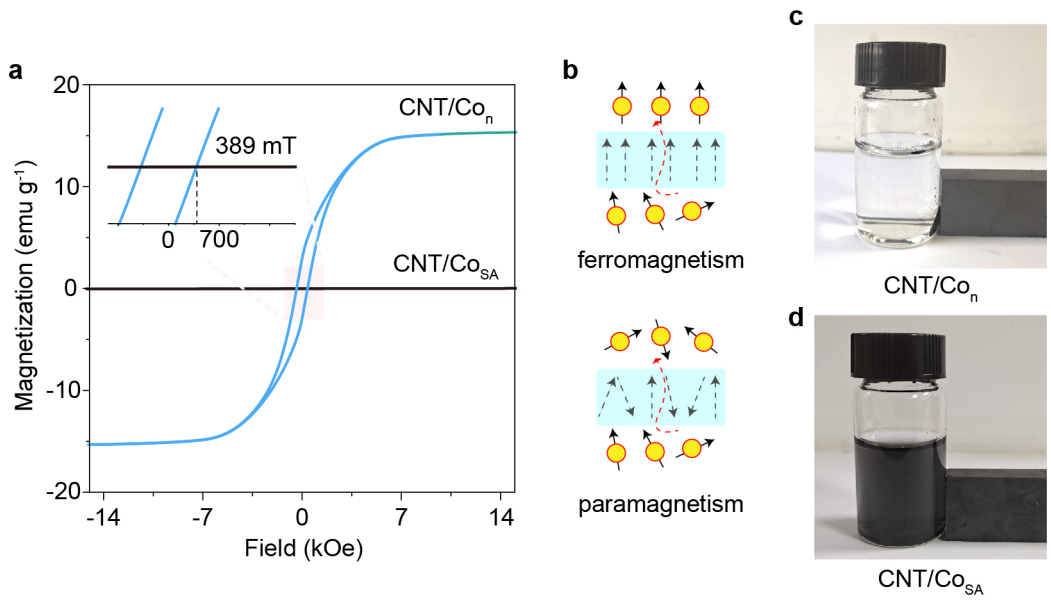

Figure S43. a) Magnetization curves of CNT/Co$_n$ and CNT/Co$_{SA}$ under room temperature. b) Schematical illustrations of ferromagnetic domain and paramagnetic domain under MF and the corresponding polarized electron generation. Digital photos of c) CNT/Co$_n$ and d) CNT/Co$_{SA}$ surrounding a permanent magnet in 30 minutes. Nearly full separation of CNT/Co$_n$ from the liquid with assistance of magnetic field indicating its ferromagnetism.

These results indicate ferromagnetic behavior for CNT/Co$_n$ with saturation magnetization (M_s) of 15 emu g^{-1} and coercive field (H_c) 389 mT, and paramagnetic behavior for CNT/Co$_{SA}$.

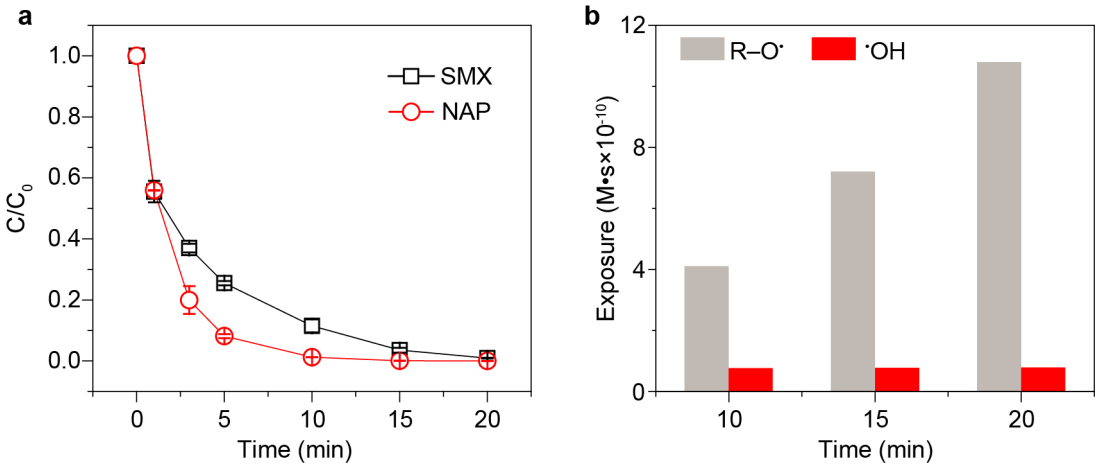

Figure S44. Time profile of SMX and naproxen (NAP) degradation in a) CNT/Co$_n$ with 240 mT magnetic field. Reaction conditions: 10 mg L^{-1} catalysts, 200 μM PAA, 7.0±0.2 pH, 2.5 mg L^{-1} organic and room temperature. b) Exposure of R–O• and •OH in figure a based on the kinetic model analysis (see text S7. Kinetic model).

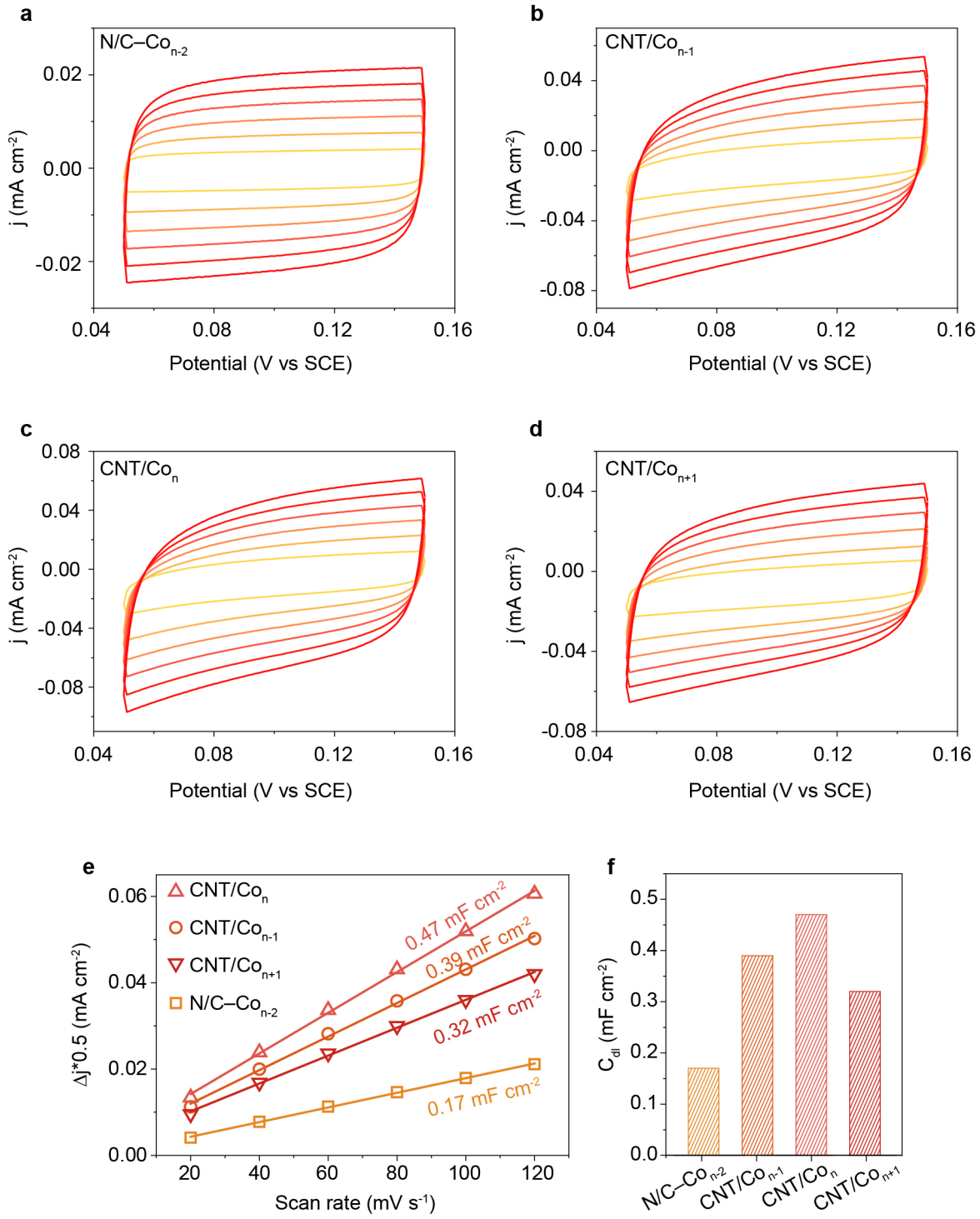

Figure S45. a to d) Cyclic voltammetry curves of CNT/Co_n series operated by the non–Faradaic potential region at varying scan rates in a three–electrode electrochemical system. e) The calculated double–layer capacitance (C_{dl}) of CNT/Co_n series. f) Comparison of C_{dl} from the CNT/Co_n series.

Electrochemically active surface area (ECSA) of the catalysts can be calculated by the equation, $ECSA=C_{dl}/C_s$. Due to the same C_s (a specific capacitance) in the above processes, we quantify the ECSA by comparing the C_{dl} values.

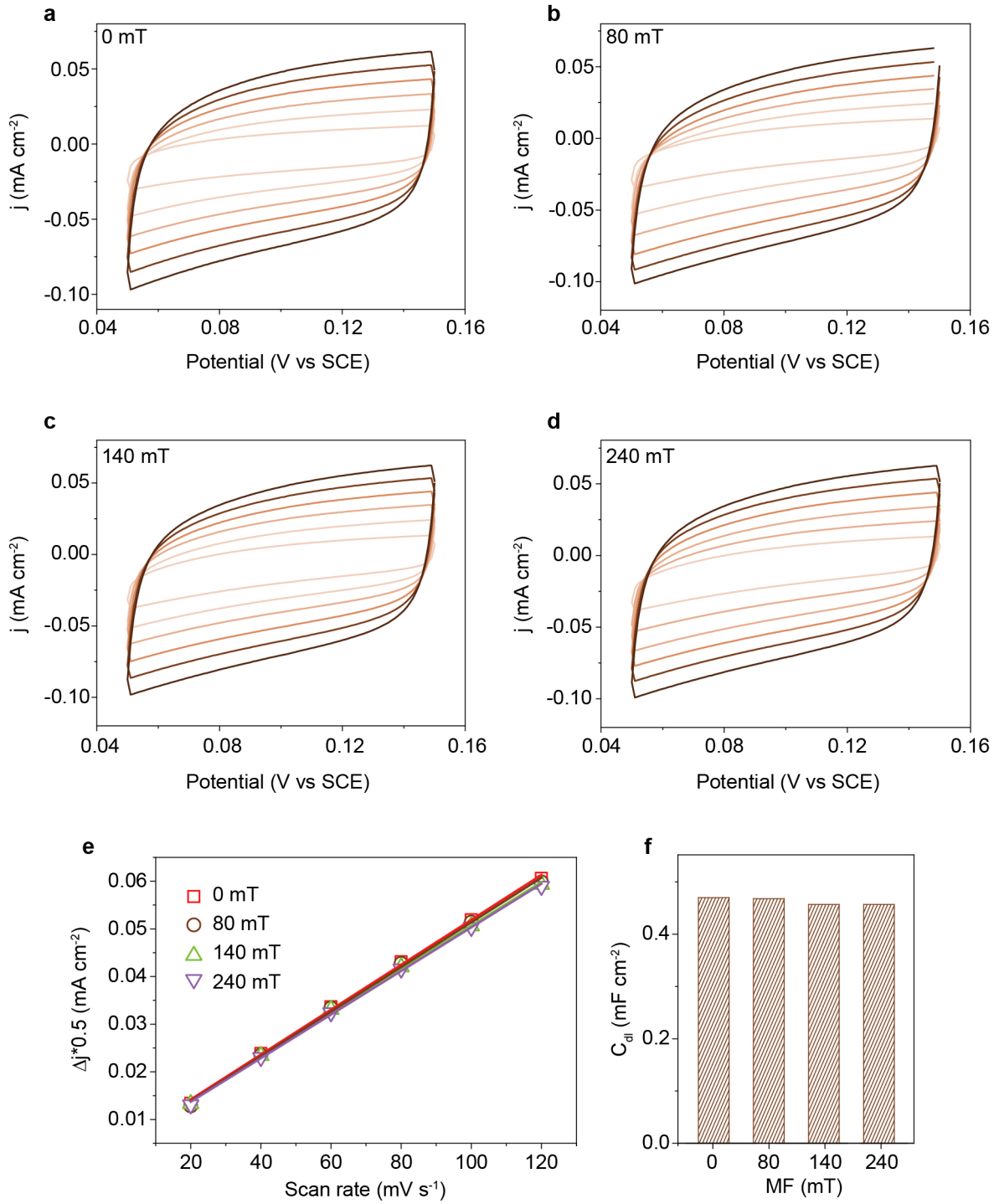

Figure S46. a to d) Cyclic voltammetry curves of CNT/Co_n operated by the non–Faradaic potential region at varying scan rates and MF in a three–electrode electrochemical system. e) The calculated double–layer capacitance (C_{dl}) of CNT/$Co_{1\&n}$ series. f) Comparison of C_{dl} from the CNT/Co_n with varying MF. The nearly stable C_{dl} for CNT/Co_n with varied MF hint that MF does not hatch newborn active sites in the catalyst.

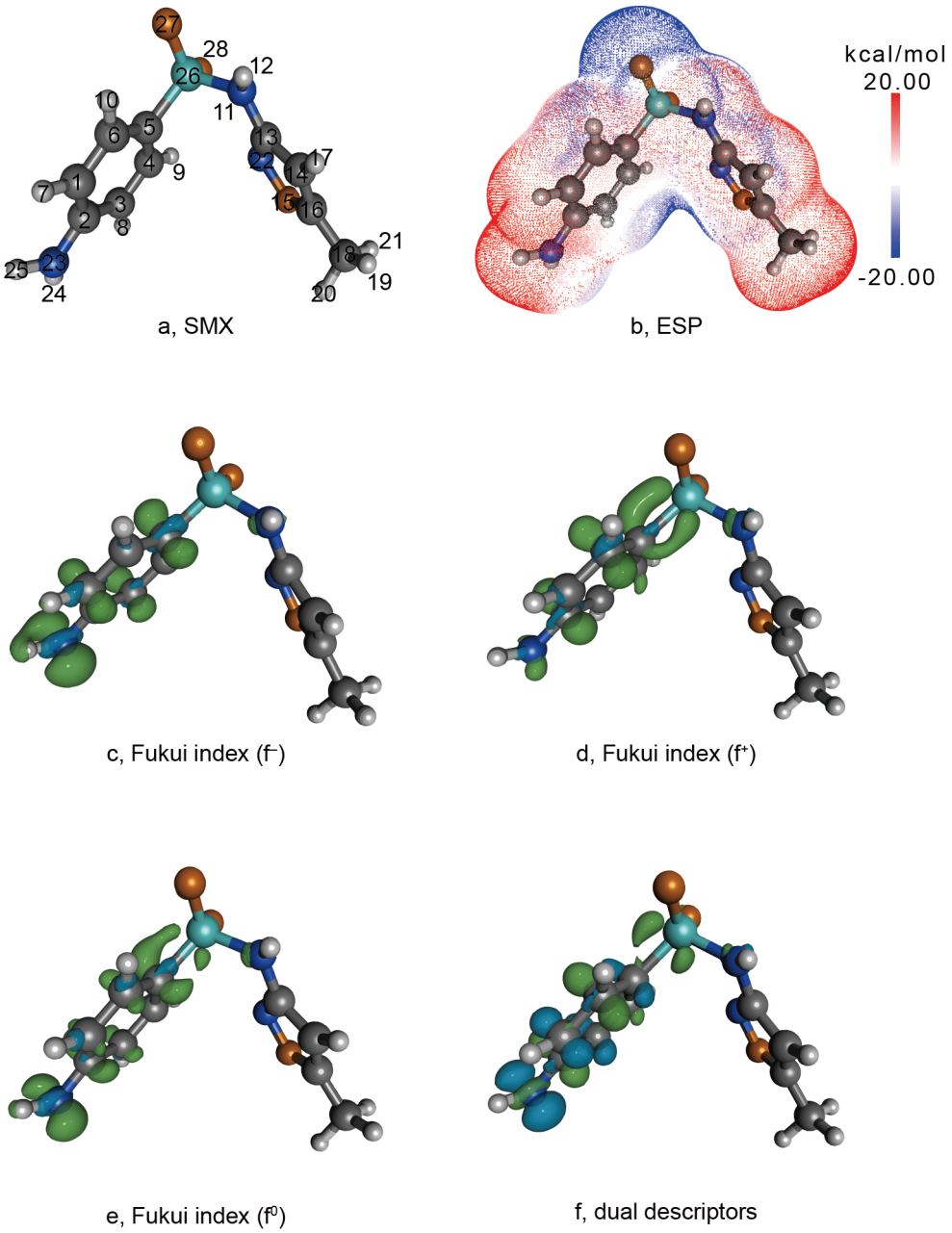

Figure S47. a) Optimized molecular structure of SMX. b) Electrostatic potential (ESP) of SMX. Fukui index c) f^-, d) f^+ and e) f^0 of SMX and f) its dual descriptions (DD).

We analyzed the atomic level chemical properties of SMX in DFT to better understand the cleavage sites of SMX in our system. The Fukui function and dual description (DD) are used to predict the possible attack means including nucleophilic attack, electrophilic attack and radical attack. Fukui index (f^+) is used to predict nucleophilic attack sites of SMX, and f^- and f^0 are related with electrophilic attack and radical attack sites of SMX. There parameters of SMX have been calculated to display in table S4 below, such as 23N site in SMX with the highest f^0 for easier radical attack.

Table S4. Chemical properties of each atom in SMX based on DFT analysis

Atom index	Electrophilicity (eV)	Nucleophilicity (eV)	f^-	f^+	f^0	DD
1C	0.0871	0.16636	0.1004	0.0571	0.0788	-0.0433
2C	0.15606	0.11589	0.0699	0.1024	0.0862	0.0324
3C	0.07652	0.15866	0.0958	0.0502	0.073	-0.0456
4C	0.16101	0.06564	0.0396	0.1056	0.0726	0.066
5C	0.10419	0.15325	0.0925	0.0684	0.0804	-0.0241
6C	0.09799	0.06274	0.0379	0.0643	0.0511	0.0264
7H	0.04826	0.06236	0.0376	0.0317	0.0346	-0.006
8H	0.04131	0.06049	0.0365	0.0271	0.0318	-0.0094
9H	0.07422	0.03769	0.0227	0.0487	0.0357	0.0259
10H	0.04724	0.03613	0.0218	0.031	0.0264	0.0092
11N	0.03956	0.02764	0.0167	0.026	0.0213	0.0093
12H	0.02821	0.01432	0.0086	0.0185	0.0136	0.0099
13C	0.01765	0.00501	0.003	0.0116	0.0073	0.0086
14C	0.01419	0.00691	0.0042	0.0093	0.0067	0.0051
15O	0.02056	0.00953	0.0058	0.0135	0.0096	0.0077
16C	0.01575	0.00637	0.0038	0.0103	0.0071	0.0065
17H	0.00849	0.00401	0.0024	0.0056	0.004	0.0031
18C	0.00508	0.00225	0.0014	0.0033	0.0023	0.002
19H	0.00415	0.00154	0.0009	0.0027	0.0018	0.0018
20H	0.00438	0.00201	0.0012	0.0029	0.002	0.0017
21H	0.00317	0.00156	0.0009	0.0021	0.0015	0.0011
22N	0.02637	0.009	0.0054	0.0173	0.0114	0.0119
23N	0.08816	0.31788	0.1919	0.0578	0.1248	-0.134
24H	0.04375	0.10345	0.0624	0.0287	0.0456	-0.0337
25H	0.04711	0.10331	0.0624	0.0309	0.0466	-0.0314
26S	0.11539	0.03641	0.022	0.0757	0.0488	0.0537
27O	0.0771	0.04395	0.0265	0.0506	0.0386	0.0241
28O	0.07084	0.04241	0.0256	0.0465	0.036	0.0209

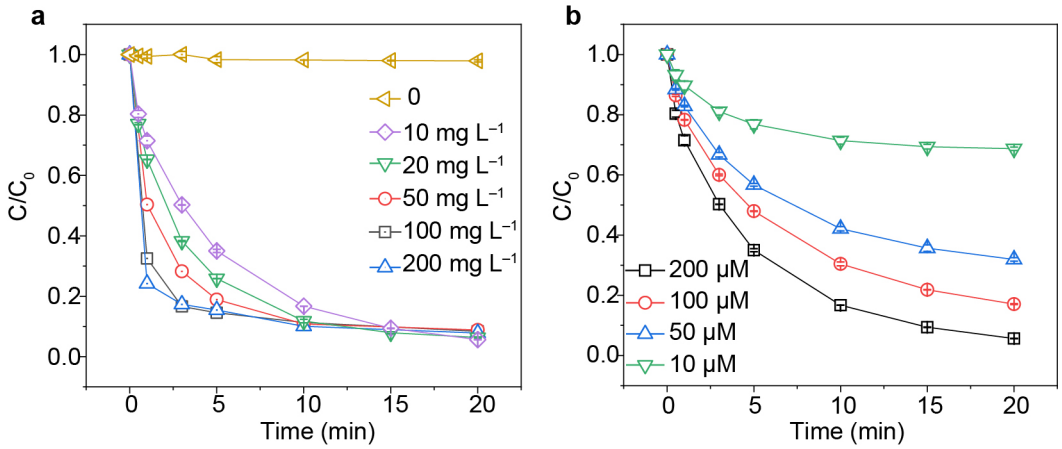

Figure S48. Time profiles of SMX degradation in CNT/Co_n/PAA system under varying dosage of a) CNT/Co_n and b) PAA. Reaction conditions: 0–100 mg L^{-1} CNT/Co_n, 10–200 μM PAA, 2.5 mg L^{-1} SMX, 7.0±0.2 pH and room temperature.

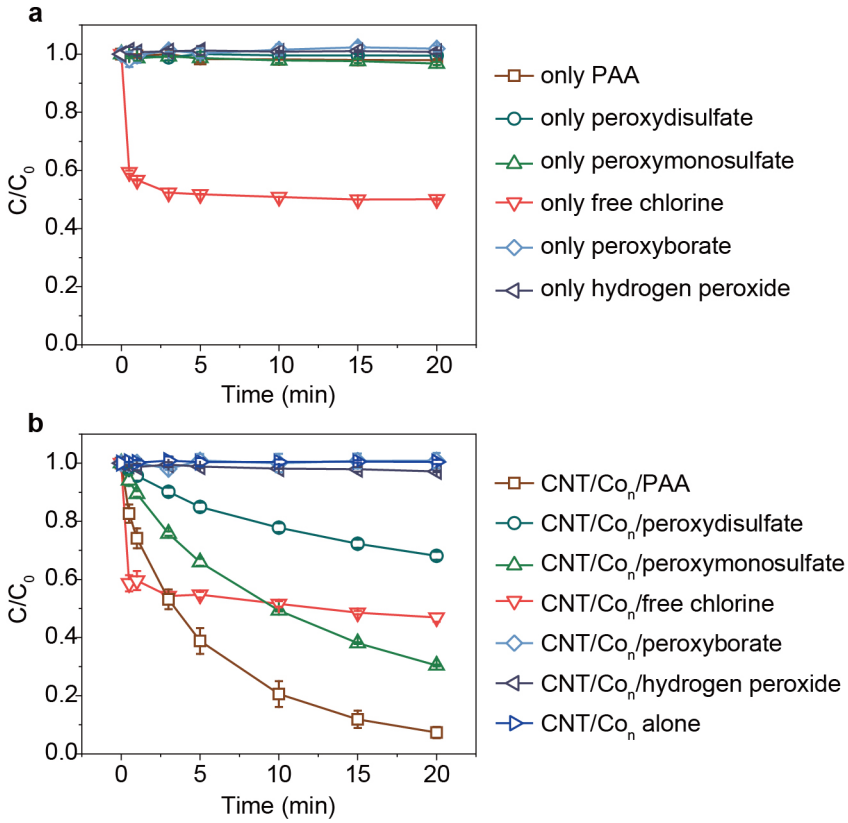

Figure S49. a) Time courses of SMX degradation in oxidants alone. Reaction conditions: 200 μM oxidants, 2.5 mg L^{-1} SMX, unadjusted pH value and room temperature, oxidants including PAA, peroxydisulfate, peroxymonosulfate, free chlorine, peroxyborate and hydrogen peroxide. b) Time courses of SMX degradation in CNT/Co_n activating oxidants. Reaction conditions: 10 mg L^{-1} catalysts, 200 μM oxidants (if needed), 2.5 mg L^{-1} SMX, unadjusted pH value and room temperature.

Notably, CNT/Co_n alone cannot effectively remove the SMX, highlighting the importance contribution of oxidants including PAA toward SMX removal. CNT/Co_n activating hydrogen peroxide

(H_2O_2) did not display effective removal of SMX during reaction, indicating that the contribution of H_2O_2 toward SMX removal is negligible.

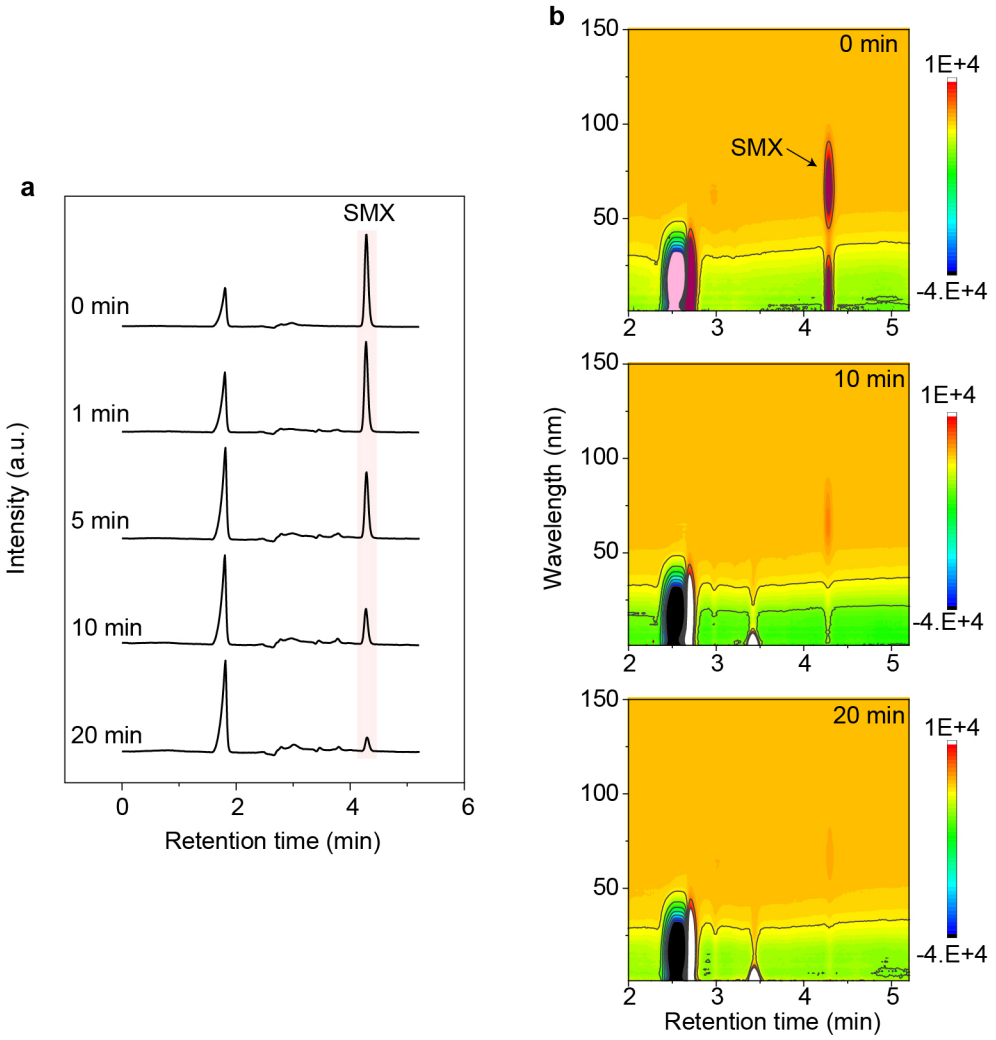

Figure S50. HPLC recording the time profiles of SMX abatement by CNT/Co_n/PAA system in a) two–dimensional and b) three–dimensional spectroscopy.

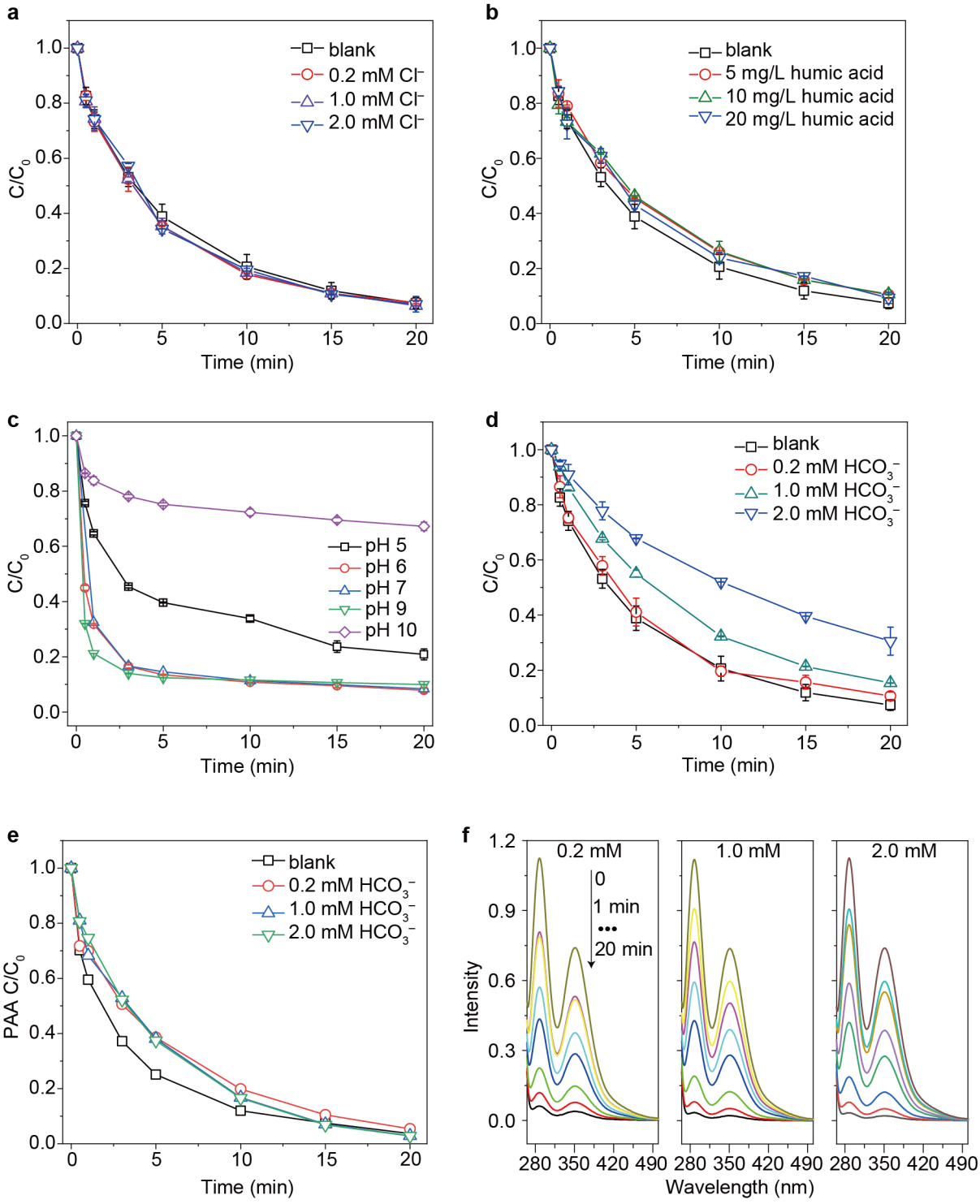

Figure S51. Time profiles of SMX degradation in CNT/Co_n/PAA system under varying concentration of a) Cl^-, b) humic acid, c) pH values and d) HCO_3^-. e) Time profile of PAA decay from the system of figure S51d. f) UV–vis absorption spectra of I_3^- to quantify the concentration change of PAA in the systems of figure S51e. Reaction conditions: 10 mg L^{-1} CNT/Co_n, 200 μM PAA, 2.5 mg L^{-1} SMX and room temperature.

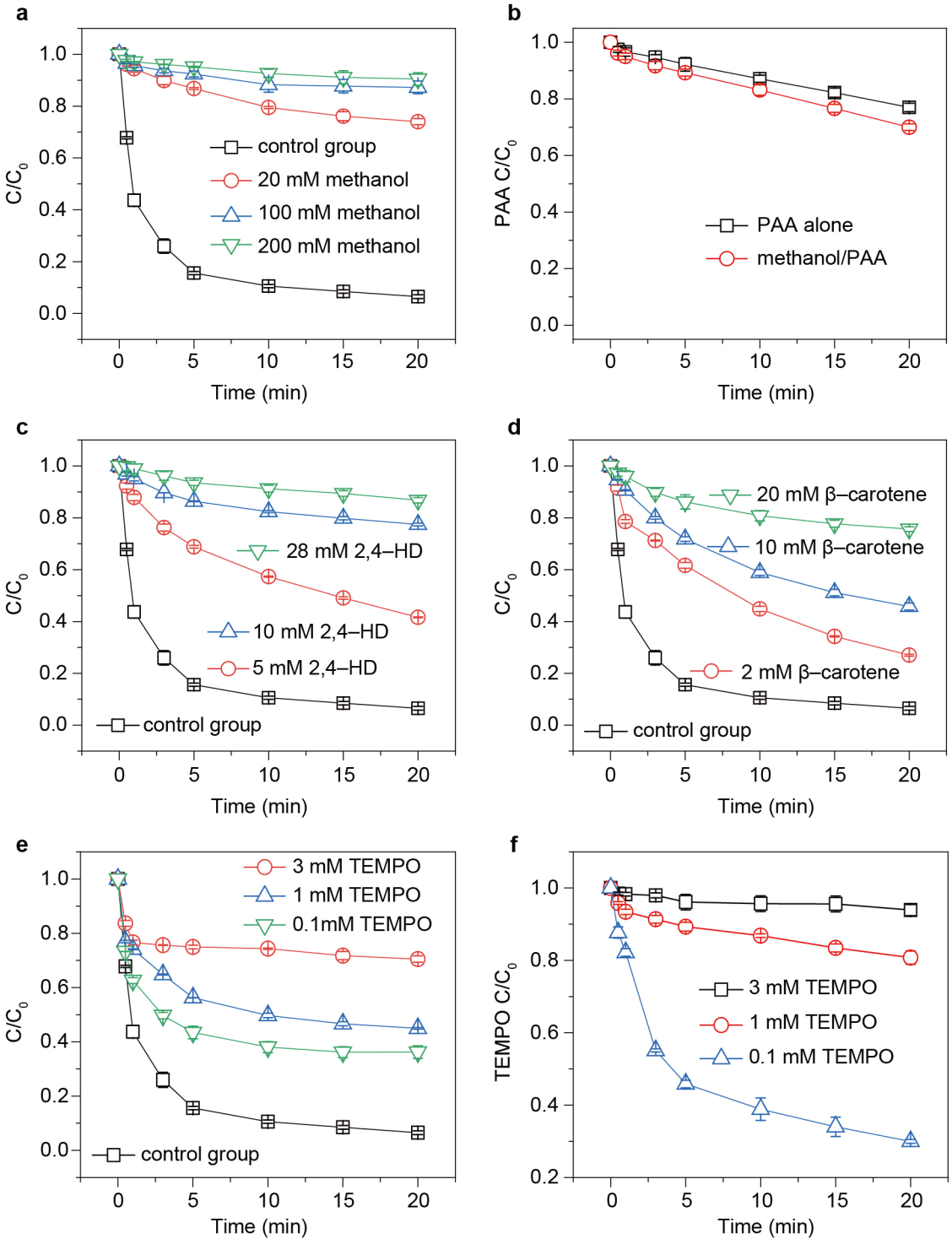

Figure S52. Verification of R–O• reactive species in CNT/Co_{n+1}/PAA system. Time courses of SMX degradation in CNT/Co_{n-1}/PAA system with varying concentration of a) methanol, c) 2,4–hexadiene (2,4–HD), d) β–carotene and e) TEMPO. Reaction conditions: 100 mg L^{-1} catalysts, 120 μM PAA, 2.5 mg L^{-1} SMX, 240 mT MF, 7.0±0.2 pH and room temperature. b) Time profile of PAA utilization in reaction solution contained 120 μM PAA only and reaction solution with mixture of 200 mM methanol/PAA. Methanol does not affect PAA concentration nearly disclosing that methanol cannot react with PAA to consume PAA. f) Time profile of TEMPO degradation in CNT/Co_{n-1}/PAA system. TEMPO can be effectively degraded indicating the generation of R–O• reactive species CNT/Co_{n+1}/PAA system.

Methanol has high reactivity toward both of •OH and R–O• [15], and as shown in figure S52a and b, its addition exhibited the pronounced inhibition for SMX removal indicating the primary reactive species of •OH and R–O• in our system. 2,4–HD possess high reactivity for R–O• (1.0×10^{10} $M^{-1}s^{-1}$) [11], its addition nearly full prevent the removal of SMX shown in figure S52c, again indicating the primary reactive species of R–O• existed. Similarly, β–carotene added into the system effectively inhibited the SMX abatement also illustrating the primary reactive species of R–O• because of the high reaction rate between β–carotene and R–O• (9.2×10^{8} $M^{-1}s^{-1}$) [11].

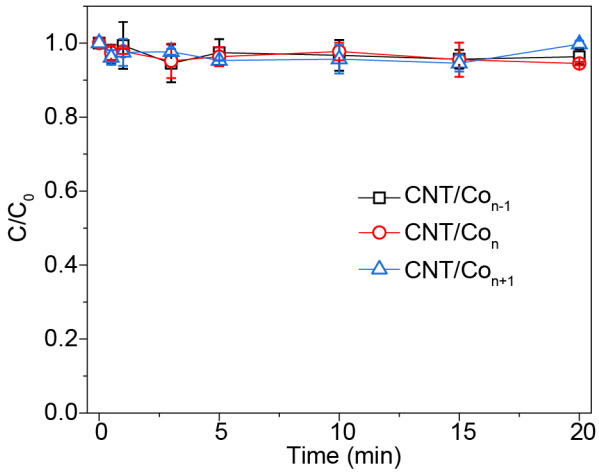

Figure S53. Time profile of SMX adsorption in CNT/Co_n series. Reaction conditions: 10 mg L^{-1} catalyst and 2.5 mg L^{-1} SMX. Inappreciable adsorption contribution for SMX removal indicated that removal of SMX in CNT/Co_n series activating PAA systems is totally attributed to catalytic oxidation degradation, and this process correspondingly occurs in bulk solution not the interfaces of catalysts.

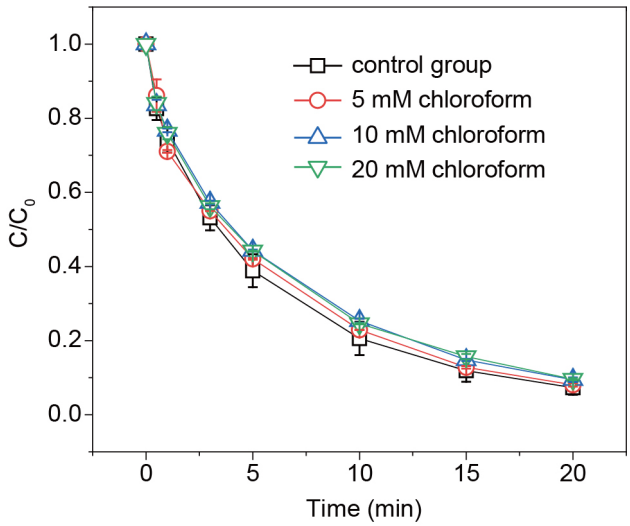

Figure S54. Time courses of SMX degradation in CNT/Co_n/PAA system under varying concentration of

chloroform. Reaction conditions: 10 mg L^{-1} catalysts, 200 μM PAA, 2.5 mg L^{-1} SMX, 7.0±0.2 pH and room temperature.

Chloroform as a classic trapper for superoxide radical with a rate constant 3×10^{10} $M^{-1}s^{-1}$ [16], there are a negligible disturbance for SMX removal after adding chloroform, hinting the absence of superoxide radical in our system.

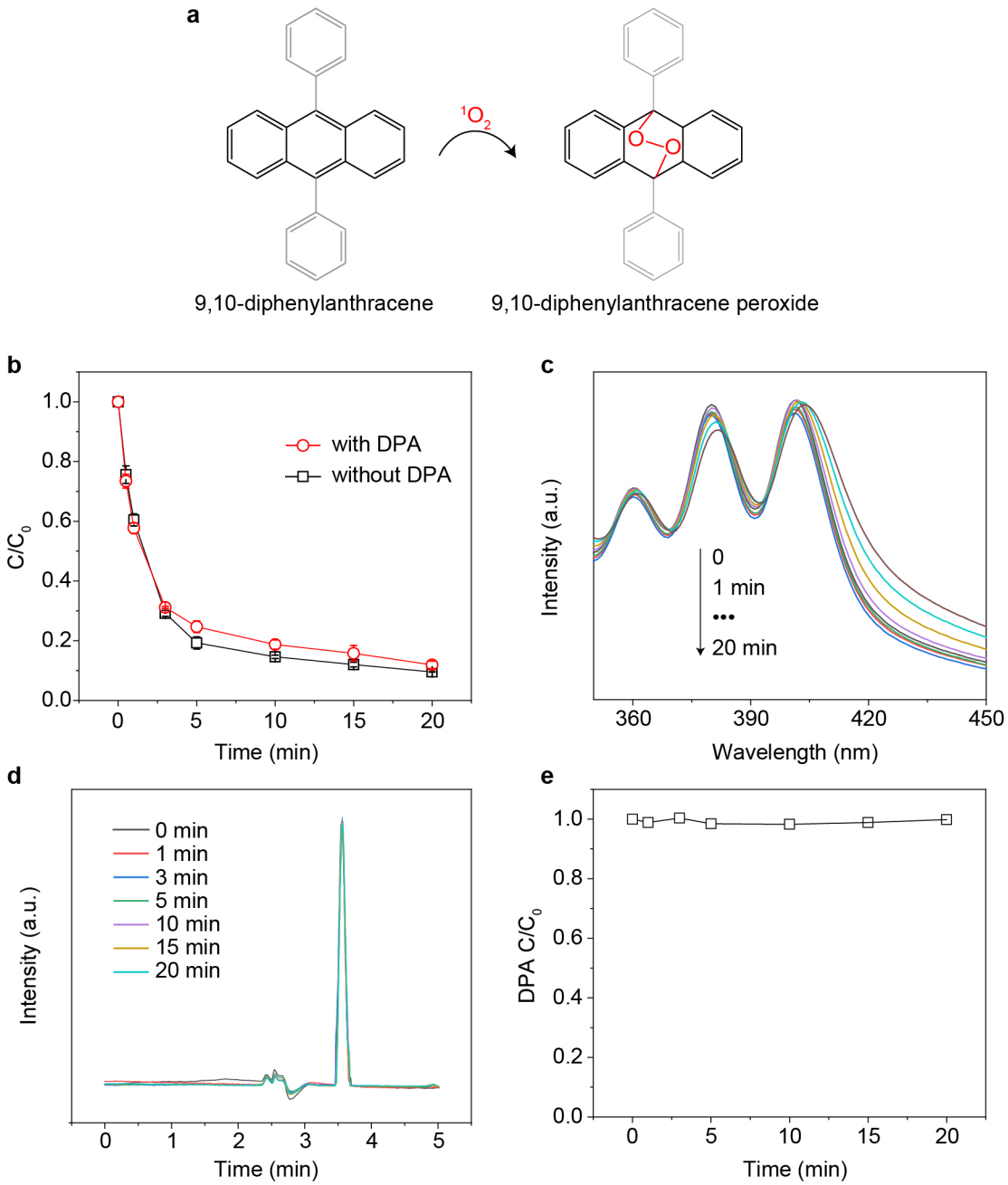

Figure S55. Verification of singlet oxygen in CNT/Co_n/PAA system. a) Schematical illustration of 9,10–diphenylanthracene (DPA) reacted with singlet oxygen. b) Time profiles of SMX removal in CNT/Co_n/PAA system with and without DPA as reaction solution. Considering DPA insoluble in water,

here 10 mg L^{-1} DPA was dissolved in 10% acetonitrile solution as the reaction medium. Time profiles of DPA concentration in CNT/Co_n/PAA system detected by c) UV–Vis absorption spectroscopy and d) HPLC technology. e) Time profiles of DPA removal in CNT/Co_n/PAA system. Unseen variation of DPA concentrations in CNT/Co_n/PAA system and unaffected SMX removal when coexisted with DPA both hint the absence of singlet oxygen in our system.

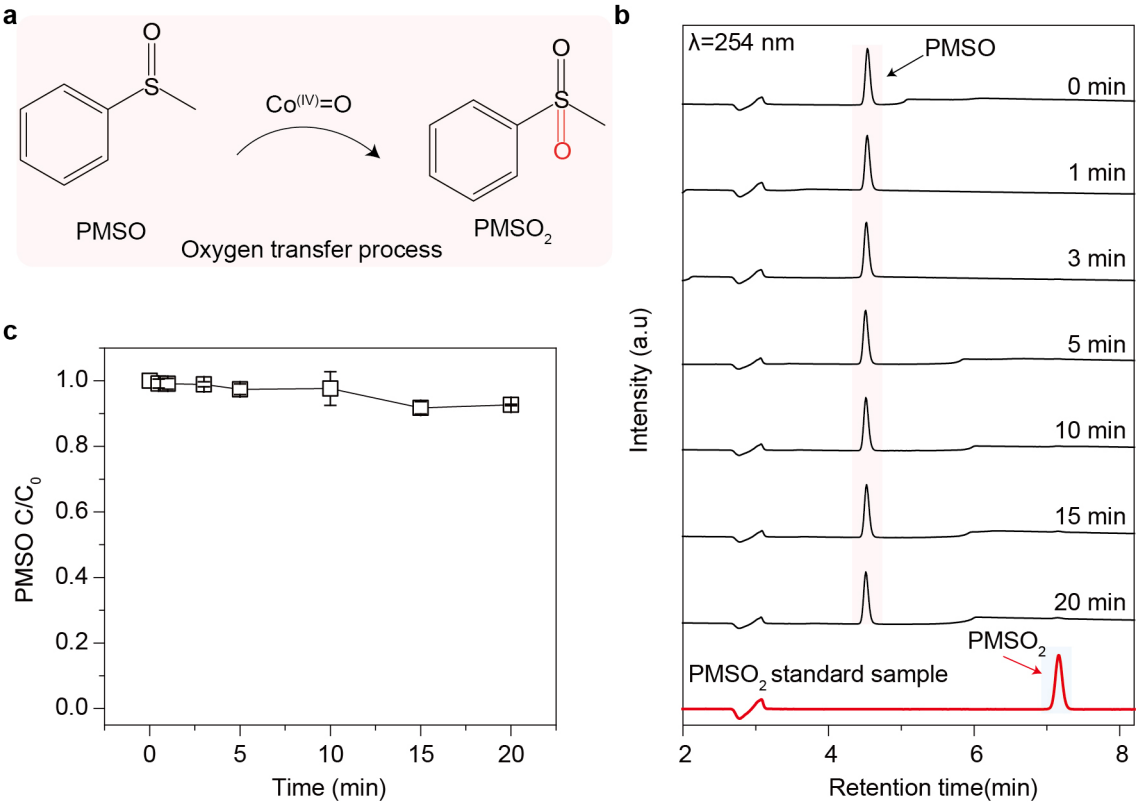

Figure S56. Verification of high–valence cobalt species in CNT/Co_n/PAA system. a) Illustration of reaction process of PMSO oxidized into $PMSO_2$ via oxygen transfer process of high–valence cobalt species. b) Two-dimensional HPLC spectra for detection of PMSO in CNT/Co_n/PAA system at different reaction time. The peak at retention time of rough 4.5 min is assigned to PMSO, and after combination the spectrum of $PMSO_2$ standard sample, we can find the peak of $PMSO_2$ at retention time of rough 7.2 min. This experimental result verifies absence of high–valence cobalt species in CNT/Co_n/PAA system because of no generation of $PMSO_2$.

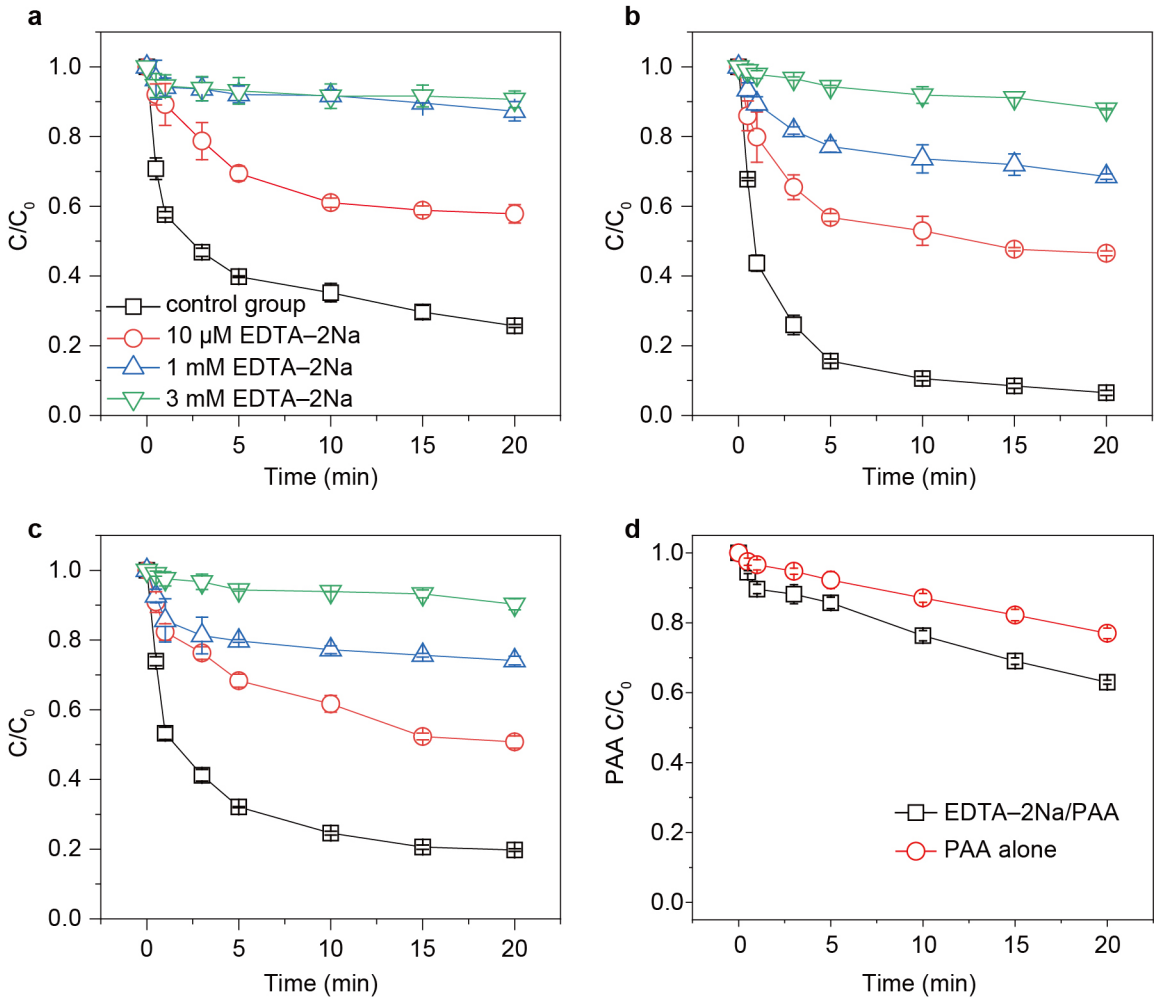

Figure S57. Confirmation of cobalt sites in the catalysts as the reactive site for PAA activation. Time courses of SMX degradation in a) CNT/Co_{n-1}/PAA system, b) CNT/Co_n/PAA system and c) CNT/Co_{n+1}/PAA system with addition of 10 μM, 1 mM or 3 mM EDTA–2Na. Reaction conditions: 100 mg L^{-1} catalysts, 120 μM PAA, 2.5 mg L^{-1} SMX, 240 mT MF, 7.0±0.2 pH and room temperature.

EDTA–2Na as a classic chelant to the metal sites, putting it into reaction solution significantly suppressed the removal of SMX in present systems, again hinting the important role of cobalt site in our catalysts. d) Time profile of PAA utilization in reaction solution contained 120 μM PAA only or reaction solution with mixture of 3 mM EDTA–2Na/PAA. EDTA–2Na does not nearly affect PAA concentration disclosing that it cannot react with PAA to consume PAA.

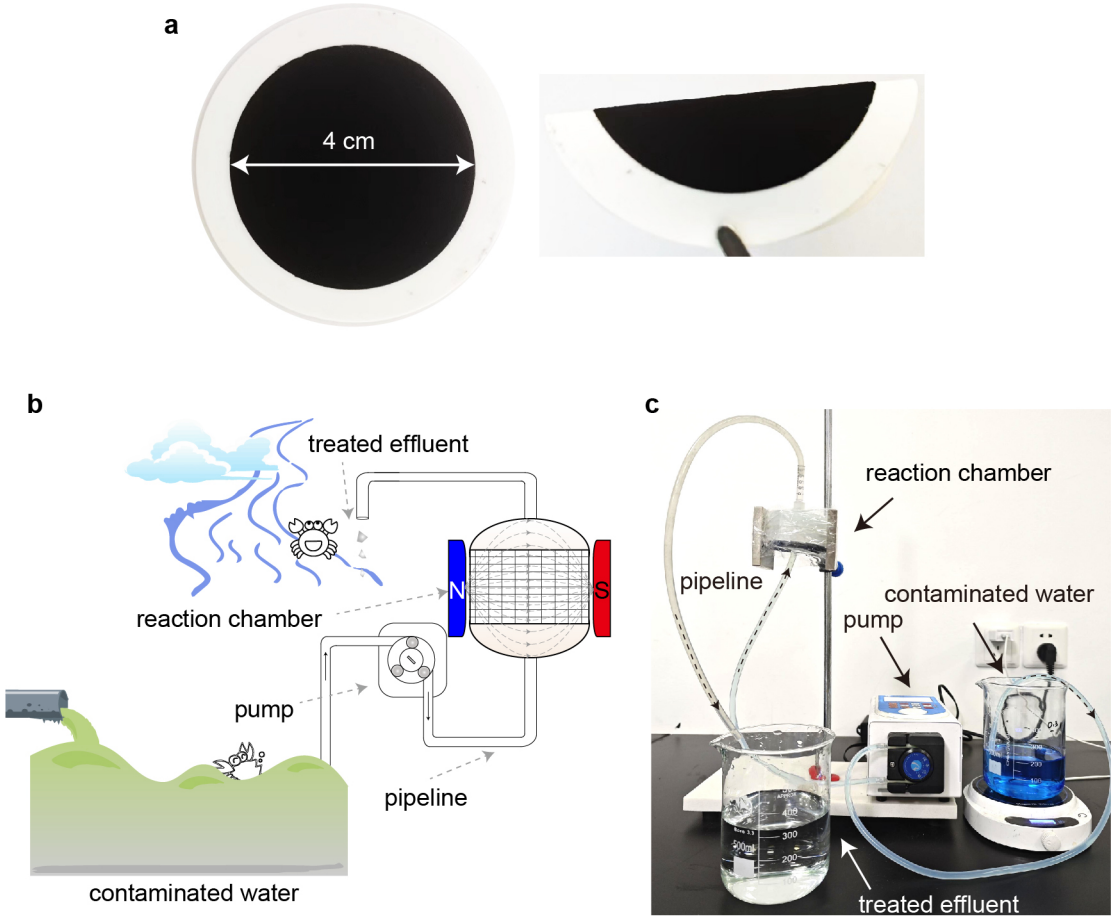

Figure S58. a) Digital photos of CNT/Co_n membrane. b) Schematic illustration of the practical application scenario of our continuous–flow system. c) Digital photo of our continuous–flow system. Taken methylene blue's treatment as example, the inflow is blue, and the treated effluent is colorless.

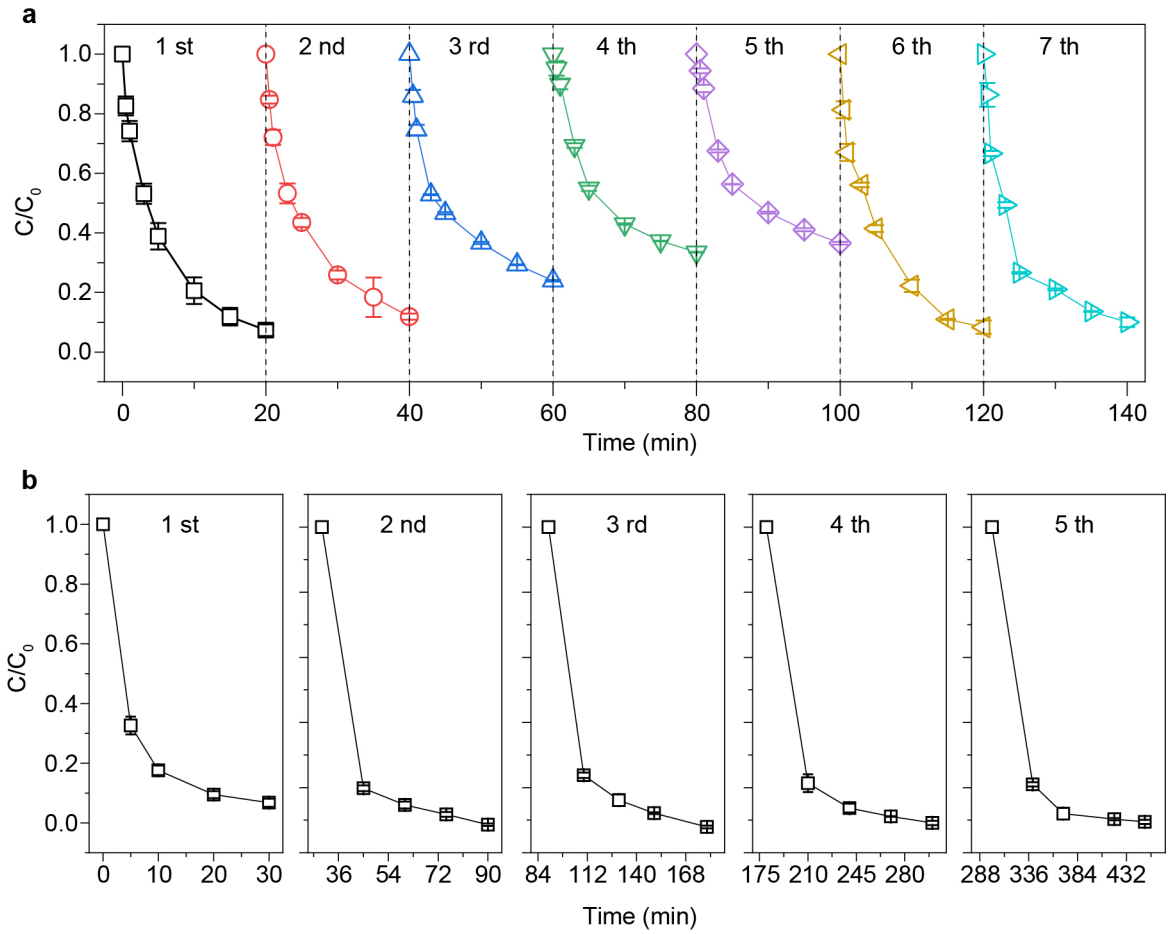

Figure S59. a) Time profile of SMX degradation in CNT/Co_n/PAA system via consecutive operations. Reaction conditions: 10 mg L^{-1} CNT/Co_n, 200 μM PAA and 2.5 mg L^{-1} SMX, 7.0±0.2 pH and room temperature. b) Time profile of SMX degradation in CNT/Co_n/PAA system via consecutive operations with the assistance of MF.

In the above Fig. S59a, we recovered the spent catalyst after 5th operation, via 500 ^{o}C pyrolysis treatment for 30 min to clear the intermediates onto the surface of catalysts, and again observed the refreshed performance of SMX removal at 6th and 7th operations. This phenomenon indicated that gradual deactivation of the catalyst from 1st to 5th operations may be attributed to the covered active sites by the intermediates of degraded SMX. When the system was conducted under a MF, there was scarcely observed by gradual deactivation of the catalyst from 1st to 5th operations. These observations not only highlight the robust structure of CNT/Co_n when activated PAA, but also point out the key role of MF toward optimizing binding energy of intermediates to tune adsorption of intermediates.

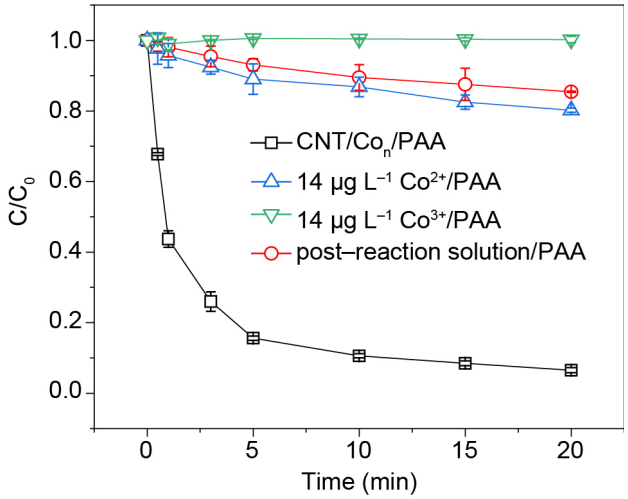

Figure S60. Time profile of SMX degradation in different reaction systems. Reaction conditions: 100 mg L^{-1} CNT/Co_n (if needed), 14 μg L^{-1} cobalt ion (if needed), 120 μM PAA, 2.5 mg L^{-1} SMX, 240 mT MF, 7.0±0.2 pH and room temperature.

Leaching of cobalt ion was measured to be 14 μg L^{-1} in CNT/Co_n/PAA/SMX system via inductively coupled plasma–mass spectrometry technology. Such leaching concentration of cobalt ion is far lower than the guideline value of 100 μg L^{-1} for drinking water quality from the World Health Organization. To evaluate possible contribution of SMX removal via PAA activation from the leaching cobalt ion, we recollected the post–reaction solution via filtration the powder catalysts to prevent the possible PAA activation. The result showed that the leaching cobalt has a negligible contribution toward SMX removal.

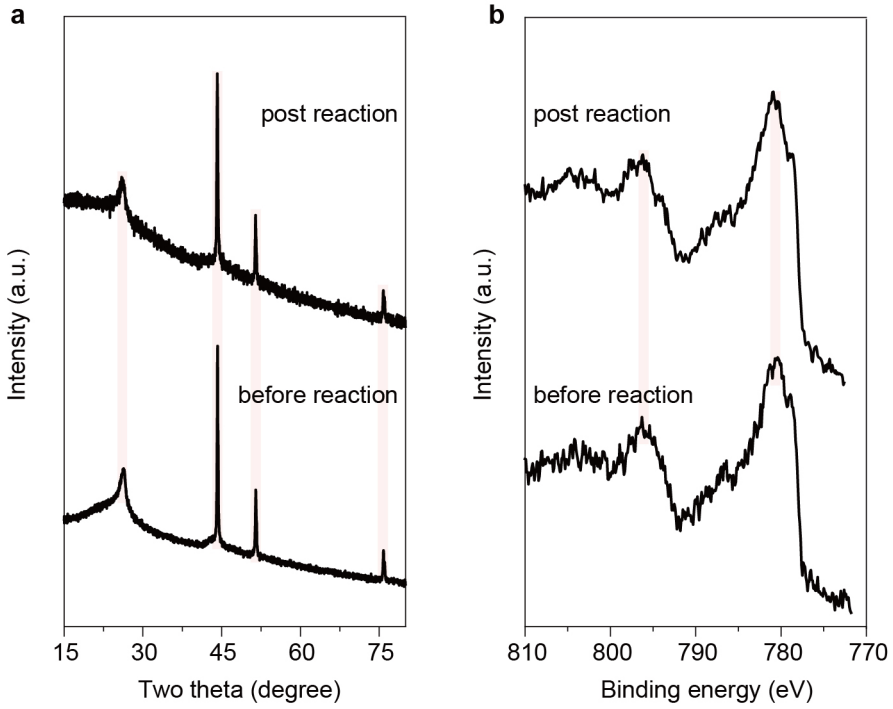

Figure S61. a) XRD patterns and b) high–resolution Co 2p XPS spectrums for fresh and spent CNT/Co_n.

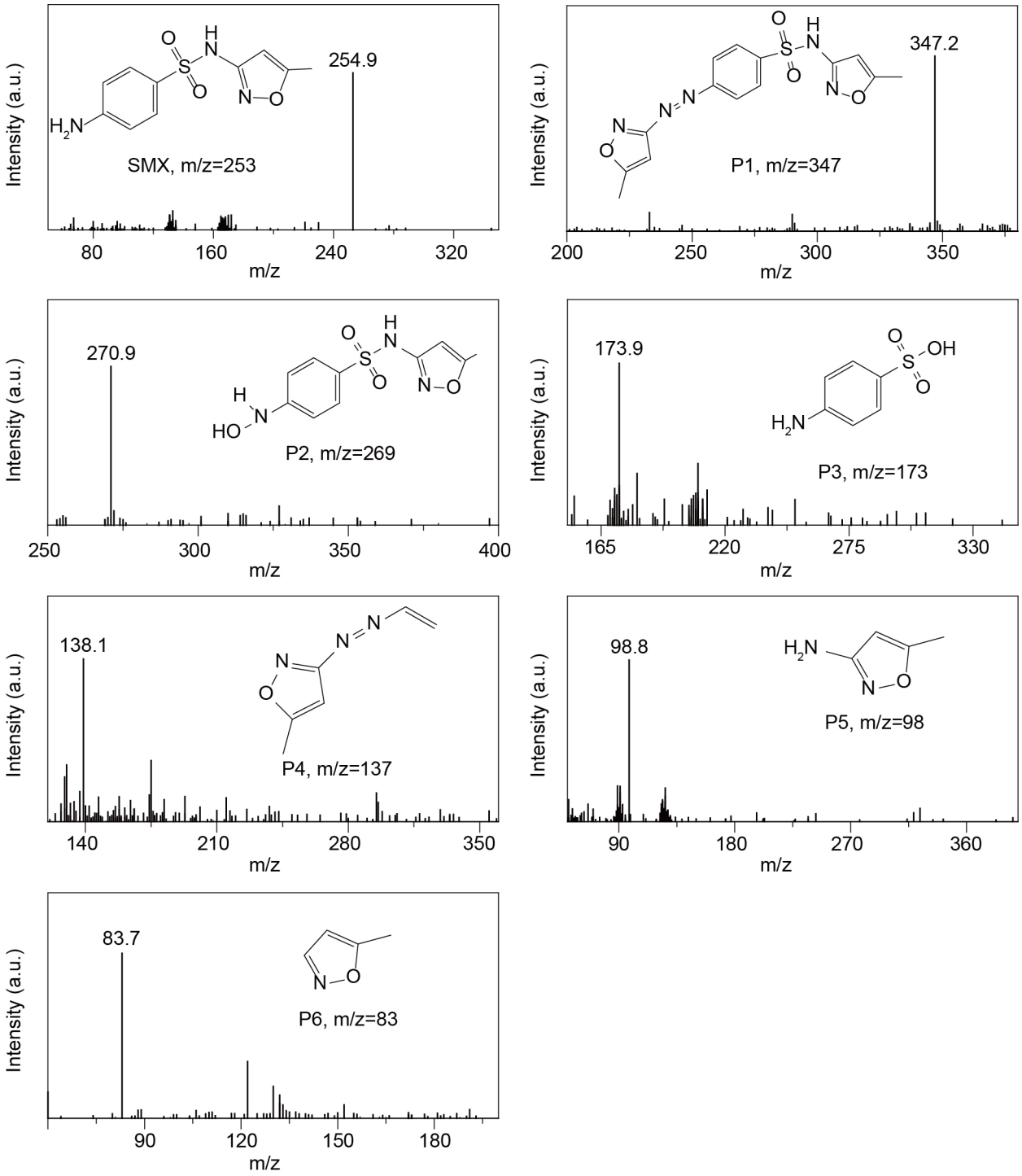

Figure S62. Mass spectroscopy (m/z) analysis of the main intermediate products from the degradation of SMX in CNT/Co_n/PAA system.

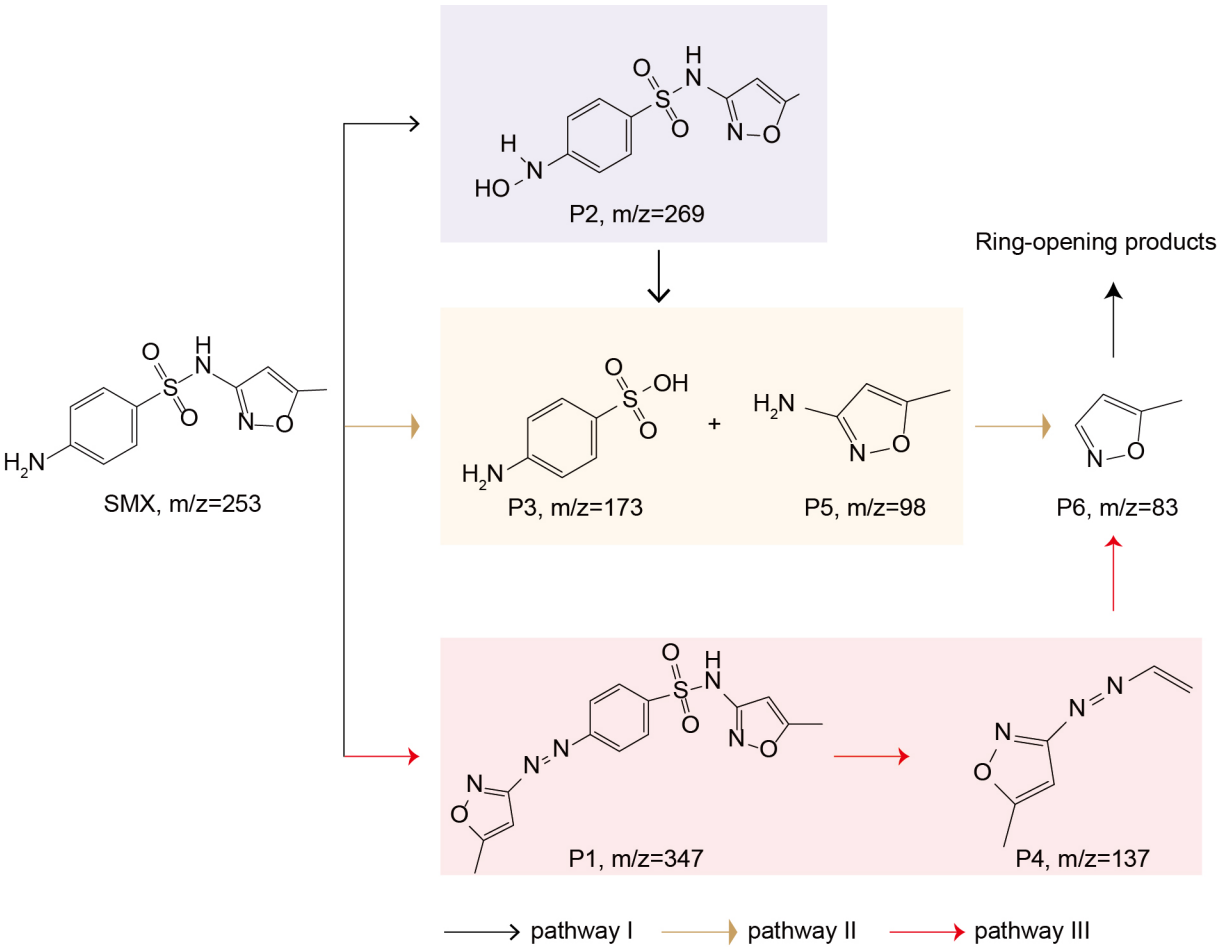

Figure S63. Possible three degradation pathways of SMX in MF–assisted CNT/Co_n/PAA system.

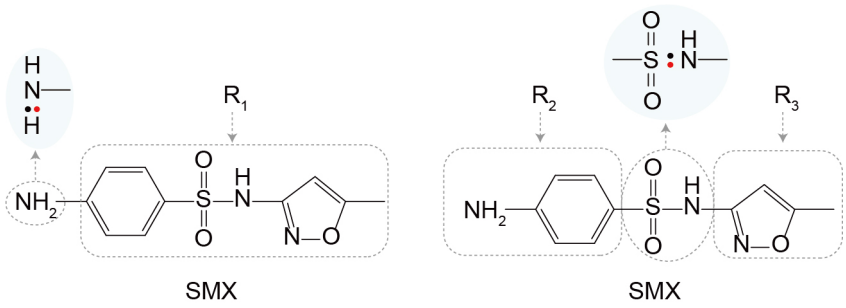

Figure S64. For a clearer description of the degradation process of SMX, SMX is designated by three parts of R_1, R_2 and R_3.

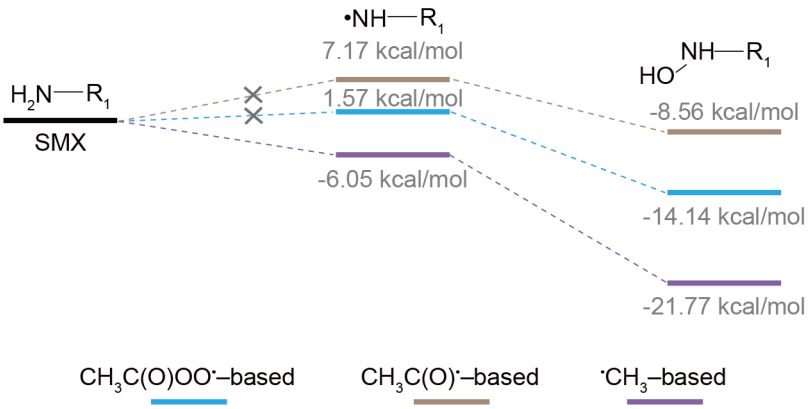

Figure S65. The Gibbs free energy of SMX degraded to P2 intermediate in CNT/Co_n/PAA system based on the attacking of $^{\bullet}CH_3$, $CH_3C(O)^{\bullet}$ or $CH_3C(O)OO^{\bullet}$ (pathway I).

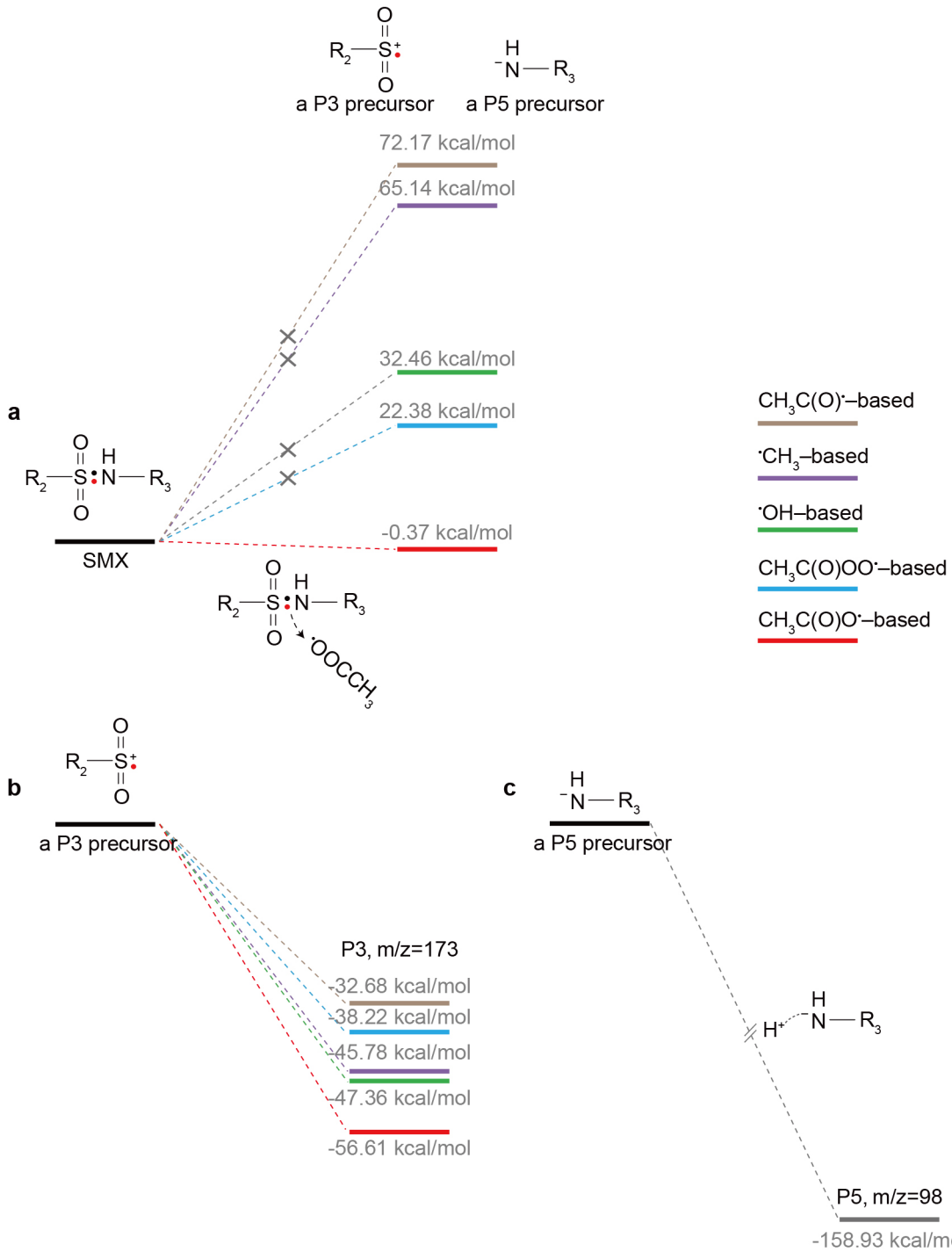

Figure S66. a) The Gibbs free energy of 26S–11N bond in SMX breaking into the precursors of P3 and P5 in free radicals of $^{\bullet}CH_3$, $CH_3C(O)^{\bullet}$, $CH_3C(O)O^{\bullet}$, $CH_3C(O)OO^{\bullet}$ or $^{\bullet}OH$. b) The Gibbs free energy of the P3 precursor converted to P3 in free radicals of $^{\bullet}CH_3$, $CH_3C(O)^{\bullet}$, $CH_3C(O)O^{\bullet}$, $CH_3C(O)OO^{\bullet}$ or $^{\bullet}OH$. c) The Gibbs free energy of the P5 precursor converted to P5 in H^+.

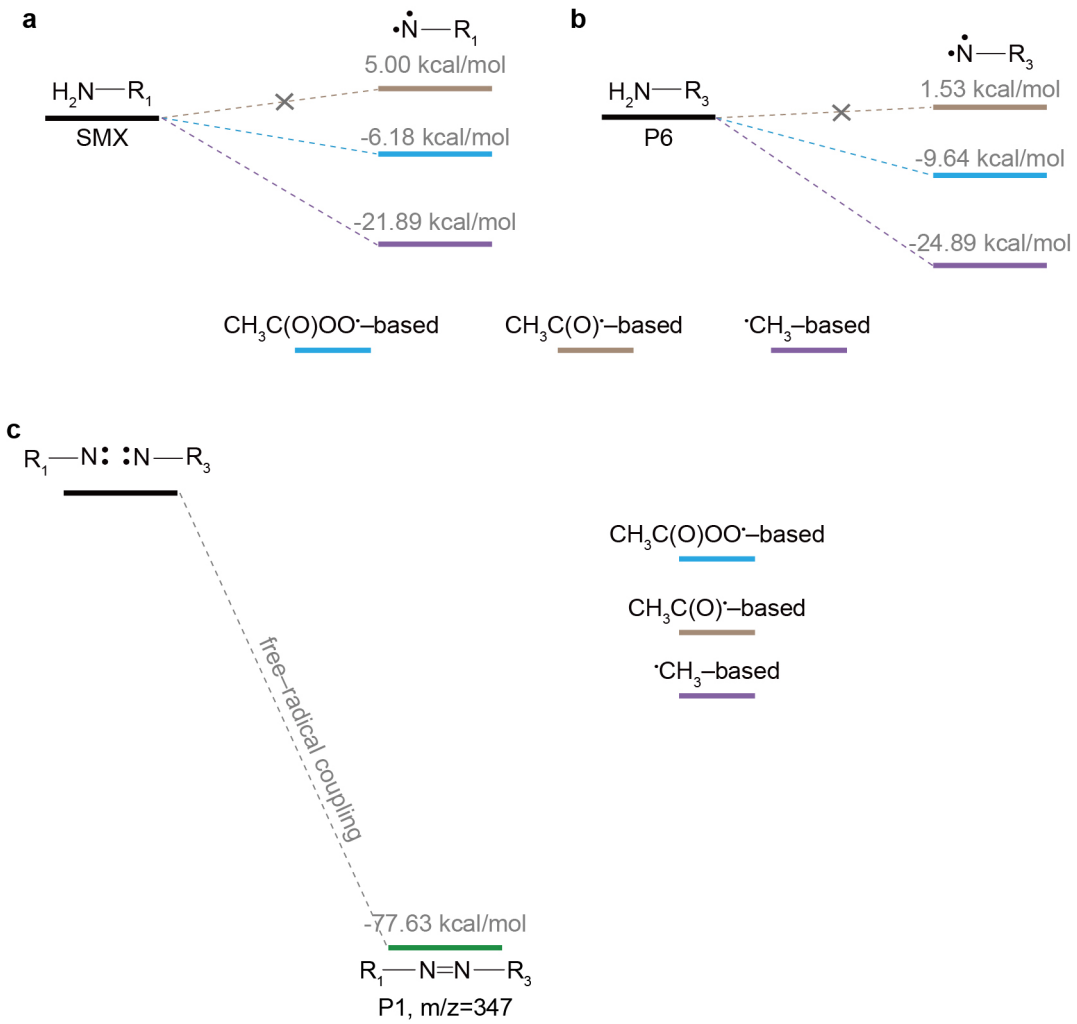

Figure S67. The Gibbs free energy of a) R_1–N: converted from SMX and b) :N–R_3 converted from P6 in CNT/Co_n/PAA system based on the attacking of $^{\bullet}CH_3$, $CH_3C(O)^{\bullet}$ or $CH_3C(O)OO^{\bullet}$. c) Gibbs free energy of free–radical coupling between R_1–N: and :N–R_3 to generate intermediate product of P1.

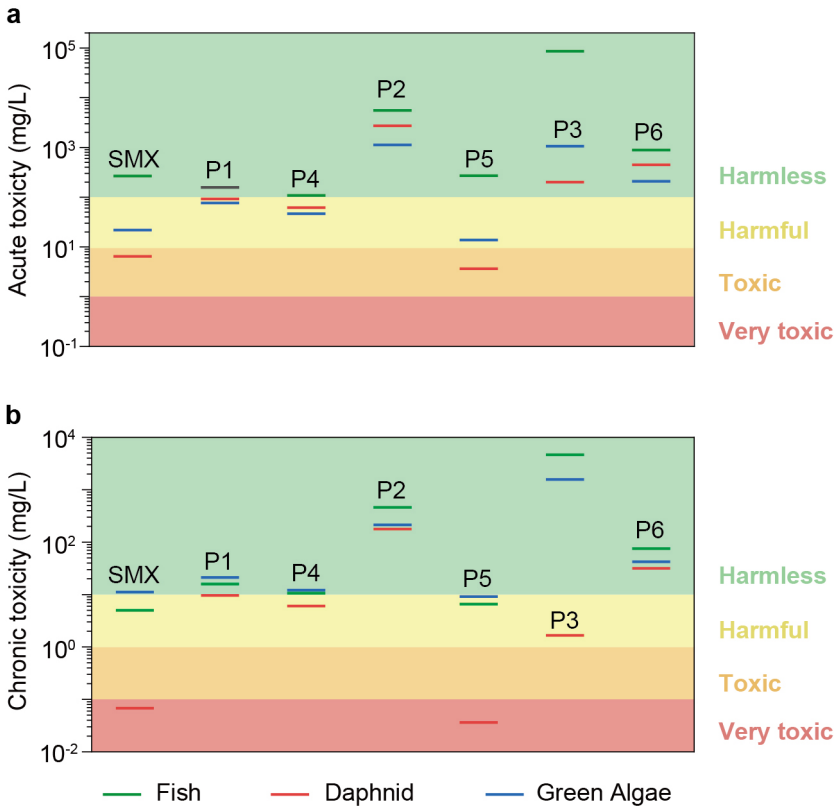

Figure S68. a) Acute toxicity assessment and b) chronic toxicity assessment of possible intermediate products from SMX degradation in our system. The toxicity assessment of these products was conducted by the well–known Ecological Structural Activity Relationships (ECOSAR) program [6].

References

[1] J. W. Wang, B. Xiong, L. Miao, S. L. Wang, P. C. Xie, Z. P. Wang, J. Ma, Applying a novel advanced oxidation process of activated peracetic acid by $CoFe_2O_4$ to efficiently degrade sulfamethoxazole, Appl. Catal. B Environ. 2021, **280**, 119422.

[2] S. Chen, M. Q. Cai, Y. Z. Liu, L. Q. Zhang, L. Feng, Effects of water matrices on the degradation of naproxen by reactive radicals in the UV/peracetic acid process, Water Res. 2019, **150**, 153-161.

[3] Z. P. Wang, J. W. Wang, B. Xiong, F. Bai, S. L. Wang, Y. Wan, L. Zhang, P. C. Xie, M. R. Wiesner, Application of Cobalt/peracetic acid to degrade sulfamethoxazole at neutral condition: efficiency and mechanisms, Environ. Sci. Technol. 2020, **54**, 464-475.

[4] S. R. Yang, C. S. He, Z. H. Xie, L. L. Li, Z. K. Xiong, H. Zhang, P. Zhou, F. Jiang, Y. Mu, B. Lai, Efficient activation of PAA by FeS for fast removal of pharmaceuticals: The dual role of sulfur species in regulating the reactive oxidized species, Water Res. 2022, **217**, 118402.

[5] K. Zhang, A. Cao, L. H. Wandall, J. Vernieres, J. Kibsgaard, J. K. Norskov, I. Chorkendorff, Spin-mediated promotion of Co catalysts for ammonia synthesis, Science, 2024, **383**, 1357-1363.

[6] Y. Q. Zhang, M. H. Chen, X. Y. He, E. Z. Zhao, H. Liang, J. G. Shang, K. Liu, J. Q. Chen, S. J. Zuo, M. H. Zhou, Intrinsic strain of defect sites steering chlorination reaction for water purification, Nat. Commun. 2025, **16**, 2652.

[7] X. T. Wang, T. Ouyang, L. Wang, J. H. Zhong, T. Y. Ma, Z. Q. Liu, Redox-inert Fe^{3+} ions in octahedral sites of Co-Fe spinel oxides with enhanced oxygen catalytic activity for rechargeable Zinc-air batteries, Angew. Chem. Int. Ed. 2019, **58**, 13291-13296.

[8] L. Yang, H. Cheng, H. Li, G. Sun, S. Liu, T. Ma, L. Zhang, Atomic confinement empowered CoZn dual-single-atom nanotubes for H_2O_2 production in sequential dual-cathode electro-Fenton process, Adv. Mater. 2024, **36** ,2406957.
[9] C. H. Chen, Q. H. Zhou, Z. Y. Guo, H. Li, C. Miao, D. Chen, X. H. Hu, X. Feng, V. Noël, S. Ghoshal, G. V. Lowry, L. Z. Zhu, D. H. Lin, J. Xu, Lattice-sulfur-impregnated zero-valent iron crystals for long-term metal encapsulation, Nat. Sustain. 2024, **7**, 1264-1272.
[10] S. R. Yang, S. Sun, Z. H. Xie, Y. D. Dong, P. Zhou, J. Zhang, Z. K. Xiong, C. S. He, Y. Mu, B. Lai, Comprehensive insight into the common organic radicals in advanced oxidation processes for water decontamination, Environ. Sci. Technol. 2024, **58**, 19571-19583.
[11] Y. P. Tong, X. L. Wang, Y. Z. Zhang, J. Xu, C. Sun, Reactive species in peracetic acid-based AOPs: A critical review of their formation mechanisms, identification methods and oxidation performances, Water Res. 2025, **272**, 122917
[12] H. C. Zheng, L. Zhang, G. Y. Zhang, Y. H. Gan, M. Xie, S. J. Zhang, UV-induced redox conversion of tellurite by biacetyl, Environ. Sci. Technol. 2021, **55**, 16646-16654.
[13] S. S. Wei, W. T. Zhang, Z. Y. Wang, G. Y. Zhang, W. W. Li, G. X. Zeng, S. J. Zhang, Operando surface ligands boost Pt nanozyme activity for H_2O_2 catalysis via bridged electron transfer, ACS Catal. 2025, **15**, 6439-6449.
[14] D. Y. Xing, S. J. Shao, Y. Y. Yang, Z. M. Zhou, G. H. Jing, X. D. Zhao, Mechanistic insights into the efficient activation of peracetic acid by pyrite for the tetracycline abatement, Water Res. 2022, **222**, 118930.
[15] F. Miao, C. Cheng, W. Ren, H. Zhang, S. B. Wang, X. G. Duan, Dual nonradical catalytic pathways mediated by nanodiamond-derived sp/sp hybrids for sustainable peracetic acid activation and water decontamination, Environ. Sci. Technol., 2024, **58**, 8554-8564.
[16] S. J. Zuo, R. X. Guo, W. D. Xue, J. G. Shang, J. Q. Chen, Y. Q. Zhang, Decipher the key role of ketone toward singlet oxygen evolution in Fenton-like process for water decontamination, Appl. Catal. B Environ. 2023, **339**, 123100.